November 2015

Impacts of Three-Dimensional Non-Uniform Groundwater Flows for Quantifying Groundwater-Surface Water Interactions Using Heat as a Tracer

Jonathan M. Reeves
University of Massachusetts Amherst

Recommended Citation

Reeves, Jonathan M., "Impacts of Three-Dimensional Non-Uniform Groundwater Flows for Quantifying Groundwater-Surface Water Interactions Using Heat as a Tracer" (2015). *Masters Theses*. 294.
https://scholarworks.umass.edu/masters_theses_2/294

IMPACTS OF THREE-DIMENSIONAL NON-UNIFORM GROUNDWATER FLOWS FOR QUANTIFYING GROUNDWATER-SURFACE WATER INTERACTIONS USING HEAT AS A TRACER

A Thesis Presented

by

JONATHAN M. REEVES

Submitted to the Graduate School of the
University of Massachusetts Amherst in partial fulfillment
of the requirements for the degree of

MASTER OF SCIENCE

September 2015

Department of Geosciences

IMPACTS OF THREE-DIMENSIONAL NON-UNIFORM GROUNDWATER FLOWS FOR QUANTIFYING GROUNDWATER-SURFACE WATER INTERACTIONS USING HEAT AS A TRACER

A Thesis Presented

by

JONATHAN M. REEVES

Approved as to style and content by:

Christine E. Hatch, Chair

David Boutt, Member

William Clement, Member

Julie Brigham-Grette, Department Head
Department of Geosciences

ACKNOWLEDGEMENTS

Foremost, I wish to express my great gratitude to my advisor, Dr. Christine Hatch for her patience, constant positive attitude and invaluable feedback. I would also like to thank the rest of my thesis committee: Dr. Bill Clement and Dr. David Boutt for their insightful comments and hard questions. Additionally, I would like to acknowledge the sources of funding which supported me through my degree: University of Massachusetts Faculty Research Grant, University of Massachusetts Department of Geosciences Andrew Wise Memorial Scholarship and the Geological Society of America Graduate Research Grants Lastly, I’d like to thank my family for their encouragement and support.

ABSTRACT

IMPACTS OF THREE-DIMENSIONAL NON-UNIFORM GROUNDWATER FLOWS FOR QUANTIFYING GROUNDWATER-SURFACE WATER INTERACTIONS USING HEAT AS A TRACER

SEPTEMBER 2015

JONATHAN M. REEVES, B.A., SKIDMORE COLLEGE

M.S., UNIVERSITY OF MASSACHUSETTS AMHERST

Directed by: Professor Christine E. Hatch

Heat-as-a-tracer has become a common method to quantify surface water-groundwater interactions (SW/GW). However, the method relies on a number of assumptions that are likely violated in natural systems. Numerical studies have explored the effects of violating these fundamental assumptions to various degrees, such as heterogeneous streambed properties, two-dimensional groundwater flow fields and uncertainty in thermal parameters for the 1-dimensional heat-as-a-tracer method. No work to date has addressed the impacts of non-uniform, three-dimensional groundwater flows on the use of heat-as-a-tracer to quantify SW/GW interactions. Synthetic temperature time series were generated using COMSOL Multiphysics for a three-dimensional cube designed to represent a laboratory setup of homogeneous, isotropic sand with a sinusoidal temperature variation applied to the top. We compare temperature-derived fluxes to model-generated fluxes to assess the performance of methods using temperature to quantify 1D vertical fluxes in response to multi-dimensional groundwater flows. Both increasingly non-uniform and non-vertical groundwater flow fields result in increasing errors for both amplitude-ratio-derived groundwater flux and temperature-derived effective thermal diffusivity. For losing flow geometries, errors in temperature-derived effective thermal diffusivity are highly correlated with errors in temperature-derived flux and can be used to identify if underlying assumptions necessary for heat-as-a-tracer for quantifying groundwater flows have been violated. For this model set-up, when groundwater flows are non-uniform, the thermal method generally calculates fluxes outside the range occurring between temperature sensor pairs. When errors are low (15% of flux calculations), temperature derived fluxes more closely match the minimum magnitude flow occurring between the sensors.

TABLE OF CONTENTS

Page

CHAPTER

APPENDICES

LIST OF TABLES

Table Page

LIST OF FIGURES

LIST OF SYMBOLS

T	Temperature
t	time
z	depth
q	Darcy flux
κ_e	effective thermal diffusivity$= \frac{\lambda_0}{(\rho c)_b}$
ρ_w	density of water
c_w	specific heat capacity water
ρ_s	density porous solid
c_s	specific heat capacity porous solid
$(\rho c)_b$	bulk volumetric heat capacity$= n\rho_w c_w + (1-n)\rho_s c_s$
n	porosity
λ_0	bulk effective thermal conductivity
λ_w	effective thermal conductivity water
λ_s	effective thermal conductivity porous solid
A	Amplitude
P	Period
α	$= \sqrt{{v_t}^4 + \left(\frac{8\pi\kappa_e}{P}\right)^2}$
v_t	advective thermal front velocity
c_b	bulk specific heat capacity
A_r	Amplitude Ratio
$\Delta\Phi$	Phase Shift
Δz	distance between temperature observation nodes
ω	angular frequency = $2\pi/P$
η	dimensionless parameter$= \frac{-\ln(A_r)}{\Delta\Phi}$
h	hydraulic head

K	hydraulic conductivity
x, y, z	orthogonal axes of the model domain
T_0	initial temperature of the model/ bottom boundary temperature
$\hat{n}$	normal vector to a model boundary
q_M	actual modeled Darcy flux
q_T	temperature-derived Darcy flux
$\frac{dq}{dz}$	degree of non-uniformity= $\frac{\lvert q_d \rvert - \lvert q_s \rvert}{z_d - z_s}$
q_h	horizontal Darcy flux magnitude
q_x, q_y	horizontal component of Darcy flux
κ_{eM}	true (model-input) effective thermal diffusivity
κ_{eT}	thermal derived effective thermal diffusivity

INTRODUCTION

Surface water-groundwater (SW/GW) interactions play an important role in contaminant transport (e.g. Elliot and Brooks 1997, Marzadri et al. 2011, Schmidt et a. 2011), biogeochemical processes (e.g. Boano et al. 2010, Findlay 1996) and ecological habitat (Baxter and Hauer 2000, Brunke and Gonser 1997, Stanford and Ward 1988, 1993). With the trend toward more extreme variations in precipitation distribution, hydrogeologists must improve their tools for quantifying gaining and losing stream reaches (Scibek et al. 2007, Zhou et al. 2014). Understanding these interactions will help land use managers maintain sustainable use of water resources during extended dry spells as well as address the impacts on water quality during large precipitation events (Constantz 2008, Pulido Velasquez et al. 2006).

Flux across streambeds is difficult to quantify due to several factors, including: 1) it is a point scale measurement that varies spatially (i.e. Keery et al. 2007); 2) it can vary temporally (i.e. Constantz et al. 1994; Winter et al. 1998); and 3) the substrate must not be disturbed for an accurate measurement (Rosenbury and Morin 2004). Heat-as-a-tracer has become a popular method for quantifying SW/GW interactions and can be used to verify the point scale measurements of conventional hydraulic measurements such as seepage meters, piezometers and the reach scale measurements of differential gauging and tracer tests (e.g. Hatch et al. 2006, Lautz 2012, Briggs et al. 2014).

Temperature has proven to be an inexpensive, easily and accurately measured, robust tracer, allowing calculations of seepage without requiring inclusion of difficult-to-quantify hydraulic conductivity (Johnson et al. 2005, Hatch et al. 2006). Additionally, technological advances have enable the development of easy to use, inexpensive automated temperature loggers with improved accuracy for continuous, remote data collection (Anderson 2005).

The thermal method for calculating one-dimensional flux is limited by both spatial and temporal resolution and requires assumptions to perform this analysis on natural systems. Applications of heat-as-a-tracer to estimate velocity (Hatch et al. 2006, Keery et al. 2007, McCallum et al. 2012, Luce et al. 2013) require that: (1) fluid flow is one-dimensional and vertical, (2) hydraulic and thermal properties are homogeneous for both the fluid and porous medium, (3) there exists no thermal gradient with depth, (4) the diurnal temperature signal at the upper boundary is sinusoidal, and (5) there is a thermal equilibrium between the fluid and the porous media for any point in space and time (Stallman 1965). Each of these assumptions can be violated to some degree in natural systems. However, the use of thermal methods for calculating flux is another tool for researchers to use to quantify SW/GW interactions.

Current thermal methods assume flow in the vertical direction only, which is not necessarily the case in nature (Bhaskar et al. 2012). Swanson and Cardenas (2010) and Rau et al. (2010) showed that streams gaining from aquifers are likely to contain a significant non-vertical component. Hyporheic flows, or short length flow paths into and out of the streambed, may be parallel or oblique to surface water flow (Bhaskar et al. 2012) and can frequently converge or diverge at the sediment-water interface (Cuthbert and Mackay 2013).

Both model and field studies have effectively produced results for calculating groundwater flux in the vertical direction (e.g. Goto 2005, Hatch et al. 2006, Lautz 2012). Experimental and modeling studies have shown that non-vertical flow can greatly reduce the accuracy of 1D solutions (Roshan et al. 2012, Lautz 2010). Lautz (2010) showed that higher ratios of vertical to horizontal velocity magnitude lead to larger percent errors in flux estimations, indicating that SW/GW interactions are a multi-dimensional problem. The idea of non-vertical flows being a source of error was ubiquitous in the heat-as-a-tracer literature until Cuthbert and Mackay (2013) showed that nonparallel flow fields are more likely to be responsible for errors than non-vertical flow alone. In an idealized steady-state system with a sinusoidal upper temperature boundary, a homogenous substrate, parallel multi-dimensional groundwater flow paths and low enough Darcy velocities to ignore hydrodynamic dispersion, 1D heat-as-a-tracer methods should be able to extract the vertical component of groundwater flow (Cuthbert and Mackay 2013). At any given point in this system, heat is transported horizontally and vertically via advection, and vertically via conduction. Since groundwater flows are parallel, the amount of heat advected horizontally into any given point in the system is identical to the amount of heat advected horizontally away from that point. Thus, there is no horizontal temperature gradient, the horizontal component of flow can be neglected and a 1D analytical model can be applied to the system to solve for vertical conduction and advection.

To date, no work to our knowledge has explored the effects of three-dimensional, non-uniform flow fields on the performance of heat-as-a-tracer to quantify 1D vertical fluxes. However, three-dimensional groundwater flow patterns have been observed in the field (e.g. Derx et. al. 2010). Roshan et al. (2010), Lautz (2010) and Cuthbert and Mackay (2013) have explored the effects of two-dimensional flows on the performance of the Hatch et al. (2006) equations for both two-dimensional transverse and longitudinal to surface flow conditions. In natural systems, regional groundwater gradients or changes in bank storage may cause groundwater flow paths to contain both a longitudinal and transverse flow component. These multi-dimensional flow fields can result in non-horizontal isotherms, thus violating the 1D groundwater flow assumption. When groundwater flows contain a significant horizontal flow component that does not change with depth, three-dimensional flow fields can be modeled in two dimensions using radial coordinates (e.g. Lautz 2010, Cuthbert and Mackay 2013). However, flow fields may not be parallel in natural systems (Cuthbert and Mackay 2013). Non-uniform flow fields, where velocity vectors change with depth, may lead to temperature gradients, not necessarily parallel to the advective thermal front, causing 2D models to be a potential oversimplification of natural systems.

In order to address the impacts of multi-dimensional flow fields, we present a partially coupled model of groundwater flow and heat transport. The purpose of this research is 1) to test how well 1D thermal methods for quantifying SW/GW interactions perform in the presence of nonvertical, and drastically non-uniform flow fields, and 2) to determine if any multi-dimensional information can be extracted from 1D temperature records in a laboratory setup with a homogenous substrate. The results from this model will be used to inform experiments in a laboratory setup.

I.1 Theory

The 1D transport of heat in a saturated, homogeneous, porous media is governed by (e.g., Carslaw and Jaeger 1959, Bredehoeft and Papadopulos 1965, Stallman 1965):

$$\frac{\partial T}{\partial t} = \kappa_e \frac{\partial^2 T}{\partial t^2} - q \frac{\rho_w c_w}{(\rho c)_b} \frac{\partial T}{\partial z} \tag{1}$$

where T is temperature that can vary with time, t, and depth, z. q is the Darcy flux, κ_e is the effective thermal diffusivity, and ρ_w and c_w are the density and specific heat capacity of the fluid, respectively. $(\rho c)_b$ is the bulk volumetric heat capacity defined as: $(\rho c)_b = n\rho_w c_w + (1-n)\rho_s c_s$ where n is porosity and subscripts w and s denote properties of the fluid and solid matrix, respectively. Ignoring the effects of dispersion, κ_e is calculated as (modified from Ingebritsen and Sanford, 1998):

$$\kappa_e = \frac{\lambda_0}{(\rho c)_b} \tag{2}$$

where λ_0 is the effective thermal conductivity of the saturated system, $\lambda_0 = {\lambda_w}^n {\lambda_s}^{(1-n)}$ where λ_w and λ_s are the thermal conductivities of the fluid and porous solid, respectively (Hatch et al. 2006). The closed-form, transient, analytic solution to equation 1 in the presence of a sinusoidal temperature signal at the surface and vertical fluid flow is (modified from Stallman, 1965 and Goto 2005):

$$\mathrm{T}(\mathrm{z},\mathrm{t}) = \mathrm{A}\exp\left(\frac{\mathrm{v_t z}}{2\,\kappa_{\mathrm{e}}} - \frac{\mathrm{z}}{2\,\kappa_{\mathrm{e}}}\sqrt{\frac{\alpha+\mathrm{v_t}^2}{2}}\right)\cos\left(\frac{2\pi\mathrm{t}}{\mathrm{P}} - \frac{\mathrm{z}}{2\,\kappa_{\mathrm{e}}}\sqrt{\frac{\alpha-\mathrm{v_t}^2}{2}}\right) \tag{3}$$

where A is the amplitude and P is the period of the sinusoidal temperature forcing at the surface, $\alpha = \sqrt{{v_t}^4 + \left(\frac{8\pi\kappa_e}{P}\right)^2}$ and $\mathrm{v_t}$ is the advective thermal front velocity defined as $v_t = q\,\frac{C_w}{C_b}$ where $c_b = c_w * n + c_s * (1-n)$ (Briggs et al. 2014). We use the convention of positive values of q to indicate downward flow, and negative, upward (e.g. Briggs et al. 2014).

Stallman's (1965) work marked an important historic contribution turning heat from exclusively a water quality parameter to a measurable input for quantification of flux (Rau et al. 2014). Hatch et al. 2006 separated the diurnal signal from filtered temperature time series into two separate components, ratio of amplitude attenuation, $A_r = \frac{A_{deep}}{A_{shallow}}$, and phase shift, $\Delta\Phi = \Phi_{deep} - \Phi_{shallow}$, to iteratively solve for fluid velocity:

$$\mathrm{A_r} = \exp\left\{\frac{\Delta\mathrm{z}}{2\,\kappa_{\mathrm{e}}}\left(\mathrm{v_t} - \sqrt{\frac{\alpha+\mathrm{v_t^2}}{2}}\right)\right\} \tag{4}$$

$$\Delta\Phi = \frac{\mathrm{P}\Delta\mathrm{z}}{4\pi\,\kappa_{\mathrm{e}}}\left(\mathrm{v_t} - \sqrt{\frac{\alpha-\mathrm{v_t^2}}{2}}\right) \tag{5}$$

Equations 4 and 5 can be rearranged to solve for Darcy velocity:

$$\mathrm{q_{A_r}} = \frac{(\rho\mathrm{c})_\mathrm{b}}{\rho_\mathrm{w}\mathrm{c_w}}\left(\frac{2\,\kappa_{\mathrm{e}}}{\Delta\mathrm{z}}\ln\mathrm{A_r} + \sqrt{\frac{\alpha+\mathrm{v_t^2}}{2}}\right) \tag{6}$$

$$|\mathrm{q_{\Delta\Phi}}| = \frac{(\rho\mathrm{c})_\mathrm{b}}{\rho_\mathrm{w}\mathrm{c_w}}\sqrt{\alpha - 2\left(\frac{4\pi\Delta\Phi\,\kappa_{\mathrm{e}}}{\mathrm{P}\Delta\mathrm{z}}\right)^2} \tag{7}$$

This method has become common-practice to extract fluid velocity from temperature records at multiple depths (Rau et al. 2010; Swanson and Cardenas 2010; McCallum et al. 2012).

When dispersivity is ignored, Equations 4 and 5 become identical to the solutions presented in Keery et al. (2007). Recent work has developed equations to solve for fluid flow and effective thermal diffusivity using both amplitude and phase information from temperature signals (McCallum et al. 2012, modified from Luce et al. 2013):

$$q_{A_r\Delta\Phi} = \frac{(\rho c)_b}{\rho_w c_w}\frac{\omega\eta\Delta z}{-\ln(A_r)}\left(\frac{1-\eta^2}{1+\eta^2}\right) = \frac{(\rho c)_b}{\rho_w c_w}\frac{\omega\Delta z}{\Delta\Phi}\left(\frac{1-\eta^2}{1+\eta^2}\right) \tag{8}$$

$$\kappa_e = \frac{\omega\Delta z^2}{\Delta\Phi^2(\frac{1}{\eta}+\eta)} = \frac{\omega\eta^2\Delta z^2}{\ln^2(A_r)(\frac{1}{\eta}+\eta)} \tag{9}$$

where: $\eta = \frac{-\ln(A_r)}{\Delta\Phi}$ and ω is the angular frequency such that $\omega = 2\pi/P$. Temperature derived effective thermal diffusivity can be used as a metric for violation of the assumptions of 1D heat-as-a-tracer methods for calculating flux (McCallum et al. 2012). McCallum et al. (2012) used a similar formulation for effective thermal diffusivity as Luce et al. (2013) and showed that a transient head boundary resulted in erroneous results for κ_e. Violation of the assumptions used for temperature-derived estimates of 1D flux results in changes in the way the diurnal signal propagates through the subsurface (e.g. Cuthbert and Mackay 2013, Briggs et al. 2014). Equation 9 uses the same phase and amplitude information from temperature time series as Equations 6, 7 and 8, so that when temperature derived κ_e estimates are erroneous, estimates of flux can be unreliable as well. Using effective thermal diffusivity as a metric for violation of the assumptions of temperature-derived estimates of 1D flux only works when we know the true value of effective thermal diffusivity. Calculating this parameter becomes more difficult in heterogeneous natural systems.

CHAPTER 1

METHODS

Synthetic temperature time series at multiple depths from multi-dimensional flow fields were generated using the finite element solver, COMSOL Multiphysics, in a one-meter cube of fully-saturated, homogeneous coarse quartz sand (Figure 1, Figure 2). COMSOL is designed to solve systems of differential equations under a variety of boundary conditions (COMSOL, Inc., Burlington, MA, USA; see www.comsol.com). The model contains 60,500 mesh elements with a minimum mesh element edge length of 1.6 cm (Figure 2). The mesh selected is finest near the inflow boundaries and through a center column extending 55 cm into the model to capture the highest temperature gradient and to refine the grid in the section of the model where the data analysis is taking place. This refinement allows for a maximum RMS error to be less than 0.003°C along the vertical centerline of the model when compared to the 1D analytical solution to Equation 3 with the same boundary conditions (Appendix D). For this comparison, the maximum Darcy velocity observed in any model run was used to verify model stability and accuracy with the known analytical solution. The error in the model due to interpolation between mesh elements is well within the accuracy range of typical temperature sensors used in the field. Onset Stowaway and Hobo Tidbit temperature sensors only have a reported accuracy of 0.15°C. A time step of 15 minutes was selected to maintain a high frequency sampling rate while still maintaining less than 0.003°C error when compared to Equation 3. Thermal and hydraulic properties of the sediment and fluid are outlined in Table 1.

1.1 Generate Groundwater Flow Fields

We modeled steady-state groundwater flow in a laboratory setup to simulate a streambed by solving Darcy’s law coupled with the continuity equation:

$$0 = S\frac{\delta \mathrm{h}}{\delta \mathrm{t}} = K\nabla^2 h = K\left[\frac{\delta^2 h}{\delta x^2} + \frac{\delta^2 h}{\delta y^2} + \frac{\delta^2 h}{\delta z^2}\right] \quad (10)$$

where S is storativity, K is hydraulic conductivity, h is hydraulic head, t is time and x, y and z are the orthogonal axes of the model. We assume that the laboratory streambed system we are modeling is homogeneous and isotropic. Although this is possible in a laboratory setup, it is unlikely in a natural setting. This allows us to independently investigate the effects of multi-dimensional groundwater flows and generate consistent non-uniform groundwater flows without preferential flow paths. We used volumetric displacement and a standard Darcy column experiment to determine an initial estimate of porosity and hydraulic conductivity, respectively, using a coarse, well-sorted filter-pack sand to be added to a laboratory setup (Table 1). The sand has a median diameter of 3 mm and is 99% quartz in composition.

Groundwater flow fields were generated by specifying a constant hydraulic head of 20 cm to three sides of the cube, and specifying various outlet fluxes to the remaining three sides of the volume. These boundary conditions were selected based on the design of a laboratory setup to simulate groundwater flow. Specific outlet velocities exiting the model are outlined in Appendix A for the 11 losing and 10 gaining simulations. This set of hydraulic boundary conditions generates a range of horizontal and vertical velocities such that q_x, q_y and q_z change with depth, creating three-dimensional non-uniform flow fields. Both gaining and losing conditions were tested to compare the use of the heat-as-a-tracer methods for quantifying flow under a range of fluxes, which could potentially occur in a natural system (e.g. Briggs et al. 2012, Gordon et al. 2013, Rau et. al. 2010). Since the heat-as-a-tracer method for quantifying flow assumes a 1D uniform flow field, increasing horizontal velocities and changing flow fields with depth should cause error for temperature derived estimates of flux.

1.2 Apply Diurnal Temperature Variations

After solving for fluid flow in COMSOL, transient heat flow was simulated in the volume consistent with assumptions of previous work (Irvine et al. 2015, Cuthbert and Mackay 2013) using the advection-diffusion equation in three dimensions:

$$\frac{\delta \mathrm{T}}{\delta \mathrm{t}} = \kappa_e \nabla^2 \mathrm{T} - q \frac{\rho_w c_w}{(\rho c)_b} \nabla \mathrm{T} \tag{11}$$

Diurnal temperature variations of a stream system were modeled by applying a sinusoidal temperature variation to the top of the cube: $T = A \cos\left(\frac{2\pi t}{P}\right) + T_0$. The initial temperature condition of the model, T_0, is 19.85°C and the amplitude A used for all model runs was 2°C. We assumed no change in groundwater temperature at depths greater than 1 m and a constant temperature boundary was specified at the bottom of the cube of T_0. Thermal insulation temperature boundaries are set to the remaining four sides of the cube such that $\hat{n} \cdot (\kappa_e \nabla T) = 0$ and no heat flux occurs across the model boundary where $\hat{n}$ is the normal vector to that boundary. These thermal conditions were selected such that the thermal conditions in the model match up with the assumptions used for quantifying flux from temperature time-series. Each model run lasts for 10 days allowing the model to equilibrate to “quasi-steady state” so that the amplitude and phase shift at each observation node has equilibrated to a constant value. We assumed local thermal equilibrium between solid and liquid phases and ignored the effect of temperature on fluid density, despite its known impact on hydraulic conductivity (Lautz 2012). This was justified because the maximum and minimum temperatures occurring at any point in the model differed by less than 4° C, causing density impacts to be negligible for the purposes of this study (Appendix E). We ignored hydrodynamic dispersion since thermal Peclet numbers were less than 0.078 for each model run (Appendix F) (Rau et al.2012). The thermal Peclet number is a dimensionless parameter which describes the ratio of convective heat transport to conductive heat transport. Peclet numbers less than one generally indicate conduction dominated systems (Huysmans and Dassargues 2005). Literature values for the thermal properties of the saturated sediment are outlined in Table 1. The laboratory sand used to calculate hydraulic conductivity and porosity was 99% quartz in composition. As a result, we used the thermal properties of quartz for our simulations (Table 1). The thermal conductivity of the saturated porous media is 2.92 W/(m°C) and agrees with literature values (Tarnaski et al. 2011).

1.3 Calculate Temperature Derived Fluxes

We extracted temperature time series at observation nodes at depths of 10, 20, 25, 40 and 50 cm from the surface along the vertical centerline of the model (Figure 2). We extracted phase and amplitude information from temperature time-series from pairs of observation nodes using VFLUX and resampled into two-hour intervals creating 8 temperature derived flux estimations per time step per trial and 168 calculations of flux total (Gordon 2012). VFLUX is a MATLAB script that filters temperature time series using dynamic harmonic regression, via the Captain Toolbox, to extract phase and amplitude information to calculate vertical groundwater fluxes (Taylor et. al 2007). In order to avoid filtering artifacts, we used a sampling rate of 12 samples per period of the diurnal temperature signal, in this case, 12 2-hour samples per each day (Gordon et al. 2012). We averaged the last day of flux calculations, consisting of 12 time steps, to eliminate any effects of the initial conditions of the model. When the modeled amplitude at each temperature observation node changed by less than our selected tolerance of 0.003°C, we concluded that model runs had reached equilibrium. This occurred within the first 9 days for all model runs.

1.4 Compare Temperature Derived Fluxes to Known Fluxes and Error analysis

We compare thermally derived Darcy velocities using Equations 6, 7 and 8 to the known modeled Darcy velocity at the center depth between two observation nodes. The center depth for each analysis was set as the arithmetic mean of the absolute depths of the two temperature observations nodes. Error was calculated as $Error = q_M - q_T$ where the subscripts M and T refer to the knwon vertical Darcy velocity at the midpoint between the two temperature observation nodes in the model and the temperature derived vertical flux between those same nodes, respectively. We compare the performance of Equations 6, 7 and 8 in response to the degree of non-uniformity, and the magnitude of horizontal flow. We can use the amount of convergence or divergence of a flow field between two sensors, $\frac{dq}{dz}$ as a metric for flow non-uniformity:

$$\frac{dq}{dz} = \frac{|q_d| - |q_s|}{z_d - z_s} = \frac{\sqrt{(q_x{}^2 + q_y{}^2 + q_z{}^2)_d} - \sqrt{(q_x{}^2 + q_y{}^2 + q_z{}^2)_s}}{z_d - z_s} \tag{12}$$

where q is the Darcy velocity and z is the depth of the observation node. The subscripts s and d refer to the shallow and deep observation nodes for a given flux calculation, respectively, and x, y, and z refer to the orthogonal axes of the model. Equation 12 is used to quantify how much a given groundwater flow field changes over the vertical distance between two temperature observation nodes. Increasing values of $\frac{dq}{dz}$ indicate larger changes in the velocity vectors between two temperature observation nodes, and thus, increasing non-uniformity for a given flow field. The magnitude of the horizontal Darcy velocity, q_h, can be calculated as $q_h = \sqrt{q_x{}^2 + q_y{}^2}$.

Thermally derived κ_e, calculated using Equation 9, was compared to the “true” (model-input) value of κ_e as:

$$Percent\ Error\ \kappa_e = \frac{\kappa_{eM} - \kappa_{eT}}{\kappa_{eM}} * 100\% \tag{13}$$

where $\kappa_{e\,M}$ and $\kappa_{e\,T}$ are the modeled and thermally-derived effective thermal diffusivity, respectively.

CHAPTER 2

RESULTS

From the COMSOL-generated steady state flow fields, we extracted the vertical Darcy flux, q_z, occurring at the midpoint between temperature observation nodes. For the 21 flow fields and 8 different spacings of temperature observation nodes, we generated 168 estimates of temperature-derived flux and effective thermal diffusivity. Values of q_z ranged from -0.85 m/d for gaining flow geometries to 1.57 m/d for losing flow geometries. Horizontal Darcy fluxes at the same locations, q_h, ranged from 0.03 to 1.03 m/d (Figure 3). Larger magnitudes for upwelling fluxes (greater than ~0.4 m/d) were not tested since the diurnal temperature signal was extinguished below the model resolution at depths of 50 cm or greater.

We then compared thermal derived velocities using the amplitude ratio (Equation 6), phase shift (Equation 7), and the combined amplitude ratio phase shift methods to the COMSOL-generated velocities (Equation 8). In general, the phase shift method (Equation 7) did not accurately calculate fluxes. When Darcy velocities approach zero, the phase shift curves have a shallow slope and are less sensitive to changes in Darcy velocity (Figure 4b). The amplitude ratio curves have a higher slope, and thus a greater sensitivity than the phase shift over the range of vertical fluxes tested (Figure 4a). Equation 8 matched known Darcy velocities better than the phase shift derived velocities but substantially worse than amplitude ratio derives velocities. This is most likely due to the decreased sensitivity of the phase shift over the Darcy velocities tested (Figure 4b). 96% of the calculations using Equation 6 had lower errors than the combined amplitude ratio-phase shift method (Equation 8).

The remainder of the results will focus on amplitude ratio derived fluxes, since Equation 6 performs consistently better than Equations 7 and 8 (Figure 5). For losing flow geometries, both Equations 6 and 8 consistently under predicted the vertical Darcy flux (Figure 6). For gaining flow conditions, the magnitude of the temperature derived Darcy flux was also consistently less than the modeled Darcy flux between the two observation nodes. The maximum errors for flux calculations using Equation 6 were 1.1 m/d for losing flow geometries and 0.59 m/d for gaining flow geometries. For losing conditions, increasing horizontal Darcy flux magnitude is correlated with increasing error in flux estimates for both the amplitude ratio method (R^2=0.81) and the combined amplitude ratio phase shift method (R^2=0.87). For the gaining fluxes tested, the correlation is much weaker for both Equation 6 (R^2=0.22) and Equation 8 (R^2=0.21).

Amplitude ratio derived flux calculations were ignored when they inaccurately predicted the direction of flow. This occurred only in the case of the most strongly gaining flow field where the vertical velocity ranged from -0.78 m/d at 15 cm depth to

-0.514 m/d at 45 cm depth. For this trial , the amplitude of the diurnal temperature signal at temperature observation nodes 40 cm depth or greater was less than 0.01°C. Thus, 5 calculations of flux were ignored reducing the total number of estimations used in our analysis to 163.

2.1 Non-uniform flow as a source of error

When flow fields are uniform, 1D heat-as-a-tracer methods can extract the vertical component of flow (Cuthbert and Mackay 2013). Conversely, there should be more error when the flow field becomes more non-uniform. Figure 7 shows a correlation of increasing error with increasing magnitude of $\frac{dq}{dz}$ for both losing (R^2= 0.80) and gaining (R^2= 0.86) flow fields. The three gaining data points with the largest $\frac{dq}{dz}$, and largest error, had upwelling magnitudes greater than 0.5 m/d and horizontal magnitudes of 0.8 m/d. The maximum magnitude of $\frac{dq}{dz}$ calculated was 3.8 d^{-1}, equivalent to an 18.2% change in Darcy velocity magnitude between the shallow and deep observation nodes. However, the maximum change in Darcy velocity magnitude between two observation nodes was 44.8%.

2.2 Effective thermal diffusivity as a metric for violation of heat-as-a-tracer assumptions

In the case of losing flow geometries, a strong linear trend (R^2= 0.94) exists between Darcy velocity error (in meters per day) and percent error in effective thermal diffusivity (Equation 13) (Figure 8). For gaining stream systems, there almost no correlation. Temperature derived κ_e from gaining groundwater flow fields consistently over predicted κ_e by up to 62%, while losing flow fields, under predicted by as much as 240%. Figure 9 shows a general trend of increasing error in κ_e with increasing magnitude of horizontal flow for losing flow geometries (R^2= 0.67). Error for κ_e is more sensitive to changes in horizontal flow magnitude for losing flow geometries than for gaining flow geometries.

2.3 Do thermal methods reproduce modeled fluxes?

Figure 10 shows flux calculations where the amplitude ratio derived flux is within the range of fluxes occurring between the shallow and deep observation nodes. Calculations where q_{AR} is less than 0.006 m/d different from the maximum or minimum velocities occurring in that range were also included in Figure 10. This tolerance was selected since it is the maximum amount of error introduced by VFLUX over this range of vertical velocities (Appendix I). ~93% of the temperature-derived fluxes using Equation 6 calculate a vertical Darcy velocity outside the range of the modeled velocity of the shallow and deep observation nodes. When the tolerance of 0.006 m/d is included, the number of amplitude ratio derived fluxes outside the range of vertical velocities at the shallow and deep sensor reduces to ~85%.

For this 15% of flux calculations where the amplitude ratio derived velocity is within 0.006 m/d of the range of known modeled velocities between the shallow and deep observation node; q_h

ranged from 0.03 to 0.88 m/d at the center depth, q_z at the center depth ranged from -0.16 to 0.3 m/d at the center depth and dq/dz ranged from -0.19 to 0.64 (d^{-1}).

CHAPTER 3

DISCUSSION

When quantifying 1D flux from temperature time series, two unanswered questions are, 1) can heat-as-a-tracer be used in practice when field conditions rarely meet the assumptions of the methods used? And 2) can 1D methods be used to extract any useful information about multi-dimensional flow paths? When temperature time series are collected as field data, substantial, additional hydrologic information is required to determine whether a 1D temperature model is appropriate. However, it is possible that 1D temperature records may contain some information about the multi-dimensionality of a given flow field. We examined the performance of 1D heat-as-a-tracer methods in response to non-vertical, non-uniform groundwater flows.

Over the range of vertical Darcy velocities tested, the phase shift method has a decreased sensitivity to changes in Darcy velocity (Figure 4b). This poses a problem since for a given phase shift extracted from two temperature time series, minor variations in the phase shift will result in drastically different Darcy velocities. As a result, we focused on the performance of Equation 4.

3.1 Non-uniform flow as a source of error

In natural systems, we can expect groundwater flow paths to converge or diverge at the sediment-water interface (Cuthbert and Mackay 2013). Deep groundwater flows driven by regional gradients interact with shorter length flow paths, driven by stream morphology, such as pool-riffle sequences (Swanson and Cardenas 2010) and channel bedforms (Janssen et al. 2012). These interactions of varying length scale flows can result in non-uniform groundwater flow paths. Within this framework at a finer spatial scale, changes in streambed hydraulic conductivity, due to changes in clast size or organic materials, can cause preferential and non-parallel groundwater flow paths (e.g. Sawyer et al. 2012, Irvine et al. 2015). The flow fields generated were drastically non-uniform such that there are large changes in velocity, and thus large thermal variations in a small space. These flow fields generate represent extreme conditions and can be considered a worst case scenario for flow non-uniformity.

For gaining conditions, the correlation between q_h and the magnitude of error is weaker (Figure 5). In the case of upwelling, advective heat transport is moving in opposition to conductive heat transport (Briggs et al. 2014). The unique physics of gaining flow fields may be responsible for this weaker correlation. The three gaining data points with the largest errors are visible in Figures 5, 7, 8 and 9. This flow geometry is expected to produce larger errors since there is a large horizontal velocity component and a high degree of flow non-uniformity.

For losing conditions, in the presence of non-uniform multi-dimensional groundwater flow paths, both the magnitude of the horizontal velocity component and the degree of non-uniformity are correlated with errors in temperature-derived fluxes (Figure 7). Thus, the presence of a horizontal velocity component, leading to a multi-dimensional flow field, is likely to cause inaccurate temperature derived fluxes since it is improbable that non-vertical, parallel groundwater flow paths exist in surface water settings (Cuthbert and Mackay 2013). Many calculations had greater horizontal flow magnitudes than vertical magnitudes, but this was not a controlling factor on the amount of error. Additionally, VFLUX can introduce errors in flux by up to 0.006 m/d (Appendix I). Although this would not effect the general trends presented above, the filtering and resampling process used in VFLUX could easily alter relative magnitudes of error by up to 0.006 m/d for vertical fluxes between -0.1 and 1 m/d. For fluxes outside this range, VFLUX may introduce larger errors.

3.2 Effective thermal diffusivity as a metric for violation of heat-as-a-tracer assumptions

Identifying a multi-dimensional groundwater flow field at a given field site can be used to determine that a 1D estimate of flux generated using heat-as-a-tracer may be erroneous. However, measuring the magnitude of horizontal velocity in the field relies on estimating hydraulic conductivity and is difficult to validate. Fortunately, effective thermal diffusivity (κ_e) derived from temperature time series has potential to work as a test for violation of the underlying assumptions used to calculate flux from temperature time-series. Since effective thermal diffusivity can be constrained relatively well in the field (Goto 2005, Shanafield et al. 2011), large variations in temperature-derived κ_e over time when κ_e should be relatively constant may indicate changes in stage of the river system (McCallum et al. 2012). When temperature derived κ_e is relatively constant but significantly different from known values, non-uniform, non-vertical groundwater flow fields may be responsible for inaccurate values of temperature-derived κ_e. It is worth noting that other violations of the assumptions used to calculate groundwater velocity from temperature time-series, such as the presence of a thermal gradient with depth (Briggs et al. 2014) or a heterogeneous substrate (Irvine et al. 2015), could cause errors in temperature derived κ_e. For both losing and gaining modeled flow geometries, errors in temperature-derived κ_e are strongly correlated with errors in amplitude ratio derived fluxes. Therefore, we can use errors in temperature-derived κ_e, in addition to measurement of horizontal flux, as another line of evidence for the presence of non-vertical flows, and thus, inaccurate temperature derived fluxes.

For 10% of the flux calculations, VFLUX incorrectly identified correlated peaks in the thermal records resulting in negative phase shifts. Flux (Equation 8) and effective thermal diffusivity calculations (Equation 9) were ignored in our analysis when VFLUX extracted negative phase shift values from the temperature time series. These failures in the solver were likely as a result of forward biasing in the dynamic harmonic regression process (Rau et al. 2015). This occurred in vertical flow fields, as well as multi-dimensional flow fields (Appendix I). Over the range of fluxes tested, VFLUX may introduce errors of up to 3.2% for temperature derived κ_e.

3.3 Do thermal methods reproduce modeled fluxes?

When a pair of temperature sensors is used to extract a fluid velocity, the sensors integrate the thermal conditions of the saturated sediment system over the distance between the two sensors. When vertical velocities change between the temperature sensor pair, the 1D uniform flow field assumption is violated. Only 7% of temperature derived fluxes were within the range of known fluxes between the maximum and minimum temperature observation nodes. Over this range of vertical velocities tested, VFLUX can introduce errors in flux estimates which under estimate the magnitude of flux by up to 0.006 m/d (Appendix I). If a tolerance of 0.006 m/d is used, up to 15% of amplitude-ratio derived fluxes could potentially fall within the range of the velocities occurring between the shallow and deep temperature observation node. For the purpose of calculating error for our analysis, we assume that temperature derived velocities are equivalent to the Darcy velocity at the midpoint between the two temperature observation nodes (Irvine et al. 2015). However, when errors are low for temperature-derived velocities, Equation 6 produces fluxes which more closely resemble the lesser magnitude flux occurring between two observation nodes. This suggests that in the presence of multi-dimensional groundwater flow fields, the amplitude ratio method may integrate the thermal transport properties of the saturated system as a harmonic mean, and the weakest magnitude velocity found within the temperature sensor pair may be the controlling factor for propagating the surface temperature signal (Figure 10). An alternative explanation is that since both losing and gaining modeled flow geometries result in an under-prediction of the known flux, these thermal derived estimates may trend towards the minimum of the range occurring between the shallow and deep temperature observation nodes.

For this series of multi-dimensional, non-uniform flow fields, even with a pure, sinusoidal temperature upper boundary and a homogeneous, isotropic substrate, temperature derived velocities rarely fall within the range of actual velocities occurring between a given pair of temperature sensors. It is worth noting that the flow fields modeled here are drastically non-uniform. Changes in the vertical velocity throughout the model cause the thermal front (i.e.

isotherms) to propagate through the model non-horizontally. These sloped thermal contours, caused by a non-uniform flow field, represent a violation of the 1D uniform flow field assumption and are responsible for causing the errors in these 1D estimates of flux. In the flow geometries resulting in high errors for thermally-derived estimates of flux, measuring a temperature profile 30 cm away would generate a different thermally derived estimate of flux. It is possible that some of these temperature profiles may vary spatially more than one would expect in a field setting. Therefore, it is crucial for these results to be tested in a controlled laboratory setting before applying the results of this study to field data.

CONCLUSIONS

This study attempts to quantify the ability of methods employing heat-as-a-tracer to quantify 1D flows for SW/GW interactions in three dimensional, non-uniform flow geometries. By comparing known groundwater fluxes in the model to fluxes extracted from temperature records at pairs of depths, we assessed the effects of the magnitude of horizontal velocity and the degree of convergence or divergence for a given groundwater flow field. We found that the presence of a horizontal flux component in addition to some degree of convergence or divergence for a given flow field is correlated with the amount of error for both gaining and losing modeled flow geometries. When a substantial horizontal velocity component exists, erroneous values of temperature-derived effective thermal diffusivity appeared to result in errors in amplitude ratio derived Darcy velocities. In the presence of drastically non-uniform, multi-dimensional groundwater flow fields, temperature derived fluxes rarely fall within the range of velocities between a given pair of temperature sensors. Further studies can verify our preliminary impression that heat-as-a-tracer methods integrate the thermal properties of the saturated system as a harmonic mean to determine where temperature sensor pairs calculate fluxes. The results of our simulations should now be tested in a controlled laboratory setting before applying these results to field data.

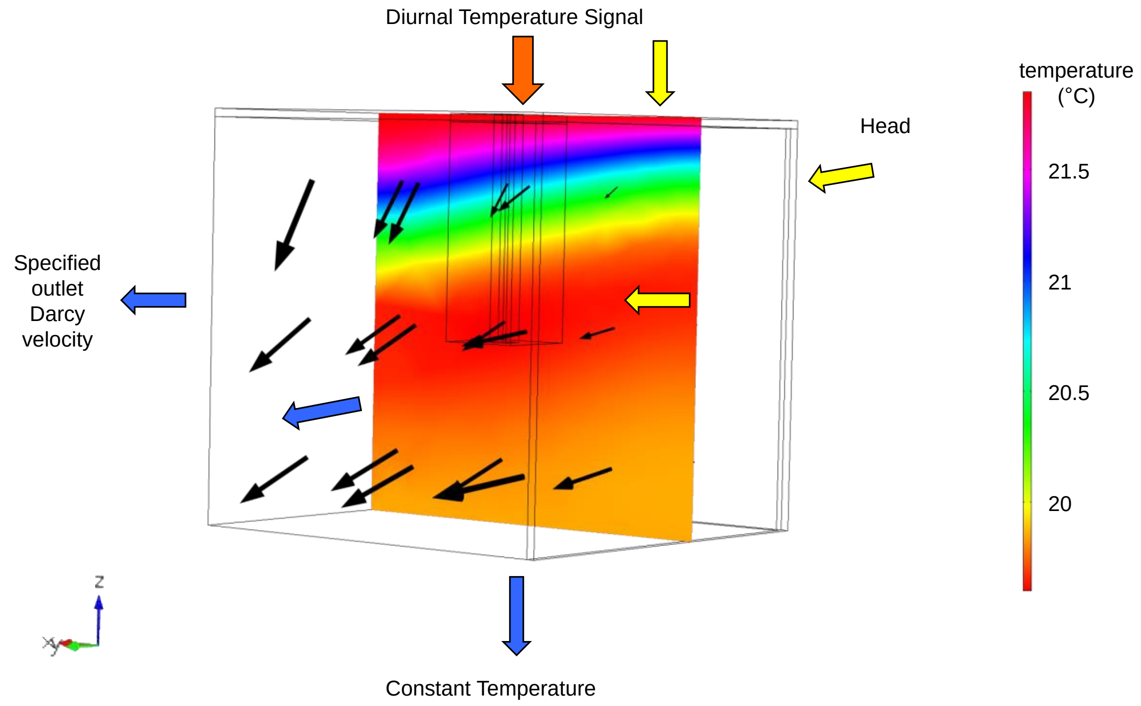

Figure 1: Model domain with color map slice showing temperature (°C) at time t=10 days for a given flow field, boundary conditions and the orthogonal axis of the model (bottom left). All sides of the cube are 1 m in length. Black arrows indicate flow direction. Columns in the center of the model and rectangles at the edge indicate areas where mesh is refined. A diurnal temperature signal (orange arrow) is applied to the top of the model and a constant temperature boundary is applied to the bottom. Sides of the model are set as no heat flux. Constant head boundaries are applied to three sides of the model (yellow arrows) with specified outlet velocities applied to the remaining three sides (blue arrows). Note that for gaining conditions, a constant head is applied to the bottom, and a specified flux exits the top of the model.

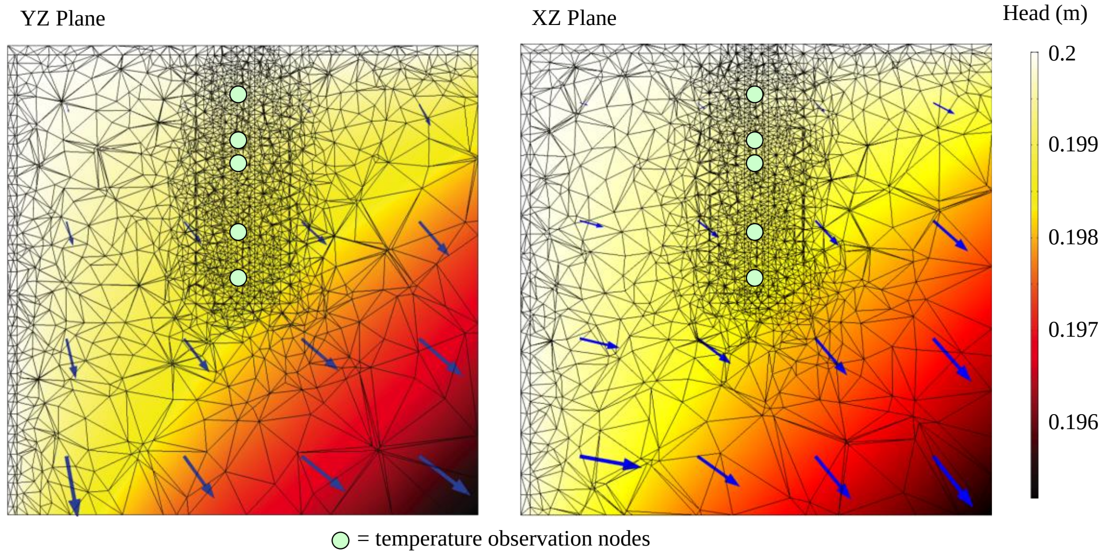

Figure 2: 2D cross sections through the center of the model showing mesh discretization. Each cross section has dimensions 1 m by 1 m. The left image is on a center plane through the model parallel to the X-axis and the right image is parallel to the Y-axis. Color map represents hydraulic head in meters and arrows indicate flow direction for the same example flow field as Figure 1. To generate this flow field, a constant head of 0.2 m was applied to the top and left side of the model and outlet fluxes of 1 m/d were applied to the bottom and right side of the model. Mesh is refined on the inlet sides of the model and through a center column where the data analysis takes place. Green circles indicate depths (10, 20, 25, 40 and 50 cm) at which temperature time series were extracted.

Table 1: Values for hydraulic and thermal model parameters.

Parameter	**Value**
Hydraulic conductivity[1]	240 m/d
Porosity[1]	0.4
Density water[2]	998 kg/m^3
Specific heat capacity water[2]	4184 J/kg*K
Density quartz[2]	2650 kg/m^3
Specific heat capacity quartz[2]	800 J/kg*K
Thermal conductivity quartz[2]	8.4 W/m*K
Thermal conductivity water[2]	0.6 W/m*K

Note: Parameter values were either estimated via laboratory experiments[1] or taken from van Wijk and de Vries (1966)[2].

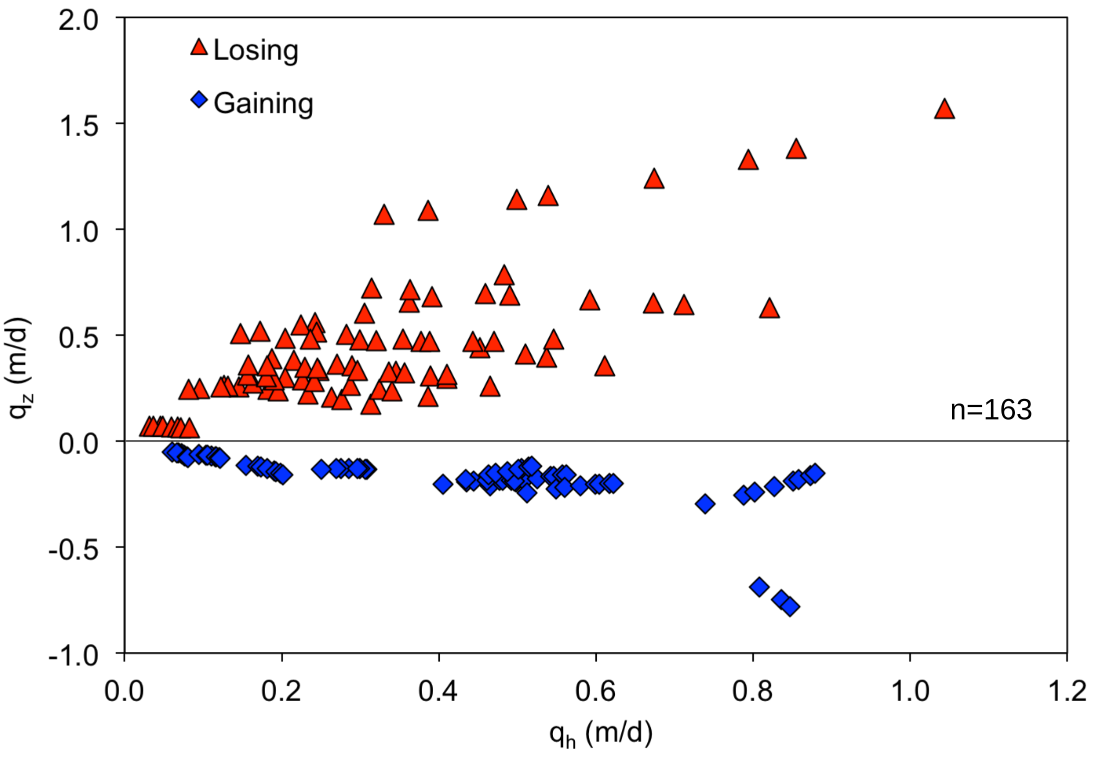

Figure 3: Range of known horizontal (q_h) and vertical (q_z) Darcy velocities in the model. Darcy velocities were recorded at the center depth between observation nodes for losing (red triangle) and gaining (blue diamond) conditions. Negative values of q_z indicate gaining conditions and positive values indicate losing conditions.

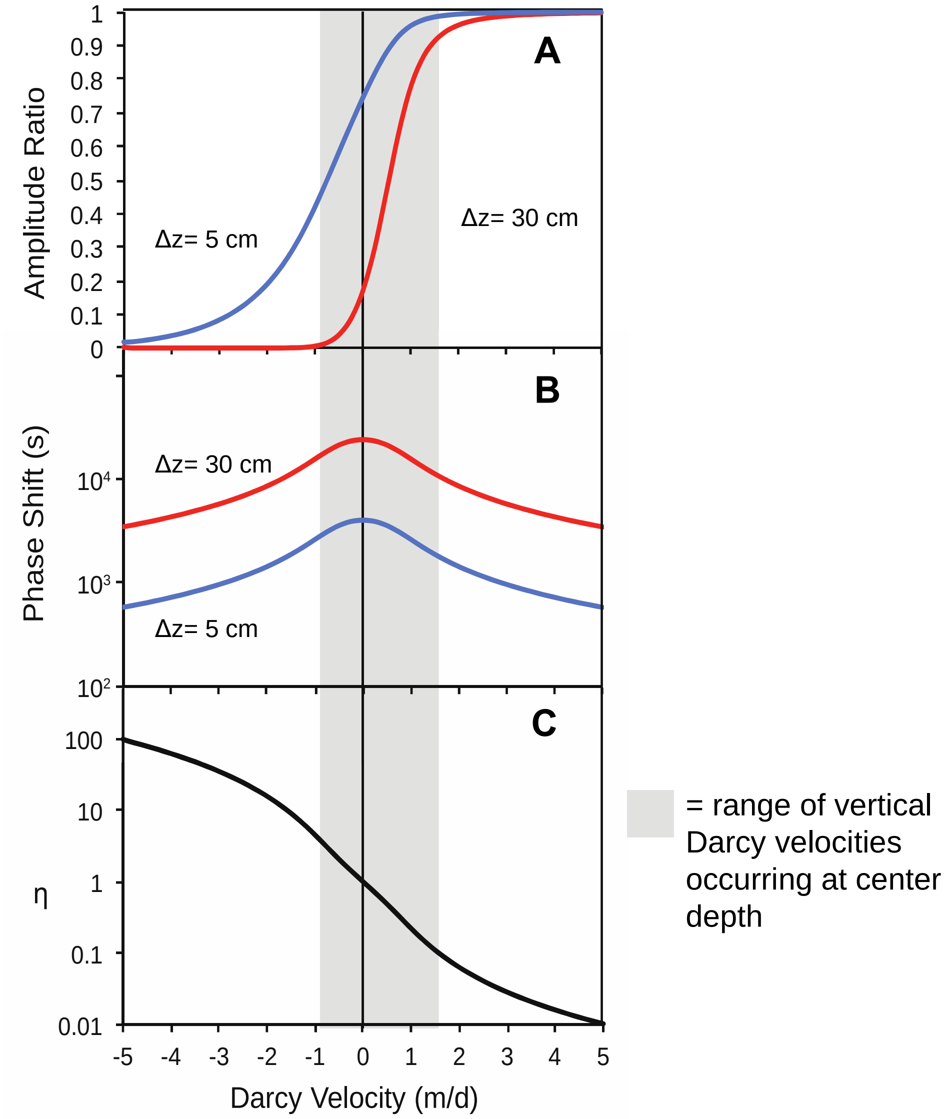

Figure 4: Solution space for amplitude ratio (A), phase shift (B), and combined amplitude ratio/phase shift parameter η (C) for the maximum (red line) and minimum (blue line) spacing between observation nodes tested. Darcy velocities tested in this study are outlined in gray. Negative values of Darcy velocity indicate gaining conditions and positive values indicate losing conditions. η is not sensitive to changes in Δz.

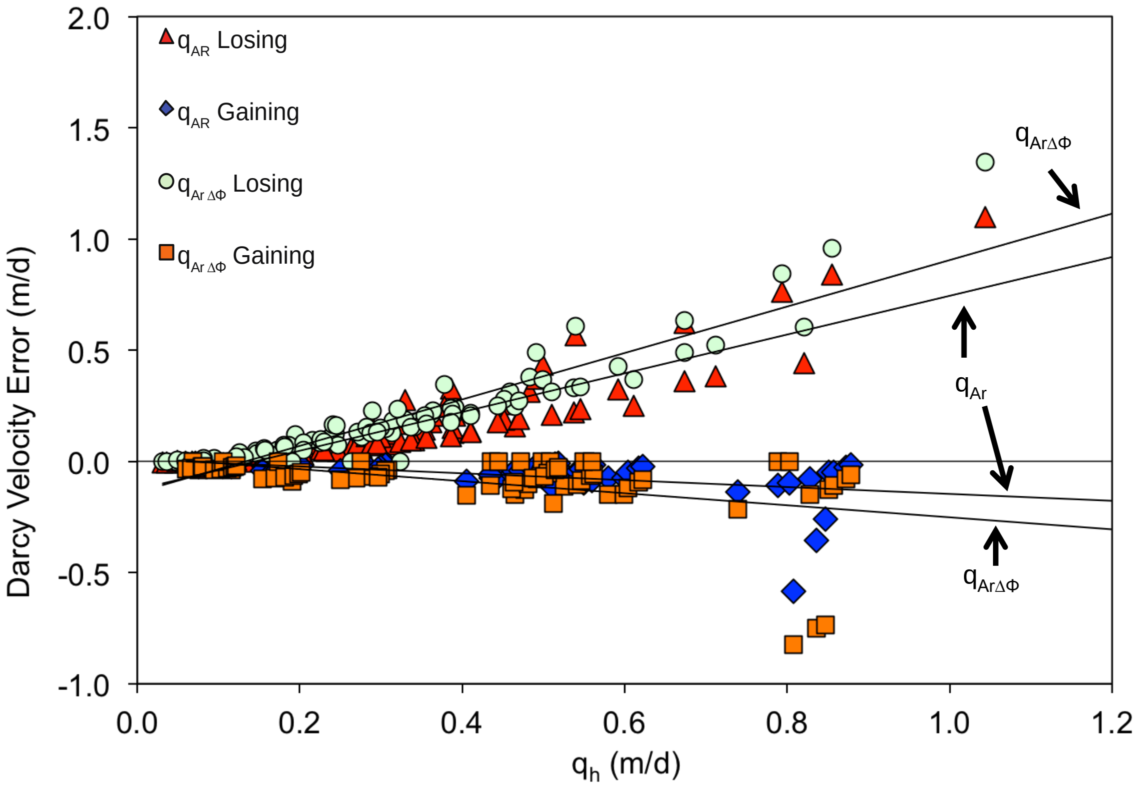

Figure 5: Performance of amplitude ratio, q_{AR} and combined amplitude ratio/phase shift, $q_{Ar\,\Delta\,\Phi}$, heat-as-a-tracer methods compared to horizontal Darcy velocity magnitude, q_h, for both gaining and losing flow geometries.

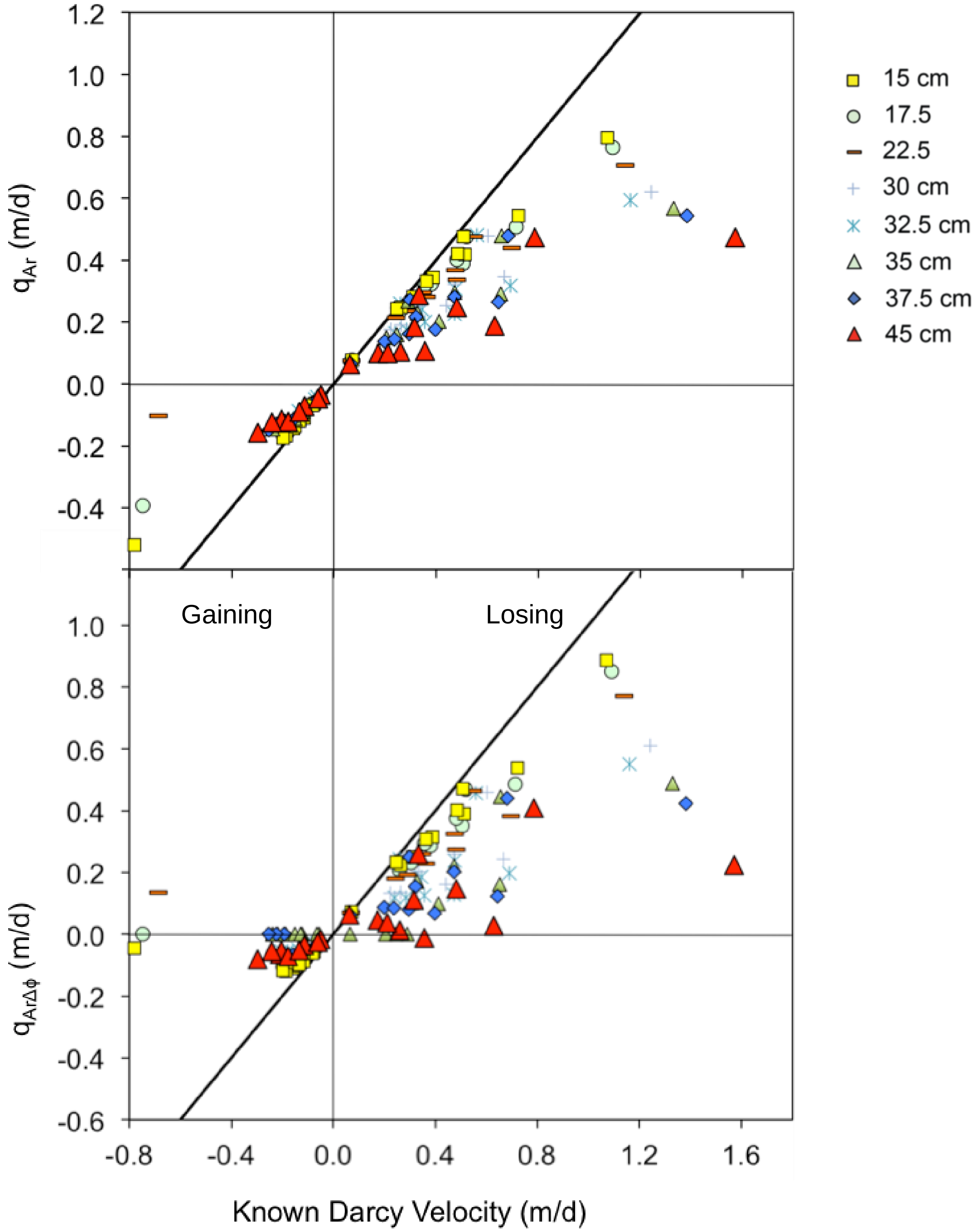

Figure 6: Known Darcy velocity compared to amplitude ratio derived flux (q_{Ar}) (top) and combined amplitude ratio and phase shift derived flux ($q_{Ar\Delta\phi}$)$_\phi$ (bottom) separated by center depth between temperature observation nodes. Black diagonal lines are the 1 to 1 lines. Temperature derived fluxes are calculated from temperature time series extracted at depths of 10, 20, 25, 40 and 50 cm.

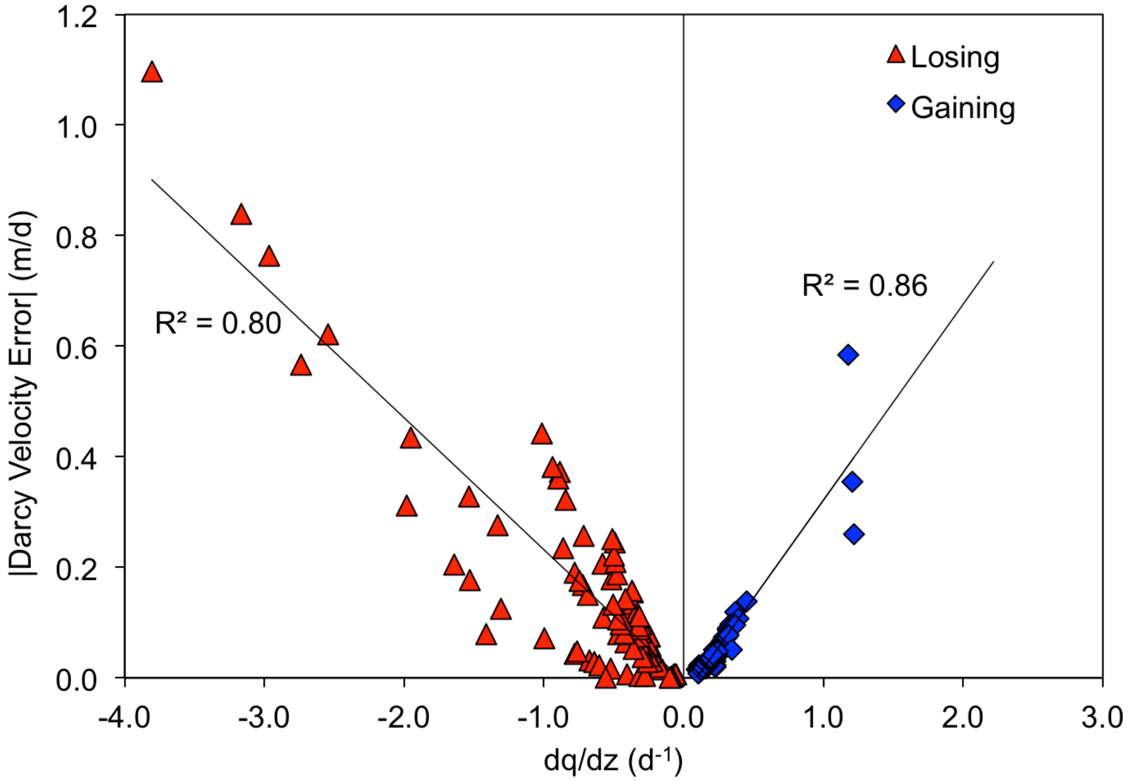

Figure 7: Error response for amplitude ratio derived fluxes as a function of degree of flow non-uniformity dq/dz for losing (red triangles) and gaining (blue diamonds) groundwater flows.

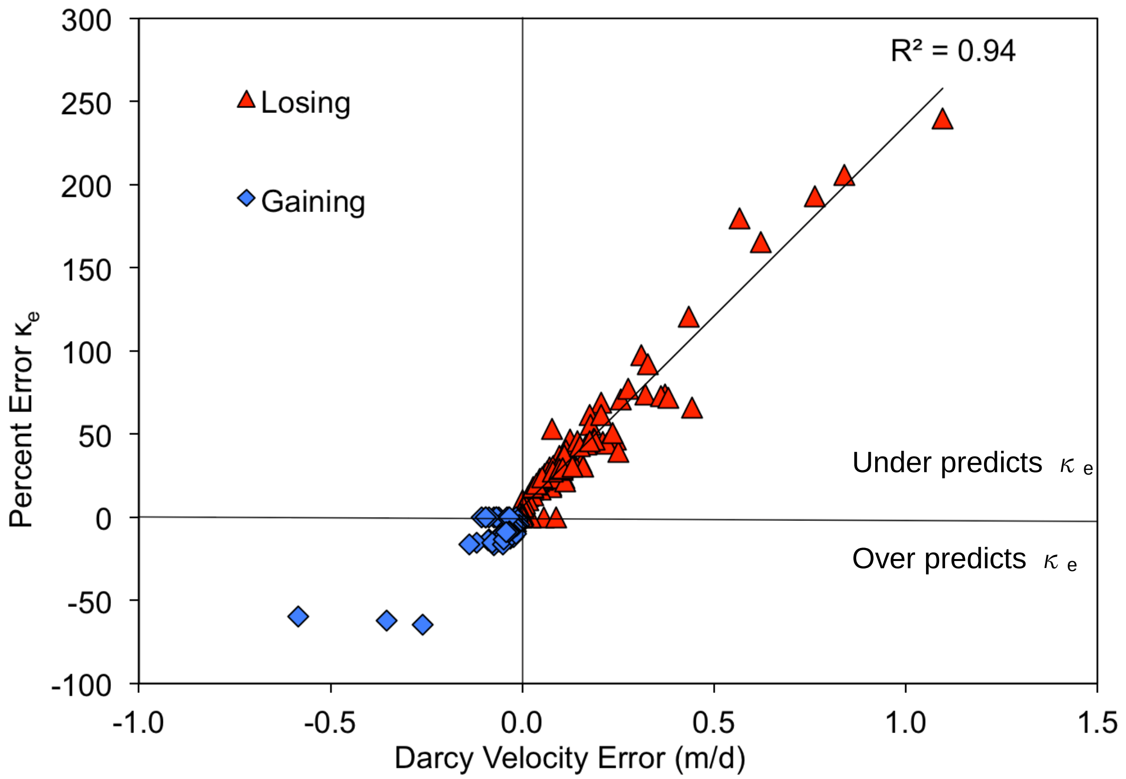

Figure 8: Percent error in temperature derived effective thermal diffusivity, κ_e, compared to amplitude ratio derived Darcy velocity error for gaining (blue diamond) and losing (red triangle) groundwater flow paths. Percent error κ_e is positive when temperature derived κ_e under predicts actual modeled . Negative values of Percent error κ_e indicate over predicted temperature derived κ_e.

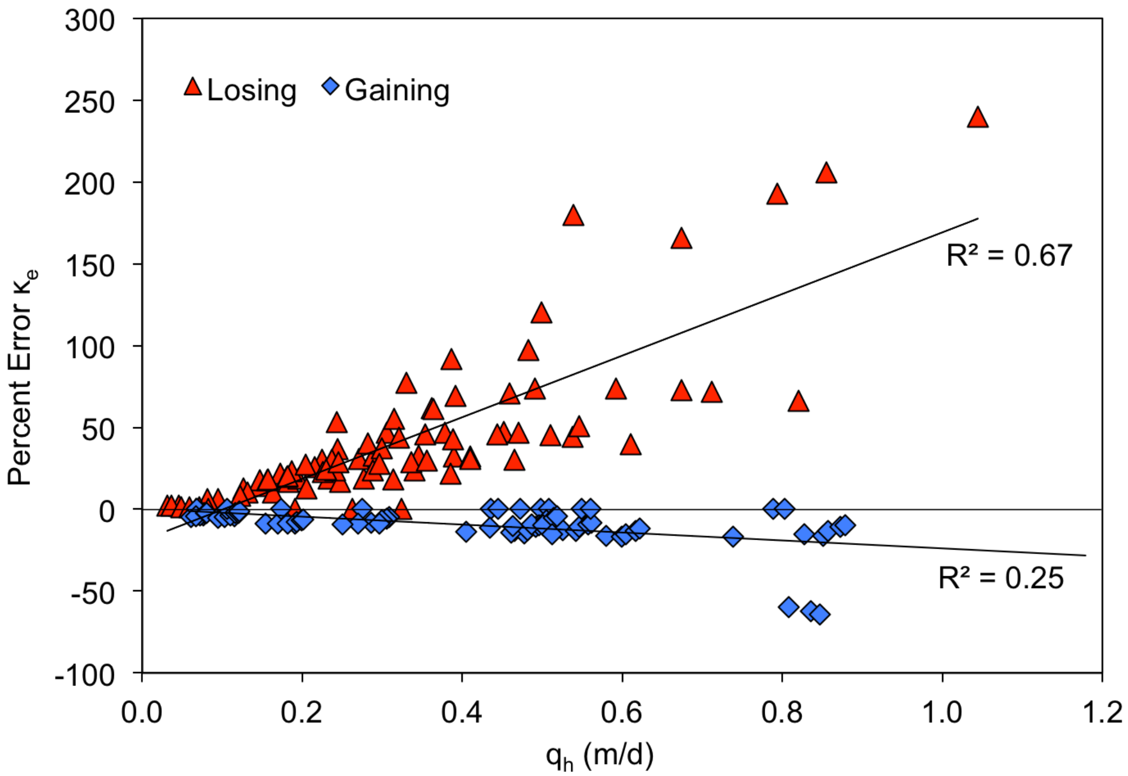

Figure 9: Percent error in temperature derived effective thermal diffusivity, κ_e, compared to horizontal Darcy flux magnitude for gaining (blue diamond) and losing (red triangle) groundwater flow paths.

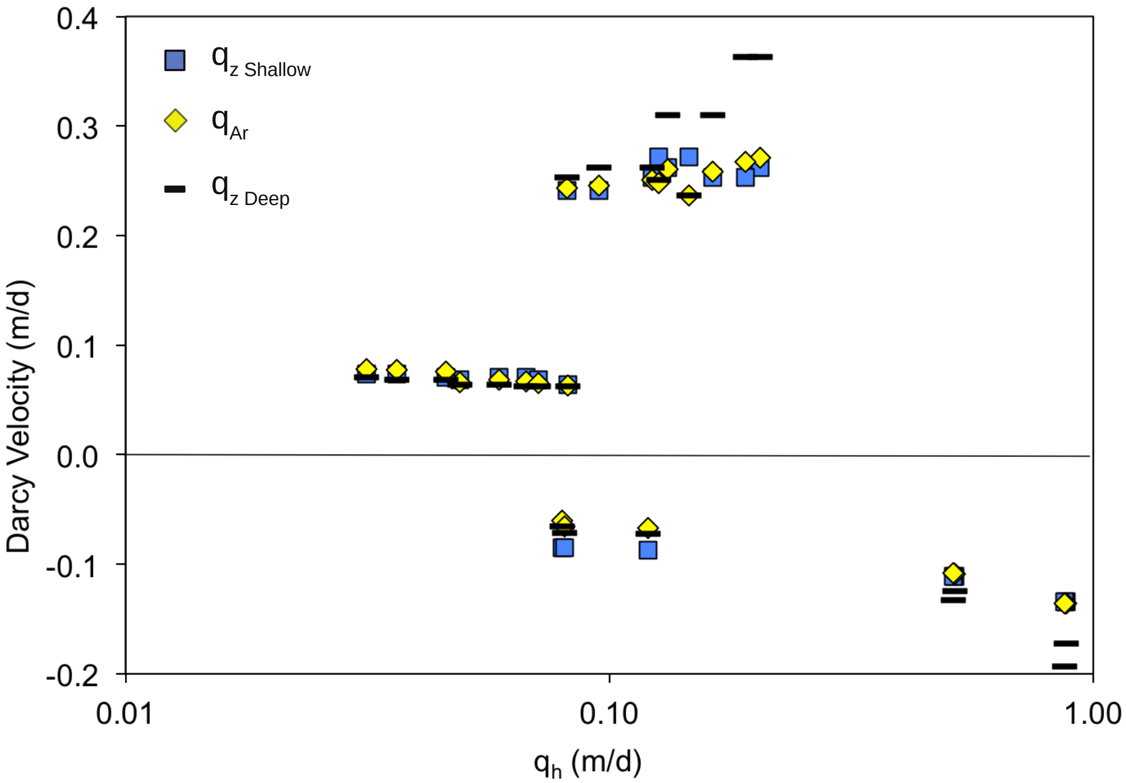

Figure 10: Range of horizontal velocities where the amplitude ratio derived flux (yellow diamonds) falls within the range of the actual modeled Darcy flux between the shallow (blue square) and deep (black line) observation nodes. Only ~7% of the 163 temperature derived velocities fall within the range of velocities occurring between the shallow and deep observation node. ~15% of the 163 flux calculations (pictured here) fall within 0.006 m/d of this range.

APPENDIX A

HYDRAULIC BOUNDARY CONDITIONS

Specified Darcy velocities at the X, Y and Z outlets for 11 losing (1) and 10 gaining (2) groundwater flow fields for all 21 simulations ordered by vertical Darcy velocity. A constant head boundary of 0.2 m was applied to the remaining three sides of the cube (X inlet, Y inlet, Z inlet). Flow enters the model from the top for losing simulations and enters from the bottom for gaining simulations. For gaining conditions, a constant head is applied to the bottom of the model and the outlet velocity boundary condition is applied to the top. For losing conditions, a constant head boundary is applied to the top of the model and an outlet velocity boundary is applied to the bottom.

Table A.1: Losing Groundwater flow fields

Trial	q_z (m/d)	q_x (m/d)	q_y (m/d)
1	0.06	0.45	0.5
2	0.1	0.8	0.6
3	0.1	1	0.1
4	0.1	0.1	0.1
5	0.1	0.1	0.5
6	0.2	1	0.8
7	1	1	1
8	1	0.1	1
9	1	0.1	0.1
10	2.6	0.01	0.01
11	5	0.2	0.2

Table A.2: Gaining Groundwater flow fields

Trial	q_z (m/d)	q_x (m/d)	q_y (m/d)
12	-0.1	0	0.1
13	-0.1	0.1	0.1
14	-0.1	0.1	1
15	-0.1	1	1
16	-0.15	0.5	0.7
17	-0.15	0.7	0.4
18	-0.2	0.2	0.1
19	-0.2	0.4	0.6
20	-0.2	0.7	0.6
21	-1	0.1	1

Note: The specified outlet fluxes are correlated to the velocity in the center of the model, but are not identical.

APPENDIX B

VERTICAL MESH ELEMENT LENGTH

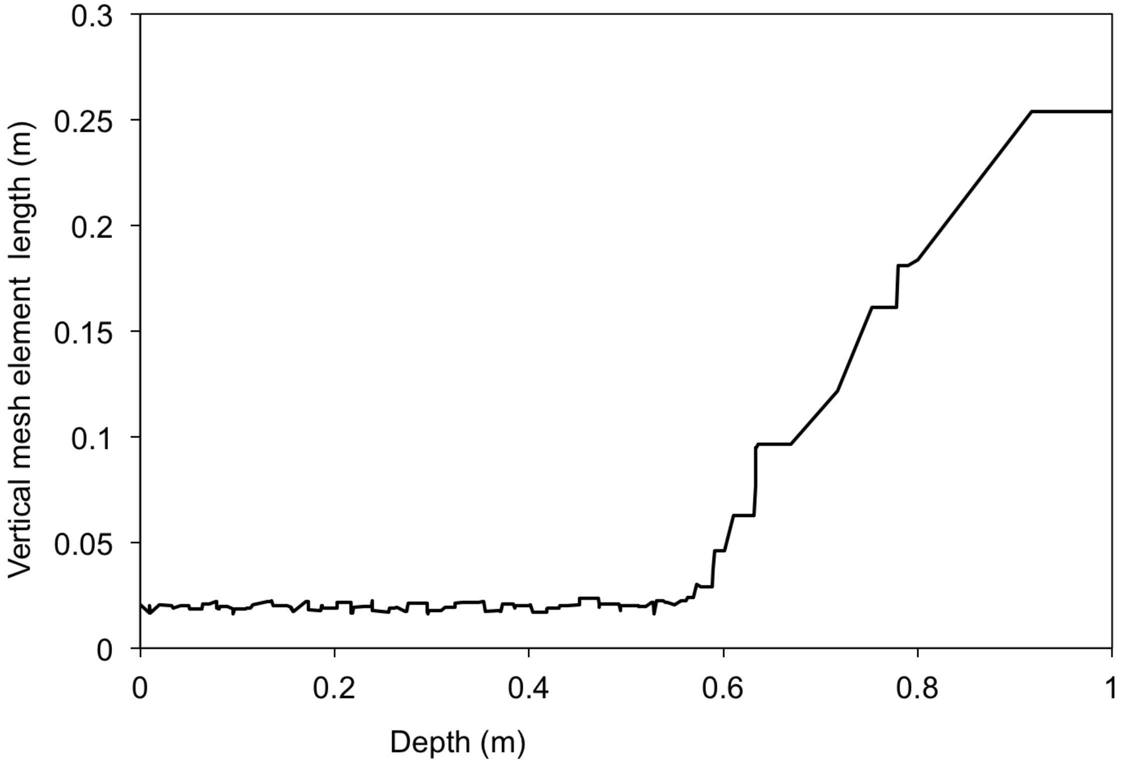

Figure B.1: Vertical mesh element length along the vertical centerline of the model. Depth of 0 m corresponds to the top of the model and 1 m corresponds to the bottom of the model.

APPENDIX C

SAMPLE MODEL OUTPUTS

The following cross-sections (Figure C.1) contain the same information as Figure 2, but occur in additional locations in the model.

Cross-sections parallel to X-axis:

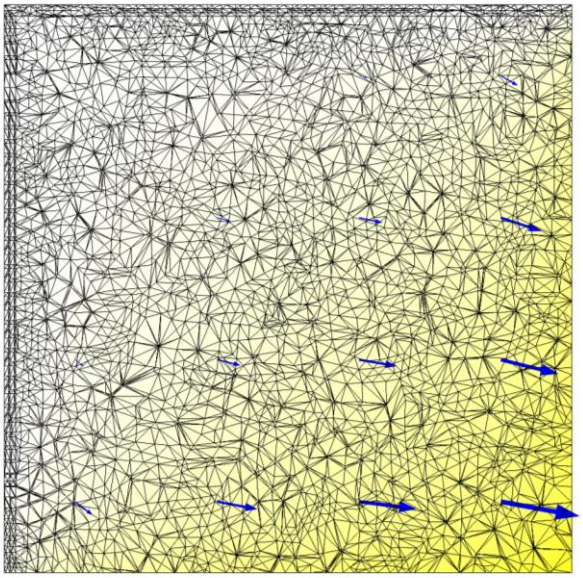

10 cm from X-inlet hydraulic head boundary

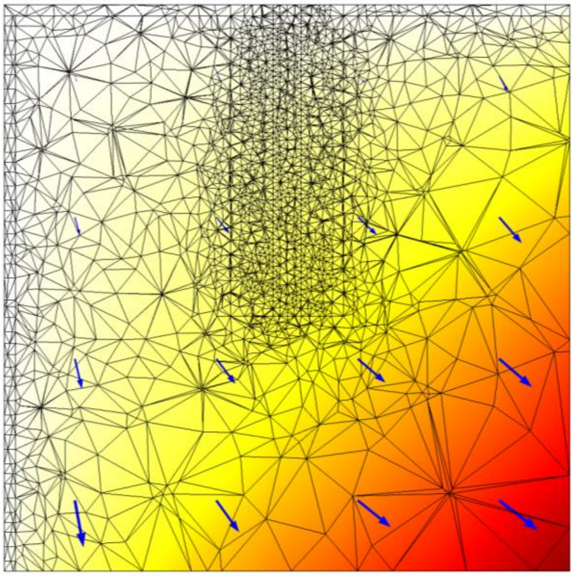

50 cm from X-inlet hydraulic head boundary

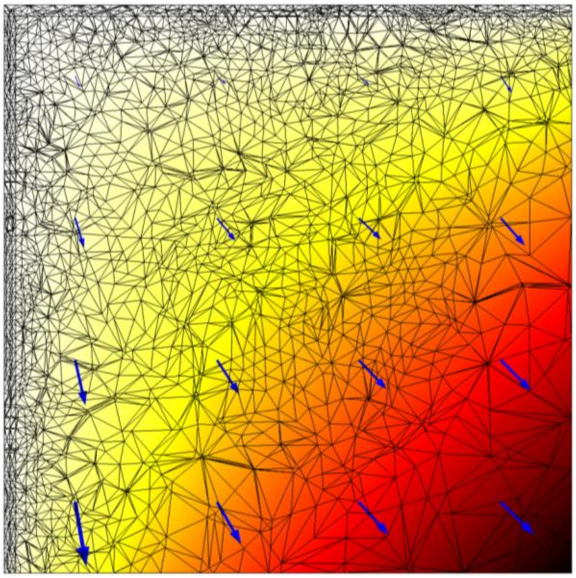

75 cm from X-inlet hydraulic head boundary

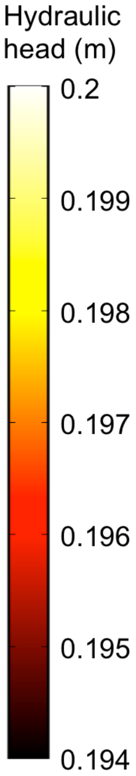

Cross-sections parallel to Y-axis:

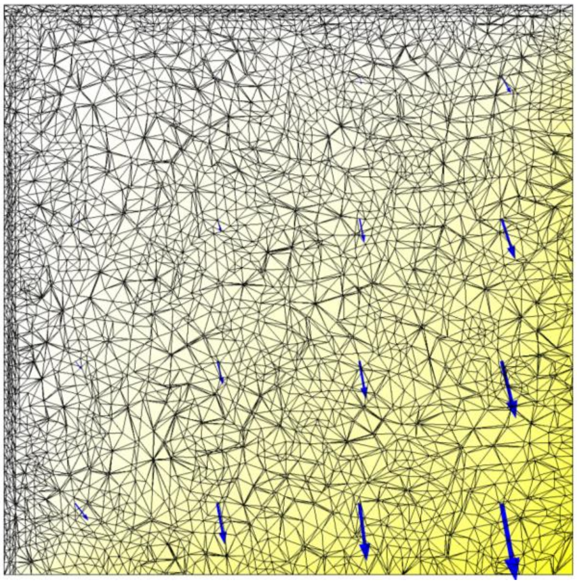

10 cm from Y-inlet hydraulic head boundary

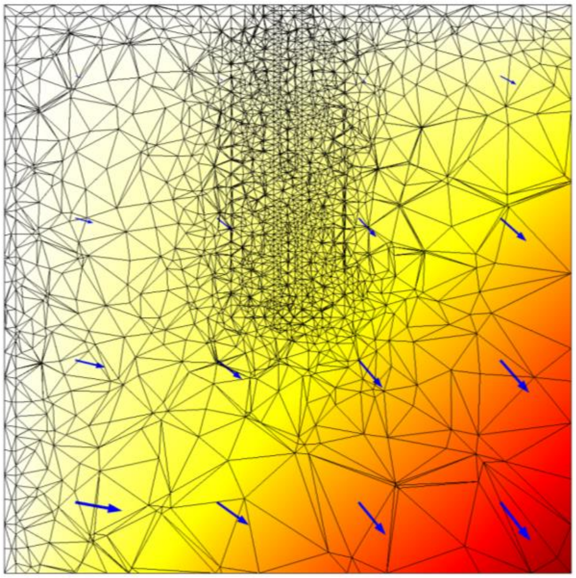

50 cm from Y-inlet hydraulic head boundary

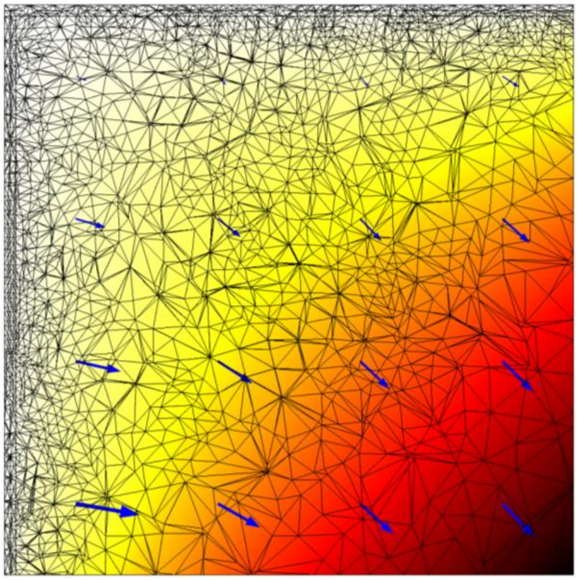

75 cm from Y-inlet hydraulic head boundary

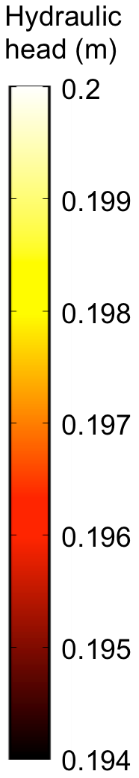

Cross-sections parallel to top of model:

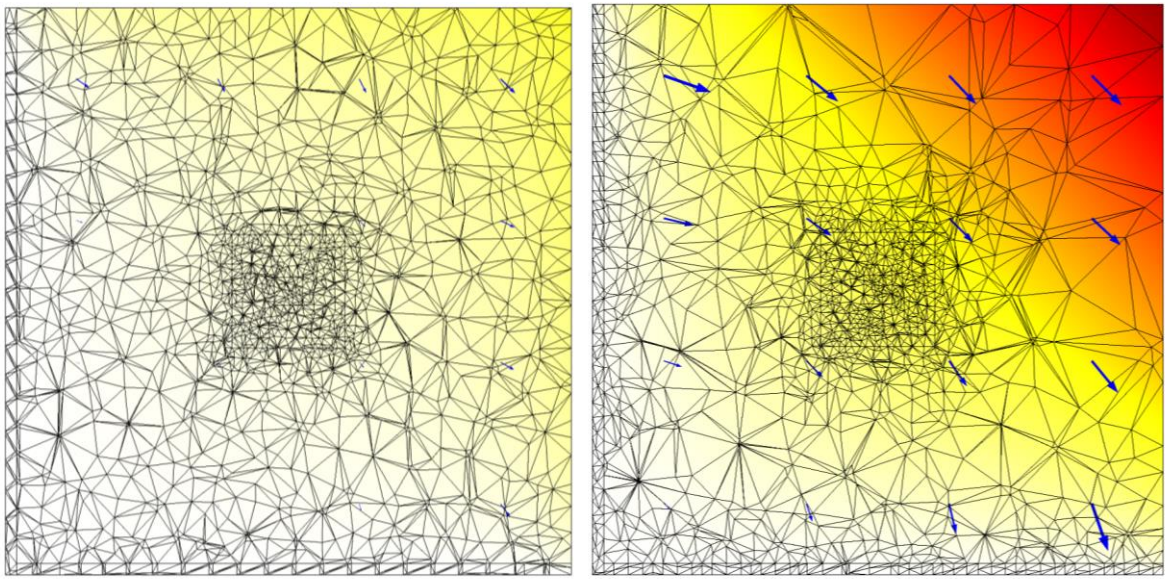

10 cm depth from top of model

50 cm depth from top of model

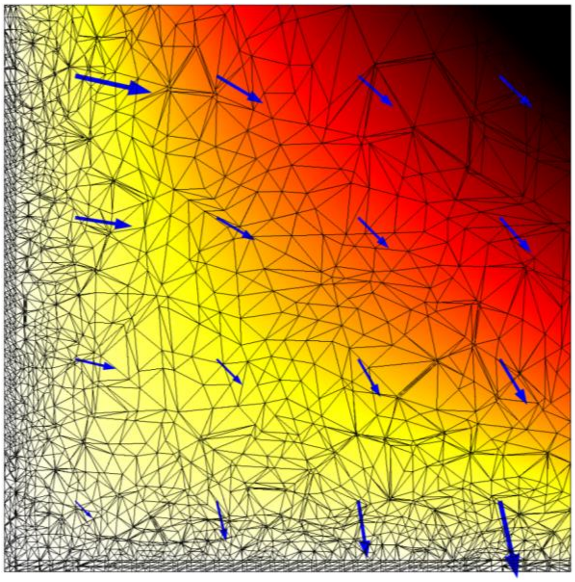

75 cm depth from top of model

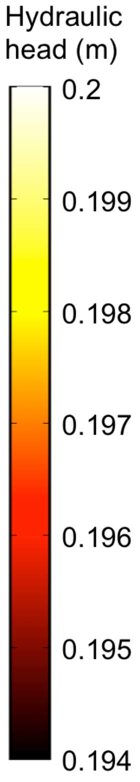

Figure C.1: Model cross sections showing hydraulic head (m), mesh discretization and flow direction for a sample trial. The color surface represents hydraulic head in meters and the blue arrows indicate flow direction for a sample model run (Trial 7, Appendix A). The black wireframe indicates mesh discretization and is constant across all models runs. All cross-sections are a 1 m by 1 m slice exported from the model.

Temperature time series were extracted for each model run. Figure C.2 shows temperature time series at depths of 10 cm (blue), 20 cm (red) and 50 (orange) cm as well as the diurnal temperature forcing at the surface (black) for a sample model run (Trial 7). Note that the modeled temperature time series and the surface temperature forcing do not line up within the first day of the model. The entire model is equal to T_0 of 19.85 at the time of 0 days. This period of time before the model equilibrated to steady state was ignored in our error analysis.

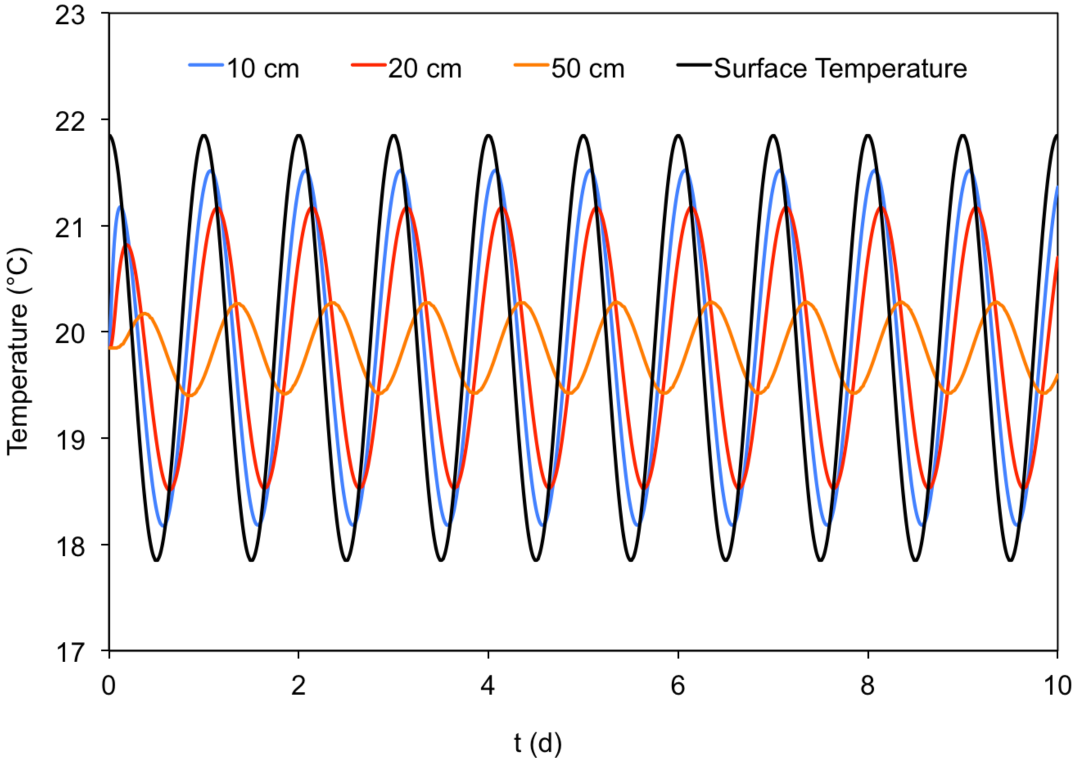

Figure C.2: Temperature time series at depths of 10 cm (blue), 20 cm (red) and 50 (orange) cm and the diurnal temperature forcing at the surface (black) for a sample model run (Trial 7).

Figure C.3 shows temperature time series with depth for the last day for the same sample model run (Trial 7). Note that the temperature envelope approaches the mean temperature of 19.85°C as depth increases due to the constant temperature boundary at the bottom of the model.

Since the constant temperature boundary is equivalent to the mean of the temperature forcing on the surface, no additional thermal gradient with depth is introduced into the system (Briggs 2014).

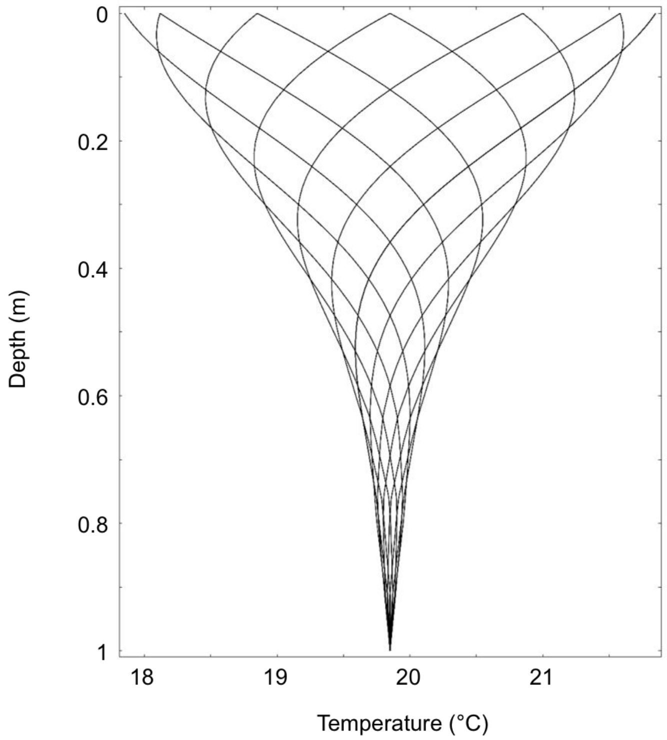

Figure C.3: Temperature time series with depth for the last day of a sample model run (Trial 7). Each black line represents the temperature with depth at a 2-hour time step.

APPENDIX D

COMPARISON OF MODEL TO 1D SOLUTION

In order to verify that the model was functioning properly, modeled temperature time series were compared to the 1D analytic equation (Equation 3) with the same boundary conditions and thermal parameters. For any model run, the largest downward flux occurring in the center column, where the temperature time series are extracted from, was 1.57 m/d (Figure 1). The largest downward flux occurring anywhere in the model was 5 m/d. Larger velocities result in greater chances of model instability and higher numerical error (Hans Johnston, personal communication). Thus, a maximum bound of error can be achieved anywhere within the center column by using a velocity greater than the largest fluxes occurring in any model run. For this comparison, a 1D vertical flow field with a downward Darcy velocity of 5 m/d was used. The maximum error occurring in the last day of the trial was 0.0028°C. Thus, we set out maximum error with the 1D analytic solution to 0.003°C as a conservative estimate.

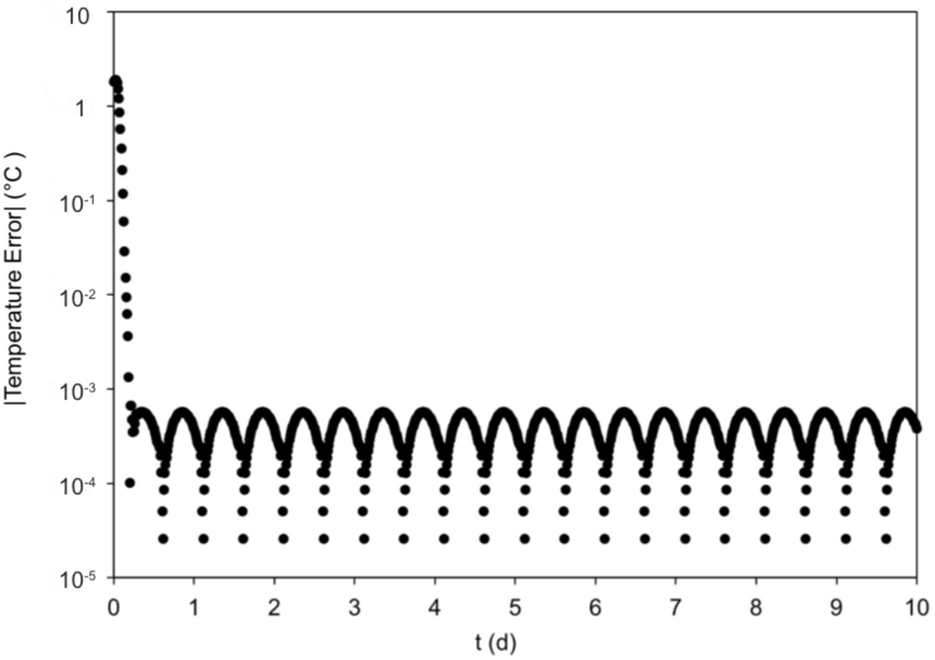

Figure D.1: Comparison of model to 1D analytical solution for a 5 m/d downward vertical flow field.

APPENDIX E

TEMPERATURE EFFECTS ON HYDRAULIC CONDUCTIVITY

We ignored temperature impacts on hydraulic conductivity (K). Temperature changes the density and viscosity (μ) of water, resulting in changes in hydraulic conductivity. Temperature variations within the model were less than 4°C at any given point and variations in hydraulic conductivity are less than 5%.

A 5% change in K will result in a 5% change in Darcy velocity. We can neglect these effects since the maximum and minimum temperatures occurring at the surface will not propagate deep into the subsurface. Especially in the case of gaining conditions, the amplitude of the diurnal signal will be greatly diminished within the first 10 cm of the model. Thus, the actual range of temperatures occurring in the model is much smaller than 2°C, and temperature will have a lesser effect on K.

Table E.1: Parameters used for temperature effects on hydraulic conductivity analysis

Parameter	Minimum	Average	Maximum
T (°C)	17.85	19.85	21.85
Viscosity ($\frac{kg}{s*m}$)	1.06E-03	1.01E-03	9.58E-04
Density water (kg/m^3)	998.2	998.0	997.8
K input in model (m/d)	240	240	240
Permeability (m^2) $= \frac{K\,\mu}{\rho\ \mathrm{g}}$	2.85E-10	2.85E-10	2.85E-10
K with temperature effects (m/d) $= \frac{k\rho \mathrm{g}}{\mu}$	228.5	240	251.7
Change in K (%)	4.80	0	4.91

Note: k is permeability (m^2) and g is gravity (9.81 m/s^2).

APPENDIX F

THERMAL PECLET NUMBER ANALYSIS

The thermal Peclet number can be defined as (Rau 2010):

$$Peclet\ number = \frac{\rho_{w} c_{w} q L}{\lambda_{0}} \tag{14}$$

where L is the characteristic length, in this case the mean grain size. We used a mean grain size of 3 mm. Increasing Darcy flux is directly correlated with larger Peclet numbers. Thus, the maximum and minimum Peclet number for our system can be estimated using the maximum and minimum Darcy velocities. The range of vertical Darcy velocities occurring in the center column was 0.05 to 1.57 m/d. The largest velocity occurring anywhere in the model for any model run was 5 m/d. In any case, the Peclet number was less than 0.5 and dispersivity can be ignored (Rau et al. 2010).

Table F.1: Thermal Peclet numbers for the range of Darcy velocities used in all model runs.

Darcy Flux (m/d)	Peclet number
0.05	0.0025
1.57	0.08
5	0.25

APPENDIX G

SUMMARY TABLES OF RESULTS

Summary tables of Darcy velocity magnitudes and error analysis for temperature derived flux and effective thermal diffusivity separated by center of sensor depth for all 21 flow fields, ordered by Trial Number. Dashed lines indicate a non-real number prediction for effective thermal diffusivity and thus non-numeric κ_e error.

Table G.1: 15 cm Depth, 10 cm Spacing between Temperature Observation Nodes

Trial	q_z (m/d)	q_x (m/d)	q_y (m/d)	q_h (m/d)	dq/dz (d^{-1})	q_{AR} (m/d)	$q_{Ar\Delta\Phi}$ (m/d)	q_{AR} Error (m/d)	κ_e Error (%)
1	0.26	0.09	0.09	0.13	-0.15	0.25	0.22	0.02	12.9
2	0.39	0.12	0.14	0.19	-0.23	0.34	0.32	0.05	23.2
3	0.31	0.07	0.14	0.16	-0.22	0.28	0.25	0.03	17.8
4	0.07	0.02	0.02	0.03	-0.05	0.08	0.07	-0.01	2.4
5	0.36	0.11	0.11	0.16	-0.26	0.33	0.31	0.03	18.0
6	0.51	0.16	0.18	0.24	-0.31	0.42	0.39	0.10	36.7
7	0.72	0.22	0.22	0.31	-0.52	0.54	0.54	0.18	55.5
8	0.48	0.18	0.10	0.20	-0.42	0.42	0.40	0.06	27.5
9	0.25	0.06	0.06	0.08	-0.28	0.24	0.23	0.00	6.2
10	0.51	0.10	0.10	0.15	-0.67	0.48	0.47	0.03	17.8
11	1.07	0.23	0.23	0.33	-1.33	0.79	0.89	0.28	77.4
12	-0.08	0.05	0.07	0.08	0.12	-0.07	-0.06	-0.01	-2.5
13	-0.08	0.09	0.09	0.12	0.10	-0.07	-0.06	-0.01	-1.5
14	-0.12	0.26	0.45	0.52	0.11	-0.11	-0.09	-0.01	-4.5
15	-0.15	0.62	0.62	0.88	0.16	-0.14	-0.09	-0.02	-9.7
16	-0.16	0.38	0.42	0.56	0.14	-0.14	-0.10	-0.02	-8.3
17	-0.13	0.23	0.21	0.31	0.13	-0.12	-0.10	-0.01	-5.0
18	-0.16	0.15	0.13	0.20	0.23	-0.14	-0.11	-0.02	-6.3
19	-0.19	0.33	0.37	0.50	0.17	-0.17	-0.12	-0.02	-9.9
20	-0.20	0.45	0.43	0.62	0.17	-0.18	-0.12	-0.02	-12.0
21	-0.78	0.50	0.69	0.85	1.22	-0.52	-0.05	-0.26	-64.5

Notes: dq/dz is calculated from Darcy velocity magnitudes at 10 and 20 cm depth. q_{AR} and percent error κ_e are calculated from temperature time series extracted at 10 and 20 cm depth.

Table G.2: 17.5 cm Depth, 15 cm Spacing between Temperature Observation Nodes

Trial	q_z (m/d)	q_x (m/d)	q_y (m/d)	q_h (m/d)	dq/dz (d^{-1})	q_{AR} (m/d)	$q_{Ar\Delta\Phi}$ (m/d)	q_{AR} Error (m/d)	κ_e Error (%)
1	0.26	0.11	0.10	0.15	-0.17	0.24	0.21	0.02	14.3
2	0.38	0.14	0.16	0.22	-0.25	0.32	0.29	0.06	25.9
3	0.30	0.08	0.16	0.18	-0.25	0.27	0.23	0.04	19.7
4	0.07	0.03	0.03	0.04	-0.06	0.08	0.07	-0.01	2.4
5	0.36	0.13	0.13	0.18	-0.29	0.32	0.29	0.04	20.1
6	0.50	0.19	0.21	0.28	-0.34	0.39	0.35	0.11	40.1
7	0.71	0.26	0.26	0.36	-0.58	0.51	0.49	0.21	61.3
8	0.48	0.20	0.12	0.24	-0.47	0.40	0.38	0.08	30.4
9	0.25	0.07	0.07	0.10	-0.32	0.25	0.23	0.00	6.2
10	0.52	0.12	0.12	0.17	-0.78	0.48	0.47	0.04	21.8
11	1.09	0.27	0.27	0.39	-1.54	0.76	0.85	0.33	91.9
12	-0.07	0.05	0.07	0.08	0.12	-0.06	-0.05	-0.01	-2.5
13	-0.08	0.09	0.09	0.12	0.11	-0.07	-0.06	-0.01	-2.5
14	-0.12	0.26	0.45	0.51	0.12	-0.11	-0.08	-0.01	-5.4
15	-0.16	0.62	0.62	0.87	0.19	-0.14	-0.09	-0.03	-10.9
16	-0.16	0.37	0.41	0.56	0.16	-0.14	-0.10	-0.02	-9.2
17	-0.13	0.23	0.21	0.31	0.14	-0.11	-0.09	-0.02	-5.6
18	-0.15	0.15	0.13	0.20	0.23	-0.13	-0.10	-0.02	-6.8
19	-0.19	0.33	0.37	0.49	0.19	-0.16	-0.11	-0.03	-10.9
20	-0.20	0.45	0.43	0.62	0.20	-0.17	-0.10	-0.03	-13.1
21	-0.75	0.49	0.68	0.84	1.20	-0.39	0.00	-0.35	-62.3

Notes: dq/dz is calculated from Darcy velocity magnitudes at 10 and 25 cm depth. q_{AR} and percent error κ_e are calculated from temperature time series extracted at 10 and 25 cm depth.

Table G.3: 22.5 cm Depth, 5 cm Spacing between Temperature Observation Nodes

Trial	q_z (m/d)	q_x (m/d)	q_y (m/d)	q_h (m/d)	dq/dz (d^{-1})	q_{AR} (m/d)	$q_{Ar\Delta\Phi}$ (m/d)	q_{AR} Error (m/d)	κ_e Error (%)
1	0.24	0.13	0.13	0.18	-0.21	0.21	0.18	0.03	16.9
2	0.36	0.18	0.20	0.27	-0.31	0.28	0.23	0.08	30.9
3	0.29	0.10	0.20	0.23	-0.29	0.24	0.19	0.05	22.6
4	0.07	0.03	0.03	0.05	-0.07	0.08	0.07	-0.01	2.4
5	0.35	0.16	0.16	0.23	-0.36	0.30	0.26	0.05	24.1
6	0.48	0.24	0.26	0.35	-0.42	0.34	0.28	0.14	45.7
7	0.70	0.33	0.33	0.46	-0.71	0.44	0.38	0.26	70.9
8	0.48	0.26	0.16	0.30	-0.58	0.37	0.33	0.11	37.1
9	0.26	0.09	0.09	0.12	-0.40	0.25	0.24	0.01	8.2
10	0.55	0.16	0.16	0.23	-1.00	0.48	0.46	0.07	30.2
11	1.14	0.35	0.35	0.50	-1.95	0.71	0.77	0.43	120.5
12	-0.07	0.04	0.06	0.08	0.12	-0.05	-0.04	-0.02	-2.5
13	-0.07	0.08	0.08	0.12	0.11	-0.06	-0.05	-0.01	-2.5
14	-0.13	0.25	0.44	0.51	0.16	-0.11	-0.07	-0.02	-7.0
15	-0.18	0.61	0.61	0.86	0.25	-0.13	-0.07	-0.05	-13.2
16	-0.17	0.36	0.41	0.55	0.20	-0.13	-0.08	-0.03	-11.0
17	-0.13	0.22	0.20	0.30	0.16	-0.10	-0.07	-0.03	-6.8
18	-0.14	0.15	0.13	0.19	0.23	-0.11	-0.08	-0.03	-7.9
19	-0.19	0.32	0.36	0.48	0.22	-0.14	-0.08	-0.04	-12.8
20	-0.20	0.44	0.42	0.60	0.24	-0.15	-0.08	-0.05	-15.2
21	-0.69	0.47	0.66	0.81	1.18	-0.10	0.13	-0.59	-59.9

Notes: dq/dz is calculated from Darcy velocity magnitudes at 20 and 25 cm depth. q_{AR} and percent error κ_e are calculated from temperature time series extracted at 20 and 25 cm depth.

Table G.4: 30 cm Depth, 20 cm Spacing between Temperature Observation Nodes

Trial	q_z (m/d)	q_x (m/d)	q_y (m/d)	q_h (m/d)	dq/dz (d^{-1})	q_{AR} (m/d)	$q_{Ar\Delta\Phi}$ (m/d)	q_{AR} Error (m/d)	κ_e Error (%)
1	0.22	0.17	0.16	0.23	-0.23	0.18	0.13	0.05	18.5
2	0.33	0.23	0.26	0.35	-0.35	0.22	0.15	0.11	32.7
3	0.26	0.13	0.26	0.29	-0.32	0.19	0.14	0.07	23.6
4	0.07	0.04	0.04	0.06	-0.08	0.07	0.06	0.00	1.4
5	0.33	0.21	0.21	0.30	-0.42	0.25	0.20	0.08	27.6
6	0.44	0.31	0.33	0.45	-0.47	0.25	0.16	0.19	47.0
7	0.67	0.42	0.42	0.59	-0.84	0.35	0.24	0.32	73.8
8	0.47	0.33	0.20	0.39	-0.69	0.32	0.26	0.15	42.9
9	0.28	0.12	0.12	0.16	-0.52	0.26	0.24	0.02	10.1
10	0.60	0.22	0.22	0.31	-1.31	0.48	0.46	0.13	46.8
11	1.24	0.48	0.48	0.67	-2.54	0.62	0.61	0.62	165.7
12	-0.06	0.04	0.06	0.07	0.11	-0.05	-0.03	-0.02	-3.6
13	-0.07	0.08	0.08	0.11	0.11	-0.05	-0.04	-0.02	-3.8
14	-0.14	0.24	0.42	0.49	0.20	-0.11	-0.07	-0.03	-9.1
15	-0.22	0.59	0.59	0.83	0.32	-0.14	-0.07	-0.08	-15.5
16	-0.18	0.35	0.39	0.53	0.25	-0.12	-0.07	-0.05	-12.8
17	-0.13	0.21	0.19	0.29	0.18	-0.10	-0.06	-0.03	-8.1
18	-0.13	0.14	0.12	0.18	0.22	-0.09	-0.06	-0.04	-8.7
19	-0.19	0.30	0.35	0.46	0.26	-0.13	-0.06	-0.06	-14.2
20	-0.21	0.42	0.40	0.58	0.29	-0.14	-0.06	-0.08	-16.5
21	-0.61	0.62	0.61	0.87	-1.11	0.01	0.13	-0.62	38.1

Notes: dq/dz is calculated from Darcy velocity magnitudes at 20 and 40 cm depth. q_{AR} and percent error κ_e are calculated from temperature time series extracted at 20 and 40 cm depth. VFLUX predicted the wrong direction of flux for Trial 21.

Table G.5: 32.5 cm Depth, 15 cm Spacing between Temperature Observation Nodes

Trial	q_z (m/d)	q_x (m/d)	q_y (m/d)	q_h (m/d)	dq/dz (d^{-1})	q_{AR} (m/d)	$q_{Ar\Delta\Phi}$ (m/d)	q_{AR} Error (m/d)	κ_e Error (%)
1	0.24	0.14	0.13	0.20	-0.24	0.16	0.12	0.08	19.0
2	0.36	0.19	0.22	0.29	-0.36	0.20	0.13	0.15	33.0
3	0.28	0.11	0.22	0.24	-0.33	0.17	0.12	0.11	23.6
4	0.07	0.04	0.04	0.05	-0.09	0.07	0.06	0.00	1.4
5	0.35	0.17	0.17	0.25	-0.44	0.24	0.18	0.11	28.6
6	0.47	0.25	0.28	0.38	-0.49	0.23	0.13	0.24	46.8
7	0.69	0.35	0.35	0.49	-0.89	0.32	0.20	0.37	73.8
8	0.48	0.27	0.17	0.32	-0.72	0.31	0.24	0.17	43.9
9	0.26	0.09	0.09	0.13	-0.56	0.26	0.24	0.00	10.1
10	0.56	0.17	0.17	0.24	-1.41	0.48	0.46	0.08	53.0
11	1.16	0.38	0.38	0.54	-2.74	0.59	0.55	0.57	179.9
12	-0.07	0.04	0.06	0.08	0.11	-0.04	-0.03	-0.02	-3.9
13	-0.07	0.08	0.08	0.12	0.11	-0.05	-0.03	-0.02	-4.1
14	-0.13	0.25	0.44	0.50	0.22	-0.11	-0.07	-0.02	-9.9
15	-0.19	0.60	0.60	0.85	0.35	-0.14	-0.06	-0.05	-16.3
16	-0.17	0.36	0.40	0.54	0.26	-0.12	-0.06	-0.05	-13.4
17	-0.13	0.22	0.20	0.30	0.19	-0.09	-0.06	-0.03	-8.6
18	-0.14	0.14	0.12	0.19	0.22	-0.09	-0.05	-0.05	-8.9
19	-0.19	0.32	0.36	0.48	0.27	-0.12	-0.06	-0.06	-14.6
20	-0.20	0.43	0.41	0.60	0.31	-0.13	-0.05	-0.07	-16.9
21	-0.67	0.65	0.67	0.93	-1.09	0.05	0.13	-0.72	26.8

Notes: dq/dz is calculated from Darcy velocity magnitudes at 25 and 40 cm depth. q_{AR} and percent error κ_e are calculated from temperature time series extracted at 25 and 40 cm depth. VFLUX predicted the wrong direction of flux for Trial 21.

Table G.6: 35 cm Depth, 30 cm Spacing between Temperature Observation Nodes

Trial	q_z (m/d)	q_x (m/d)	q_y (m/d)	q_h (m/d)	dq/dz (d^{-1})	q_{AR} (m/d)	$q_{Ar\Delta\Phi}$ (m/d)	q_{AR} Error (m/d)	κ_e Error (%)
1	0.21	0.19	0.18	0.26	-0.24	0.15	NaN	0.06	-
2	0.31	0.26	0.29	0.39	-0.36	0.18	0.10	0.13	32.3
3	0.25	0.15	0.29	0.32	-0.32	0.16	NaN	0.09	-
4	0.07	0.05	0.05	0.07	-0.09	0.07	NaN	0.00	-
5	0.33	0.24	0.24	0.34	-0.45	0.23	0.17	0.10	28.8
6	0.41	0.35	0.38	0.51	-0.49	0.20	0.10	0.21	45.2
7	0.65	0.48	0.48	0.67	-0.90	0.29	0.16	0.36	72.9
8	0.47	0.38	0.24	0.44	-0.75	0.30	0.22	0.18	45.8
9	0.29	0.14	0.14	0.19	-0.60	0.27	NaN	0.02	-
10	0.65	0.26	0.26	0.36	-1.53	0.48	0.45	0.18	61.7
11	1.33	0.56	0.56	0.79	-2.96	0.57	0.49	0.76	193.0
12	-0.06	0.04	0.06	0.07	0.11	-0.04	NaN	-0.01	-
13	-0.07	0.08	0.08	0.11	0.11	-0.05	NaN	-0.02	-
14	-0.15	0.23	0.41	0.47	0.23	-0.11	NaN	-0.04	-
15	-0.24	0.57	0.57	0.80	0.37	-0.15	NaN	-0.10	-
16	-0.19	0.34	0.38	0.51	0.27	-0.12	NaN	-0.06	-
17	-0.13	0.20	0.18	0.28	0.19	-0.10	NaN	-0.03	-
18	-0.12	0.13	0.11	0.17	0.21	-0.09	NaN	-0.04	-
19	-0.19	0.29	0.33	0.45	0.28	-0.12	NaN	-0.07	-
20	-0.22	0.41	0.39	0.56	0.32	-0.13	NaN	-0.09	-
21	-0.57	0.59	0.57	0.82	-1.06	0.01	0.10	-0.58	25.8

Notes: dq/dz is calculated from Darcy velocity magnitudes at 20 and 50 cm depth. q_{AR} and percent error κ_e are calculated from temperature time series extracted at 20 and 50 cm depth. VFLUX predicted the wrong direction of flux for Trial 21.

Table G.7: 37.5 cm Depth, 25 cm Spacing Between Temperature Observation Nodes

Trial	q_z (m/d)	q_x (m/d)	q_y (m/d)	q_h (m/d)	dq/dz (d^{-1})	q_{AR} (m/d)	$q_{Ar\Delta\Phi}$ (m/d)	q_{AR} Error (m/d)	κ_e Error (%)
1	0.20	0.20	0.19	0.28	-0.24	0.14	0.09	0.06	18.7
2	0.30	0.27	0.31	0.41	-0.37	0.16	0.08	0.13	32.2
3	0.24	0.16	0.30	0.34	-0.33	0.14	0.08	0.09	23.6
4	0.06	0.05	0.05	0.07	-0.09	0.07	0.06	0.00	1.4
5	0.32	0.25	0.25	0.36	-0.47	0.22	0.15	0.11	29.6
6	0.40	0.36	0.40	0.54	-0.50	0.18	0.07	0.22	44.3
7	0.65	0.50	0.50	0.71	-0.94	0.26	0.12	0.38	71.9
8	0.47	0.40	0.25	0.47	-0.78	0.28	0.20	0.19	46.8
9	0.30	0.15	0.15	0.21	-0.64	0.27	0.25	0.03	13.0
10	0.68	0.28	0.28	0.39	-1.64	0.48	0.44	0.21	69.1
11	1.38	0.60	0.60	0.86	-3.17	0.54	0.42	0.84	205.9
12	-0.05	0.04	0.06	0.07	0.10	-0.04	-0.02	-0.01	-4.3
13	-0.07	0.07	0.07	0.10	0.11	-0.05	-0.03	-0.02	-4.6
14	-0.16	0.23	0.41	0.46	0.25	-0.11	-0.07	-0.05	-10.5
15	-0.15	0.56	0.56	0.79	0.39	-0.15	NaN	-0.11	-
16	-0.19	0.33	0.37	0.50	0.29	-0.12	NaN	-0.07	-
17	-0.13	0.20	0.18	0.27	0.20	-0.09	-0.06	-0.04	-8.8
18	-0.12	0.13	0.11	0.17	0.21	-0.08	-0.04	-0.04	-8.9
19	-0.19	0.29	0.33	0.44	0.29	-0.12	NaN	-0.07	-
20	-0.22	0.40	0.38	0.55	0.33	-0.13	NaN	-0.10	-
21	-0.56	0.58	0.56	0.80	-1.04	0.03	0.08	-0.59	14.1

Notes: dq/dz is calculated from Darcy velocity magnitudes at 25 and 50 cm depth. q_{AR} and percent error κ_e are calculated from temperature time series extracted at 25 and 50 cm depth. VFLUX predicted the wrong direction of flux for Trial 21.

Table G.8: 45 cm Depth, 5 cm Spacing between Temperature Observation Nodes

Trial	q_z (m/d)	q_x (m/d)	q_y (m/d)	q_h (m/d)	dq/dz (d^{-1})	q_{AR} (m/d)	$q_{Ar\Delta\Phi}$ (m/d)	q_{AR} Error (m/d)	κ_e Error (%)
1	0.17	0.23	0.22	0.31	-0.25	0.10	0.05	0.08	18.1
2	0.26	0.31	0.35	0.47	-0.37	0.10	0.01	0.16	30.3
3	0.21	0.18	0.34	0.39	-0.32	0.10	0.04	0.11	21.7
4	0.06	0.06	0.06	0.08	-0.10	0.06	0.06	0.00	0.4
5	0.32	0.29	0.29	0.41	-0.51	0.18	0.11	0.13	30.6
6	0.36	0.41	0.45	0.61	-0.51	0.11	-0.01	0.25	39.5
7	0.63	0.58	0.58	0.82	-1.01	0.19	0.03	0.44	66.1
8	0.48	0.46	0.30	0.55	-0.86	0.25	0.15	0.24	50.6
9	0.33	0.18	0.18	0.25	-0.76	0.29	0.26	0.05	16.8
10	0.79	0.34	0.34	0.48	-1.98	0.47	0.41	0.31	97.4
11	1.57	0.74	0.74	1.04	-3.81	0.47	0.22	1.10	239.8
12	-0.05	0.03	0.05	0.06	0.10	-0.04	-0.02	-0.01	-4.9
13	-0.06	0.07	0.07	0.10	0.11	-0.05	-0.03	-0.02	-5.2
14	-0.18	0.21	0.38	0.44	0.28	-0.12	-0.07	-0.06	-11.4
15	-0.30	0.52	0.52	0.74	0.45	-0.16	-0.08	-0.14	-16.6
16	-0.21	0.31	0.35	0.47	0.32	-0.13	-0.06	-0.09	-13.5
17	-0.13	0.19	0.17	0.25	0.21	-0.09	-0.05	-0.04	-9.1
18	-0.11	0.12	0.10	0.16	0.20	-0.07	-0.04	-0.04	-8.9
19	-0.20	0.27	0.31	0.41	0.31	-0.11	-0.05	-0.09	-13.8
20	-0.24	0.37	0.35	0.51	0.37	-0.12	-0.06	-0.12	-15.3
21	-0.51	0.53	0.51	0.74	-0.96	0.01	-0.03	-0.52	9.6

Notes: dq/dz is calculated from Darcy velocity magnitudes at 40 and 50 cm depth. q_{AR} and percent error κ_e are calculated from temperature time series extracted at 40 and 50 cm depth. VFLUX predicted the wrong direction of flux for Trial 21.

APPENDIX H

COMPARISON OF LOW AND HIGH ERROR TRIALS

For the purpose of verifying what determines the amount of error when calculating thermal derived flux or effective thermal diffusivity, we compare the model outputs of a trial with relatively low, and relatively high error. Trial 5 had comparatively low error where as Trial 11 had relatively higher errors than the other losing flow geometries tested. Both trials were subjected to the same thermal boundary conditions, but different hydraulic boundary conditions. The hydraulic boundary conditions for these two trials are outlined in Appendix A.

For the 8 pairs of temperature observation nodes used to calculate flux and effective thermal diffusivity, Trial 5 had a average error for amplitude ratio derived fluxes of 0.13 m/d and an average of 49% error for thermally derived effective thermal diffusivity. Trial 11 had an average amplitude ratio derived flux error of 0.62 m/d and an average error of effective thermal diffusivity of 159.2%. This is due to the higher degree of non-uniformity, and higher horizontal velocity magnitude of Trial 11. For the 8 pairs of temperature observation nodes, the average $\frac{dq}{dz}$ was -1.3 and -2.5 d^{-1} for Trials 5 and 11, respectively. The average q_h was 0.29 m/d and 0.64 m/d for Trials 5 and 11, respectively.

Figure H.1 shows the difference in hydraulic head between the two model runs. Trial 5 had heads ranging from 0.1993 to 0.2 m, while Trial 11 had heads from 0.19 to 0.2 m. Trial 11 had a greater head gradient, and thus larger groundwater velocity magnitudes in the x, y and z directions. Figure H.2 shows the Darcy velocity magnitude through cross sections through the middle of the model. We can define the magnitude of the Darcy velocity at any given point in the model as:

$$|q| = \sqrt{q_x{}^2 + q_y{}^2 + q_z{}^2}$$

In all model runs, areas of high velocity exist along any edge of the model where an inlet (i.e. head boundary) meets an outlet boundary. This is visible in the bottom left corner in the cross sections parallel to the X and Y axis for both trials (Figure H.2). Since temperatures were extracted from the center column of the model, these zones of high velocity did not effect our analysis.

Trial 5 **Trial 11**

Parallel to X axis, 0.5 m from X-head boundary/X-outlet

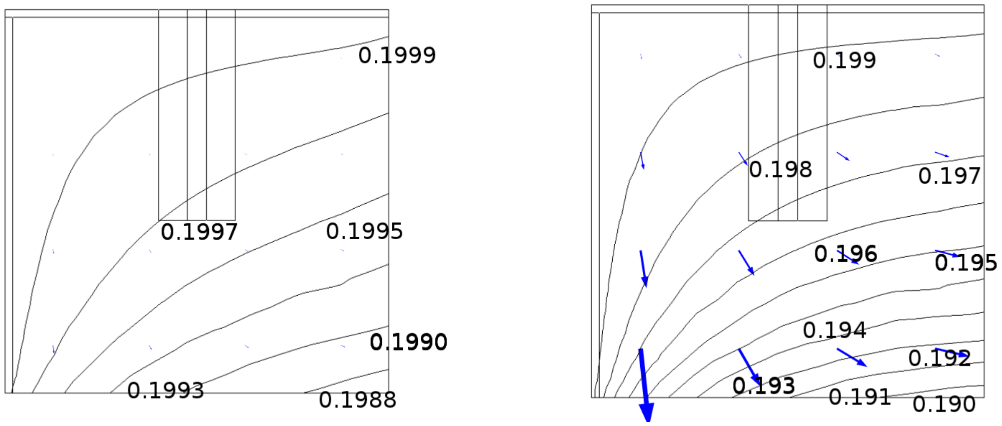

Parallel to Y axis, 0.5 m from Y-head boundary/X-outlet

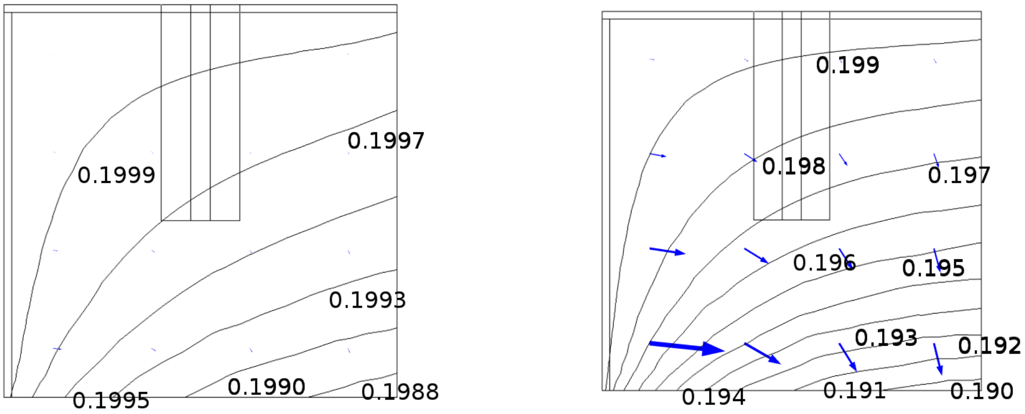

Parallel to top of model, 0.5 m from top head boundary/ bottom outlet

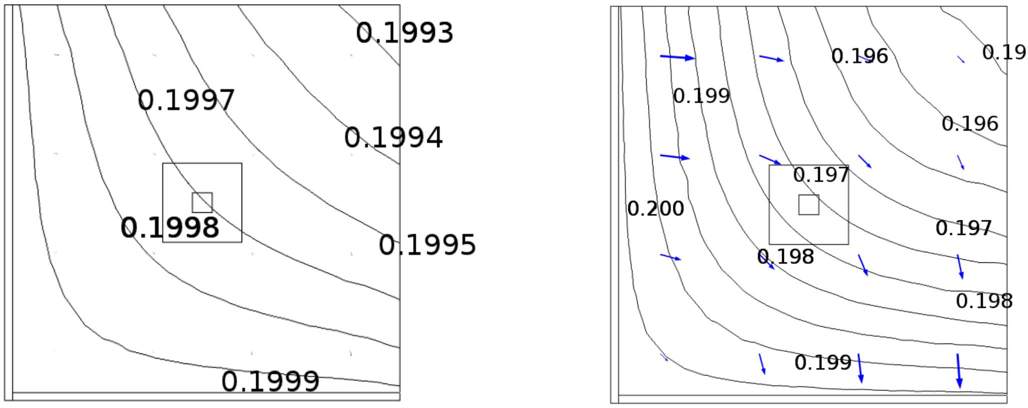

Figure H.1. Head contours (m) for cross sections through center of the model for Trial 5 (left column) and Trial 11 (right column). Blue arrows indicate groundwater flow magnitude and direction.

Figure H.3 shows temperature time series for both model runs. Trial 11 has a higher vertical velocity magnitude causing the surface temperature to propagate deeper into the subsurface, resulting in a greater amplitude with depth. Trial 5 has a weaker downward velocity component, and thus a greater delay in phase with depth. Since the downward velocity is slower, the timing of each peak at any given depth occurs later. The difference in $\frac{dq}{dz}$ is visibile between Trials 5 and 11. Near the center column of the model, there is a much greater change in Darcy velocity magnitude in Trial 11 than in Trial 5.

In a saturated system with vertical fluid flow with the same thermal boundary conditions, temperature contours will be horizontal within the model. In the presence of a non-uniform, multi-dimensional flow field, the thermal signal is propagated with depth at different rates throughout the model, causing temperature contours to be non-horizontal. Trial 11 has a substantially higher horizontal velocity component, as well as a higher degree of flow non-uniformity, resulting in the thermal signal propagating at a greater angle compared to Trial 5.

A.

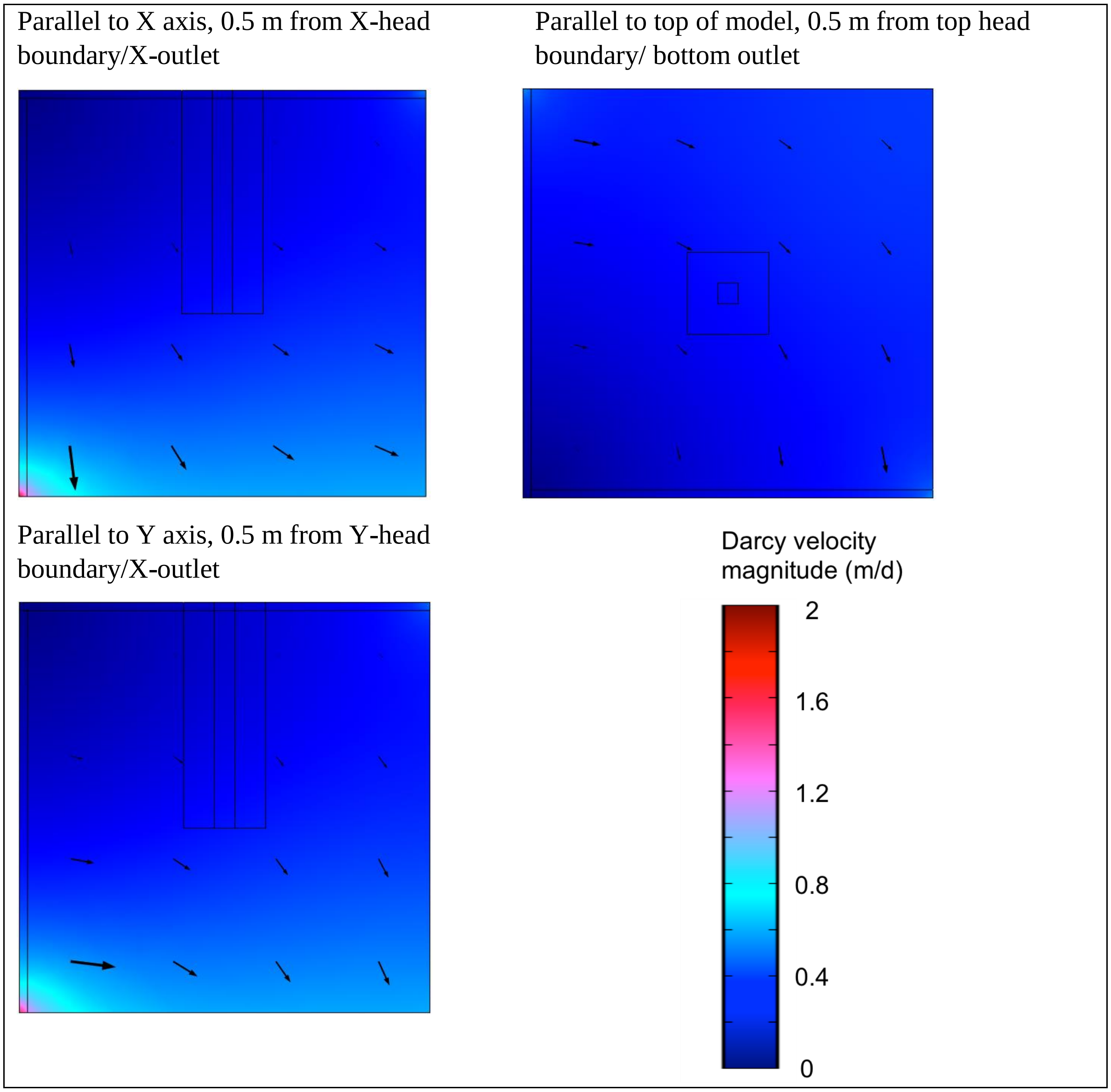

Parallel to X axis, 0.5 m from X-head boundary/X-outlet

Parallel to top of model, 0.5 m from top head boundary/ bottom outlet

Parallel to Y axis, 0.5 m from Y-head boundary/X-outlet

B.

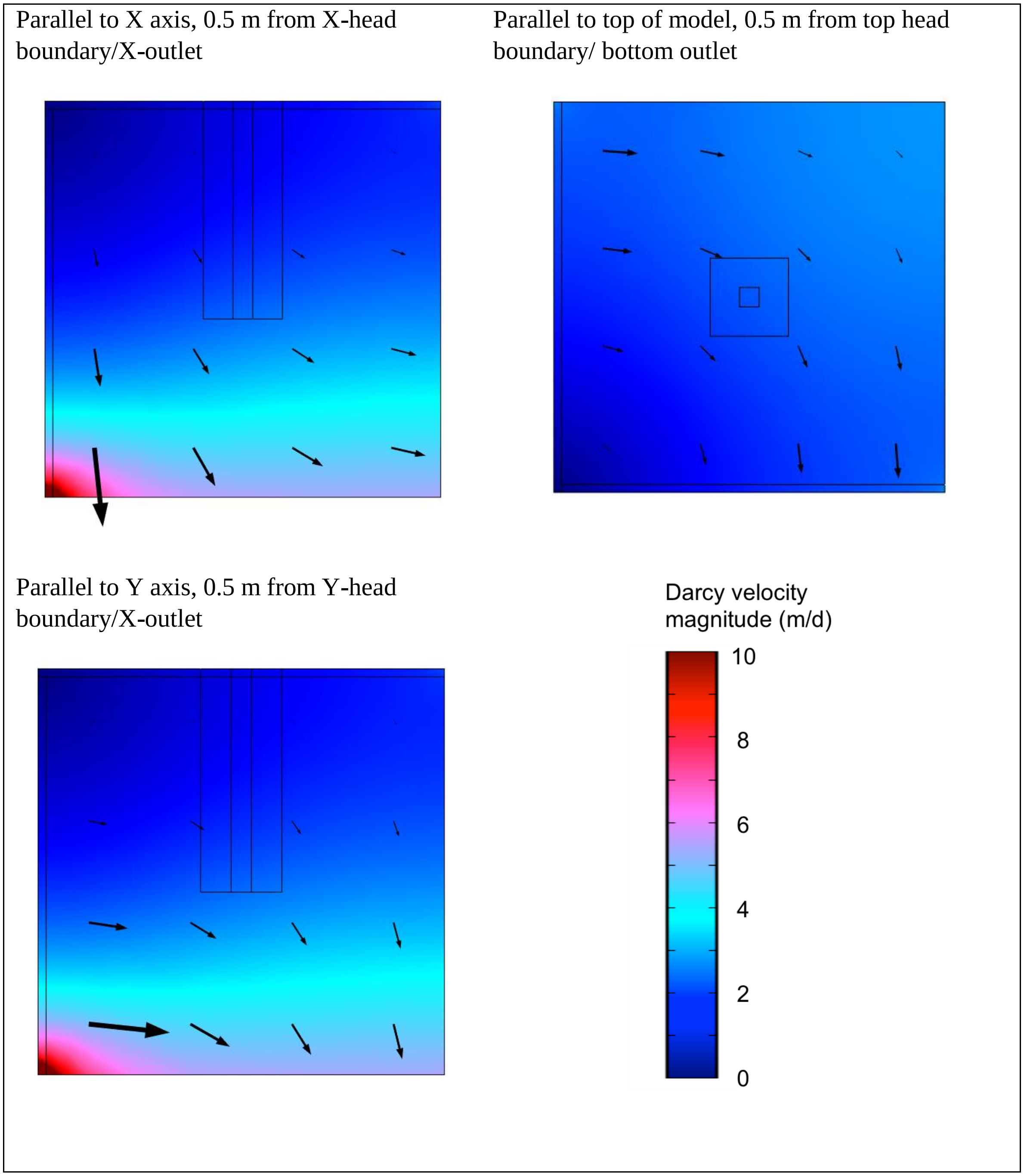

Parallel to X axis, 0.5 m from X-head boundary/X-outlet

Parallel to top of model, 0.5 m from top head boundary/ bottom outlet

Parallel to Y axis, 0.5 m from Y-head boundary/X-outlet

Figure H.2: Color map showing Darcy velocity magnitude (|q|) in three cross sections through the center of the model for Trial 5 (A) and Trial 11 (B). Black arrows indicate groundwater flow direction. Arrow length is proportional to velocity magnitude within the same trial. The scale factor for Trial 11 has been reduced so that the arrows would fit on the image.

A.

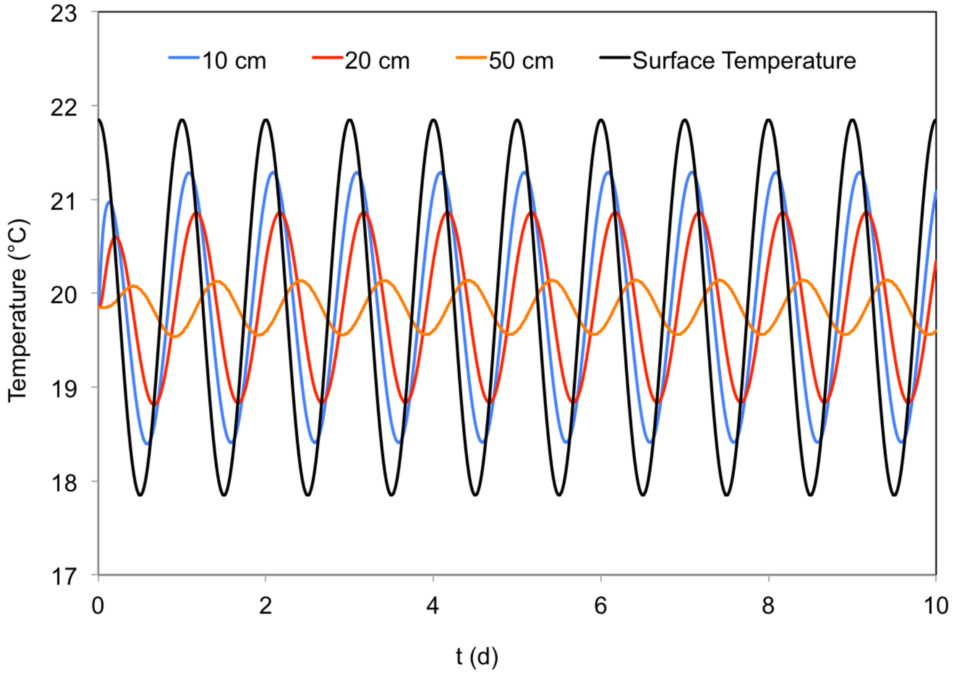

B.

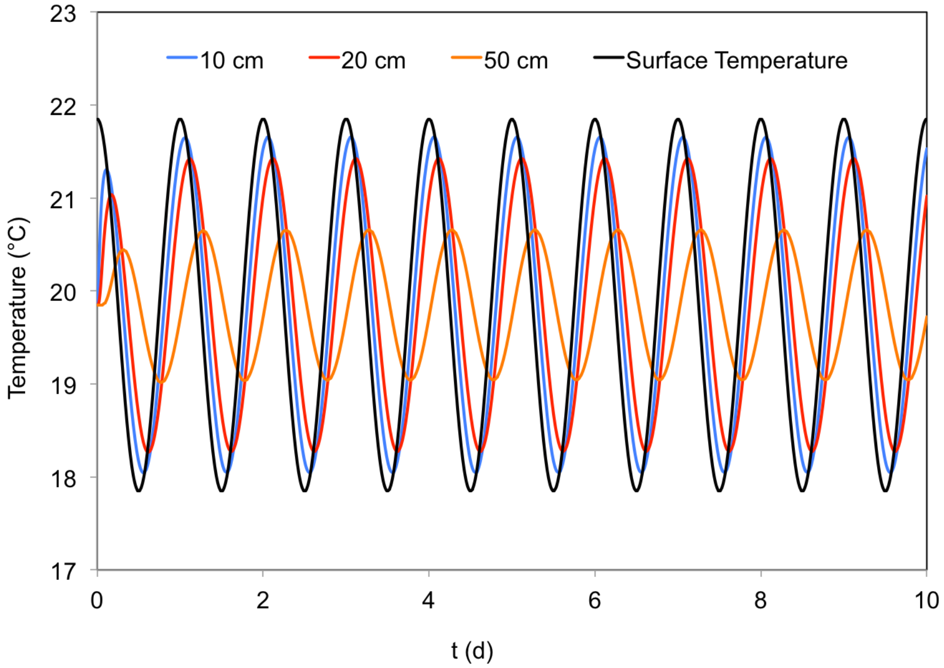

Figure H.3: Temperature time series for Trial 5 (A) and Trial 11 (B) at depths of 10, 20 and 50 cm. The surface temperature forcing (black line) is included as a reference and is identical in both figures.

A.

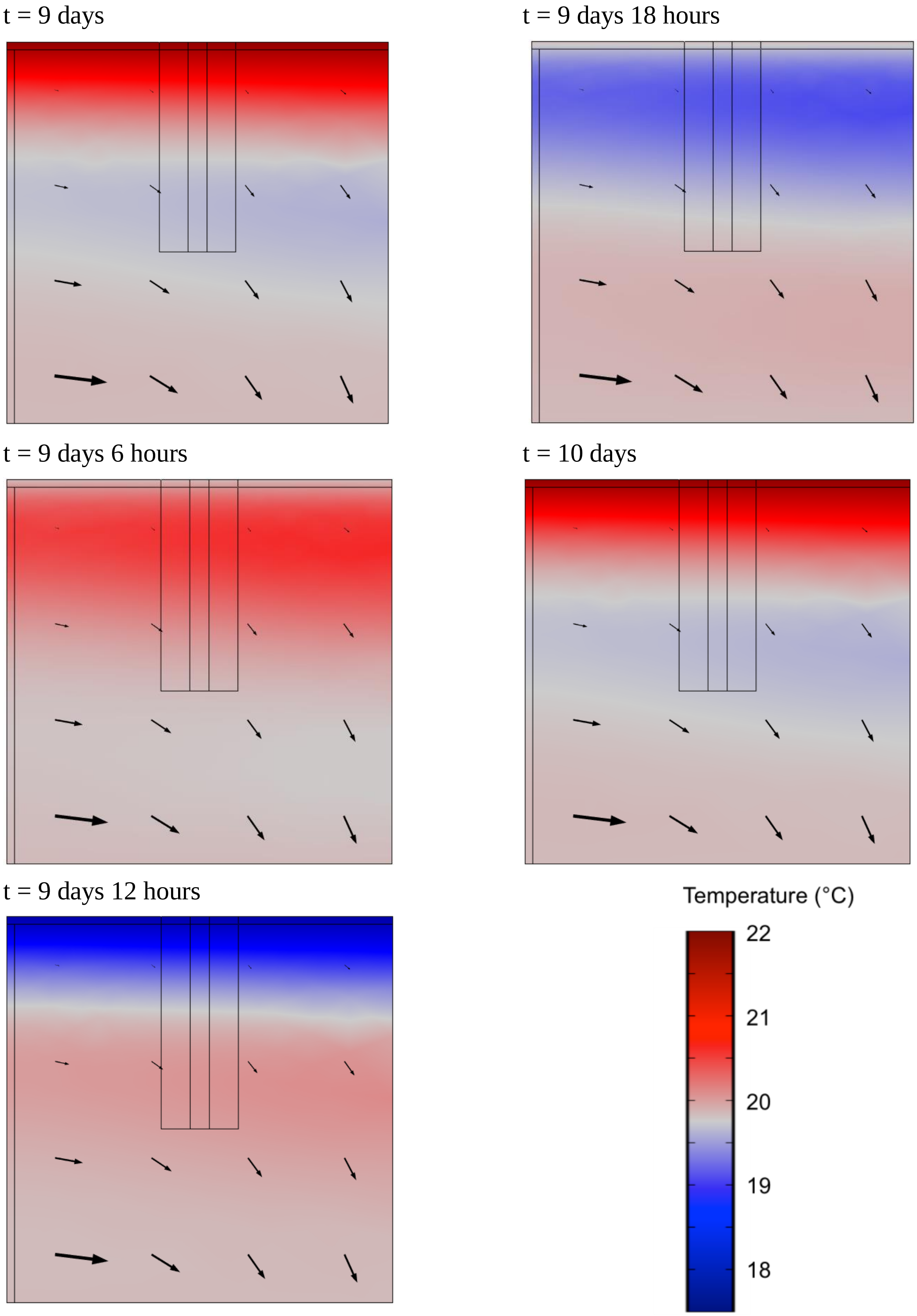

t = 9 days

t = 9 days 18 hours

t = 9 days 6 hours

t = 10 days

t = 9 days 12 hours

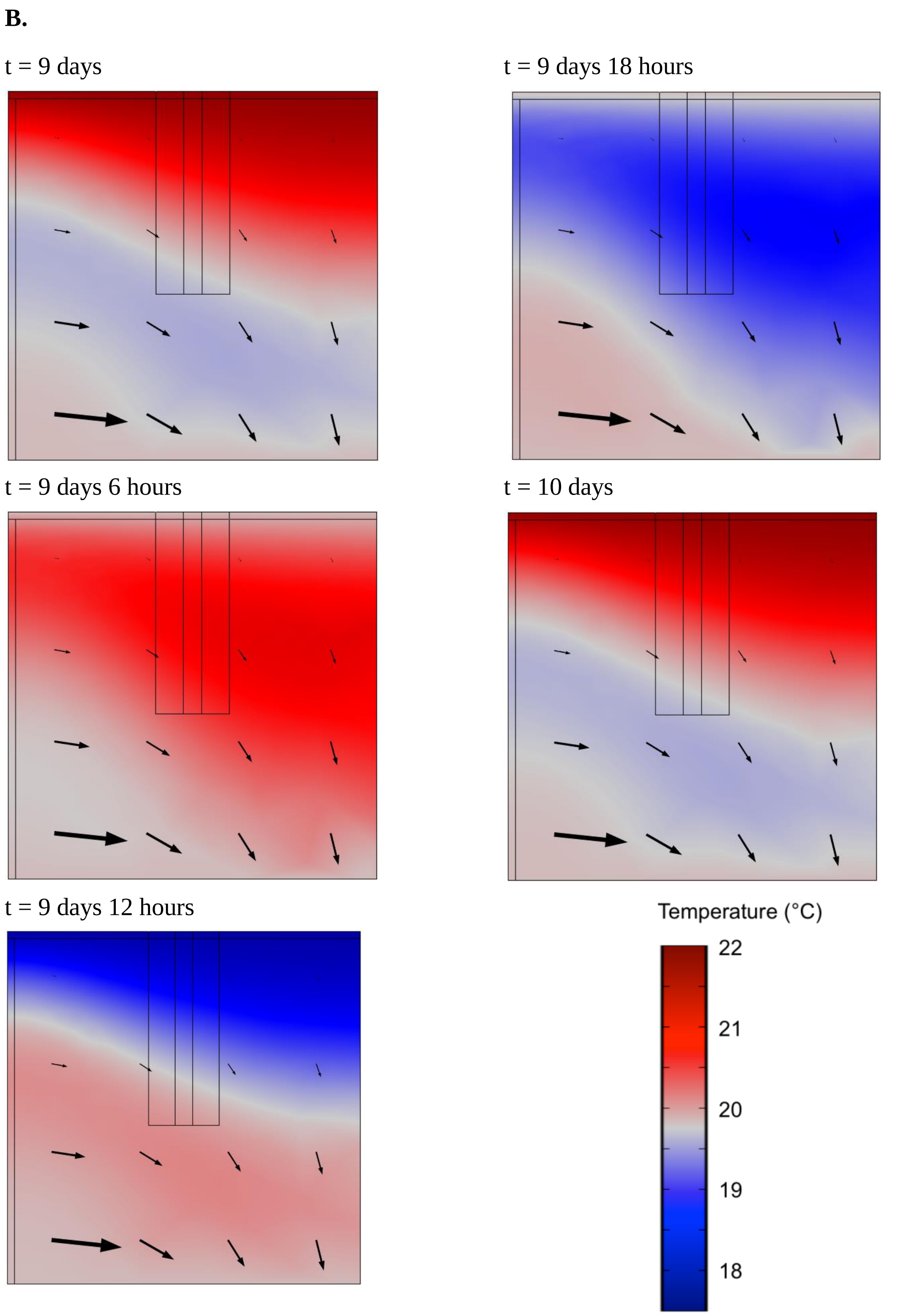

Figure H.4: Temperature cross sections in the middle of the model, parallel to the Y-axis, for Trials 5 (A) and 11 (B). Time steps begin a t=9 days and end at t=10 days with a 6 hour interval. Black arrows indicate groundwater flow direction. Arrows are proportional to velocity within each trial. Due to differences in the velocity magnitude between trials 5 and 11, a different scale factor was used so that the arrows would be visible.

APPENDIX I

PERFORMANCE OF VFLUX UNDER VERTICAL FLOW CONDITIONS

VFLUX uses dynamic harmonic regression (DHR) to extract amplitude ratio information from temperature time series. In order to quantify the amount of error VFLUX introduces into our thermally derived calculations of flux, we ran 5 vertical flow simulations at 2.5, 1.0, 0.1, -0.1 and -1.0 m/d through the 3D model. For losing conditions (q_z>0 m/d) a hydraulic head of 0.2 m was applied to the top of the model and a specified outlet velocity was applied to the bottom of the model. For gaining conditions, (q_z<0 m/d) a hydraulic head of 0.2 m was applied to the bottom of the model and a specified outlet velocity was set for the top of the model. For this analysis, the same thermal boundary conditions were used as in the bulk of the thesis. VFLUX performance was determined by calculating the amplitude ratio derived flux and thermal-derived κ_e using each pair of temperature observation nodes used in our model runs and comparing to the known modeled velocity and model input κ_e for each of the 5 vertical flow simulations.

Relatively large errors for both thermal-derived flux and effective thermal diffusivity occurred for the -1 m/d gaining flow field at depths when the deeper temperature observation node was at 40 cm depth or greater, resulting in the amplitude of surface diurnal signal being extinguished at the deeper temperature sensor beneath the resolution of the model. Therefore, we can ignore error estimates for both flux and temperature-derived κ_e for center depths greater than 25 cm when the vertical flux is -1 m/d. The maximum error occurred at 22.5 cm depth when vertical velocity in the model was 2.5 m/d. This larger error is a result of a high losing velocity and a sensor spacing of only 5 cm. The fast downward velocity propagates the surface signal such that the amplitude does not change (within the model resolution) between temperature observation nodes of 20 and 25 cm. We can ignore both error estimates at this depth since the sensor spacing is not large enough to capture the rapid downward propagation of the surface

temperature signal. For the thermal parameters and observation node spacings used in this study, when the downward velocities approach 2.5 m/d, the slope of the amplitude ratio solution space curves approach 0 (Figure 4a). Due to the decreased sensitivity of the amplitude ratio solution at this velocity, the errors are expected to be higher than for Darcy fluxes where the amplitude ratio solution space curves have a higher slope. Therefore, errors occurring as a result of vertical Darcy velocities between
-1 and 1 m/d are more indicative of the errors introduced by VFLUX throughout this thesis.

The maximum error for losing simulations where q_z is less than or equal to 1 m/d was 0.006 m/d which occurred at a purely vertical flux of 0.1 m/d, and was calculated using temperature observation nodes at 20 and 25 cm depth (Table I.1). The maximum error for gaining simulations was 0.008 m/d and occurred when a gaining velocity of -1 m/d was calculated using temperature observation nodes of 20 and 25 cm. Absolute errors in flux estimates for vertical velocities of -0.1 m/ d to 1 m/d were less than 0.006 m/d. This is a more representative value of the amount of error introduced since it more closely matches the range of fluxes analyzed in this thesis.

Errors in effective thermal diffusivity for these trials ranged from -28% occurring at a center depth of 22.5 cm for a 2.5 m/d velocity to 8.5% occurring at a center depth of 45 cm and a vertical velocity of -1 m/d (Table I.2). For fluxes ranging from -0.1 m/d to 1 m/d, errors in thermally-derived effective diffusivity were less than 3.2%. This error introduced is more representative for the calculations used in this thesis.

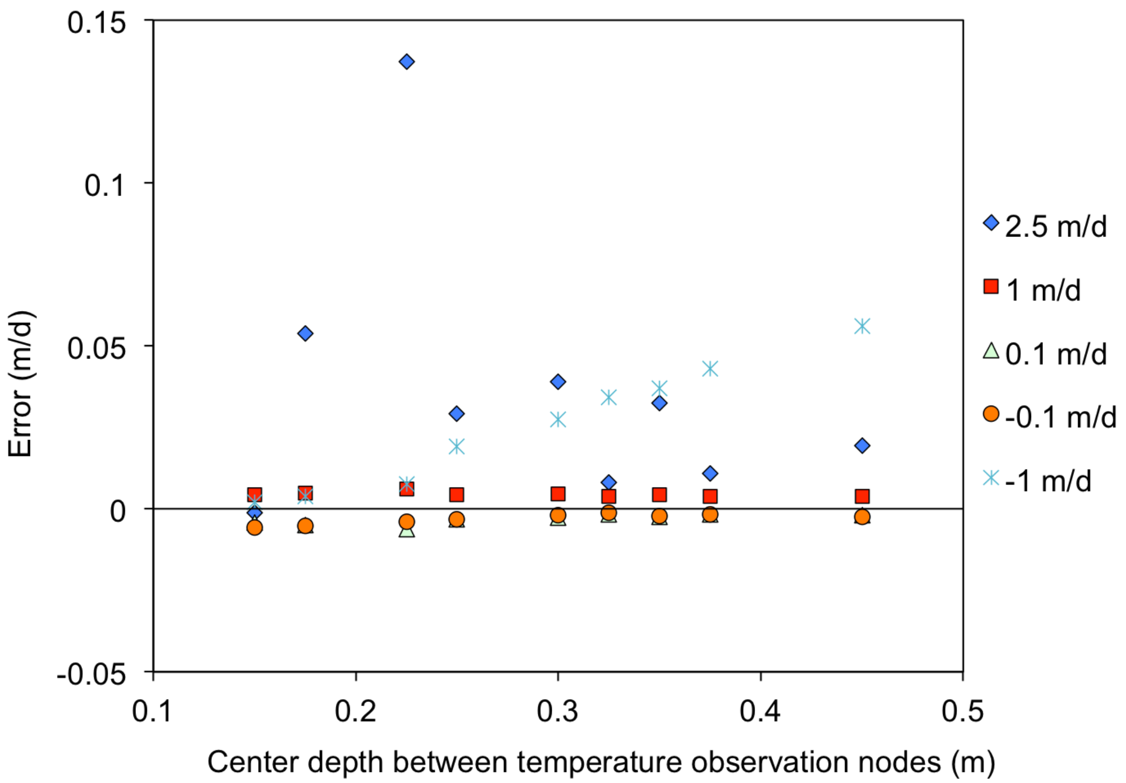

Figure I.1: Error (m/d) introduced by VFLUX for the range of purely vertical fluxes tested versus the center depth between the temperature observation nodes.

With the exception of the -1 m/d vertical flow field, there does not appear to be a correlation between center depth and error. For the strongest gaining flow field, error increases with center depth between temperature observation nodes. This is due to the surface signal being effectively extinguished at depths greater than 40 cm for this upward velocity. The largest errors occurred when the modeled velocity was 2.5 m/d. Errors in effective thermal diffusivity follow a similar trend (Table I.2) in that the largest errors occurred for the losing flow field with a downward velocity of 2.5 m/d. There is an increasing trend of larger percent error κ_e with increasing center depth when the upward velocity is 1 m/d. In summary, over the range of velocities tested, we expect VFLUX introduces errors up to 0.006 m/d for flux and up to 3.2% error for thermally derived effective thermal diffusivity.

Table I.1. Error in flux (m/d) introduced by VFLUX at center depth between temperature observation nodes at a range of fluxes. Red text indicates calculations where the amplitude of the surface signal does not propagate to the depth of the deeper temperature observation node. Green text indicates a temperature observation node spacing too narrow to capture the known modeled velocity.

Known modeled velocity (m/d)	Center depth of temperature observation nodes (m)								
	0.15	0.175	0.225	0.25	0.3	0.325	0.35	0.375	0.45
2.5	-0.001	0.054	0.137	0.029	0.039	0.008	0.033	0.011	0.019
1	0.004	0.005	0.006	0.004	0.005	0.004	0.004	0.004	0.004
0.1	-0.004	-0.005	-0.006	-0.003	-0.003	-0.002	-0.002	-0.002	-0.002
-0.1	-0.006	-0.005	-0.004	-0.003	-0.002	-0.001	-0.002	-0.002	-0.002
-1	0.002	0.004	0.008	0.019	0.028	0.034	0.037	0.043	0.056

Table I.2. Percent error in thermally derived effective thermal diffusivity introduced by VFLUX at center depth between temperature observation nodes at a range of fluxes. Red text indicates calculations where the amplitude of the surface signal does not propagate to the depth of the deeper temperature observation node. Green text indicates a temperature observation node spacing too narrow to capture the known modeled velocity.

Known modeled velocity (m/d)	Center depth of temperature observation nodes (m)								
	0.15	0.175	0.225	0.25	0.3	0.325	0.35	0.375	0.45
2.5	2.0	-7.3	-28.0	-4.2	-7.0	-1.7	-1.7	-5.4	-2.4
1	-1.7	-1.9	-2.2	-1.7	-1.7	-1.5	-1.5	-1.6	-1.4
0.1	-1.2	-1.1	-0.9	-	-0.1	0.2	0.8	-	1.8
-0.1	-0.5	-0.4	-0.4	-	0.9	1.3	2.0	-	3.2
-1	2.0	2.4	3.3	4.8	6.2	7.2	7.7	7.0	8.5

APPENDIX J

VALIDATION OF MODEL BOUNDARY CONDITIONS

In order to validate that the thermal boundary conditions are not controlling the results of the model simulations, we can show that the distance to the boundary of the model is not impacting the results at the center of the model. By showing that distance to the model boundary does not change the temperature distribution, we are effectively showing that cube of sand modeled in this study could be extended horizontally in either the x or y direction, without changing the results of the study. This validates the dimensions of the model, despite being smaller in size than similar numerical studies in two dimensions (e.g. Irvine et al. 2015, Cuthbert and Mackay 2013).

To validate the thermal boundary conditions used in this study, we show that the temperature profiles and velocity estimates of a 10 m by 1 m and a 1 m by 1 m 2D model are identical within model resolution. The 1 m by 1 m model overlaps the 10 m model between 5 and 6 m from the left boundary. The 10 m model was refined to 1 cm grid spacing in the top 55 cm of the model for the first 6 m from the left boundary. The 1 m model was refined for the top 55 cm for the entire model, such that both models have effectively identical grid spacing. This refinement was selected to match the mesh discretization used in the bulk of this thesis as well as to limit computation time.

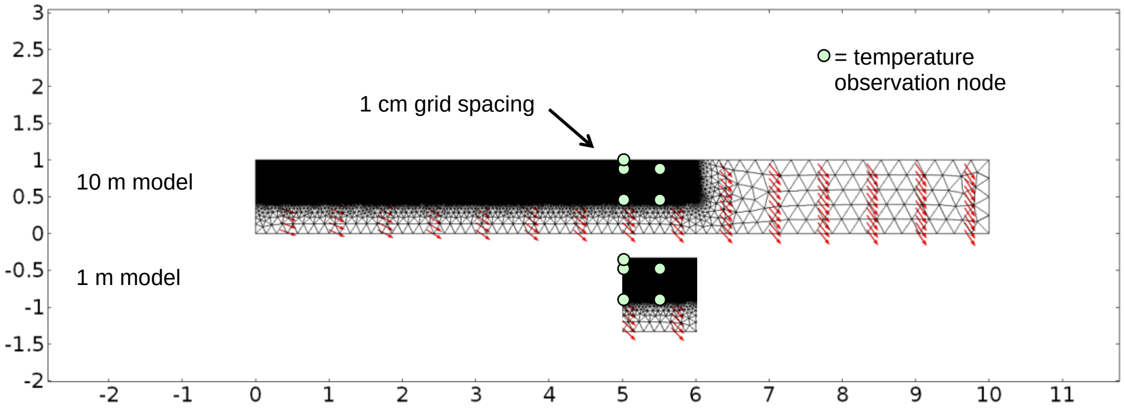

Figure J.1: Mesh discretization (black wireframe), flow direction (red arrows) and temperature observation node location (green circles) used for validation of model boundary conditions.

Groundwater flow is generated by specifying a horizontal Darcy velocity, and a vertical Darcy velocity which varies linearly across the model. Scenario 1 had a horizontal velocity of 0.4 m/d and Scenario 2 had a horizontal velocity of 0.8 m/d. Vertical Darcy velocity ranged from 0.25 m/d to 1.25 m/d for the 10 m model and from 0.75 m/d to 0.85 m/d for the 1 m model. The vertical velocity at 5 and 6 m from the left boundary for the 10 m model was 0.75 m/d and 0.85 m/d, respectively.

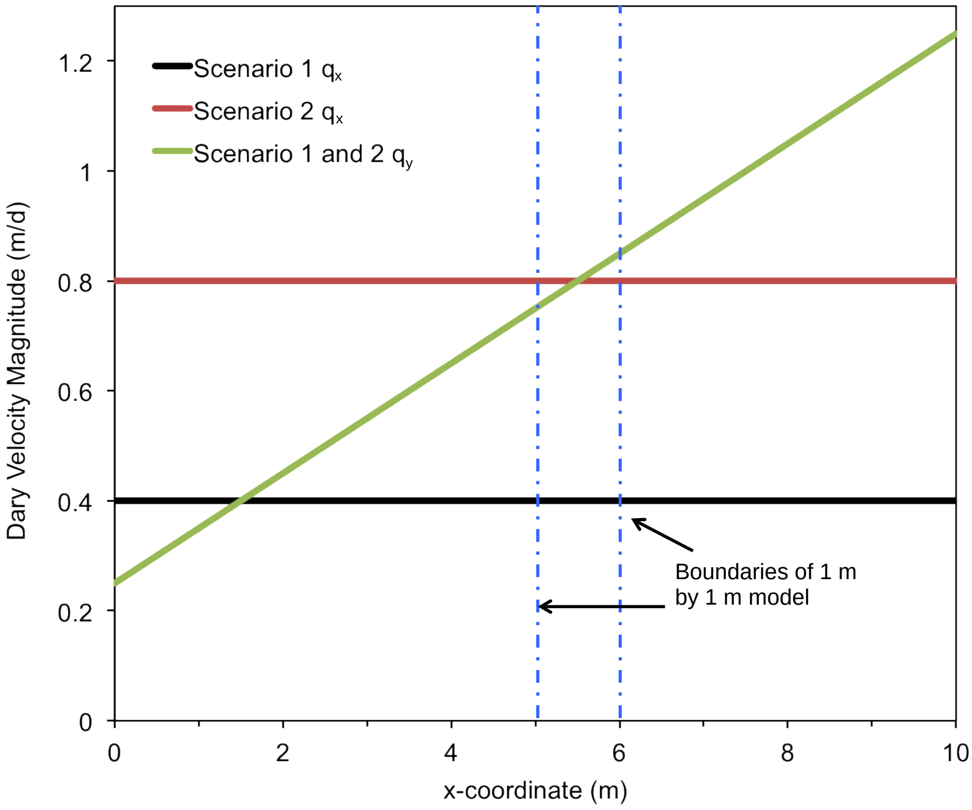

Figure J.2: Darcy velocity magnitude (m/d) across model for Scenarios 1 and 2.

The 2D model is setup with the same thermal boundary conditions as the 3D model used for this thesis. The top boundary for both models is a diurnal sinusoidal temperature variation with amplitude of 2°C. Thermal boundary conditions of the model are set as no heat flux on the sides of the model and a constant temperature is applied to the bottom of the model. The following graphics show COMSOL outputs for the last day of the model with 6 hour time steps for Scenarios 1 and 2. Results from the 1 m model are shown below the 10 m model. Temperature in degrees Celsius is shown via the color map with the maximum and minimum temperatures occurring at that time step above and below the temperature scale, respectively.

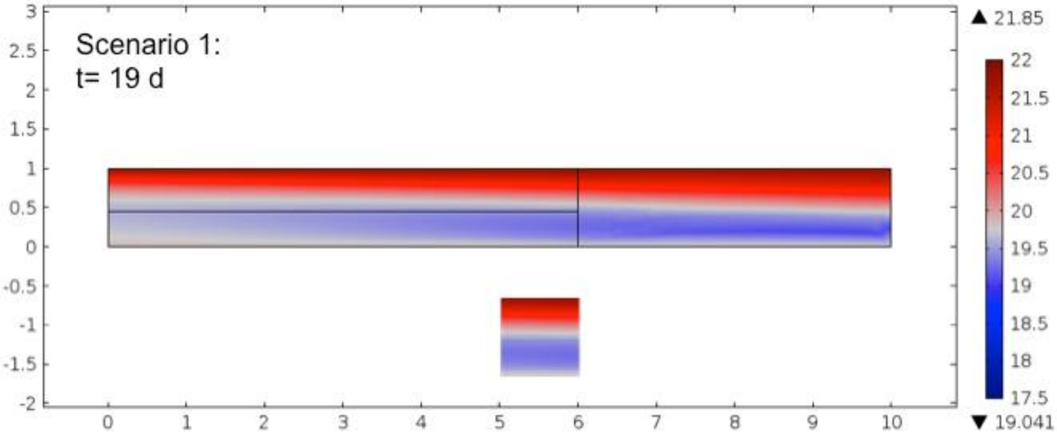

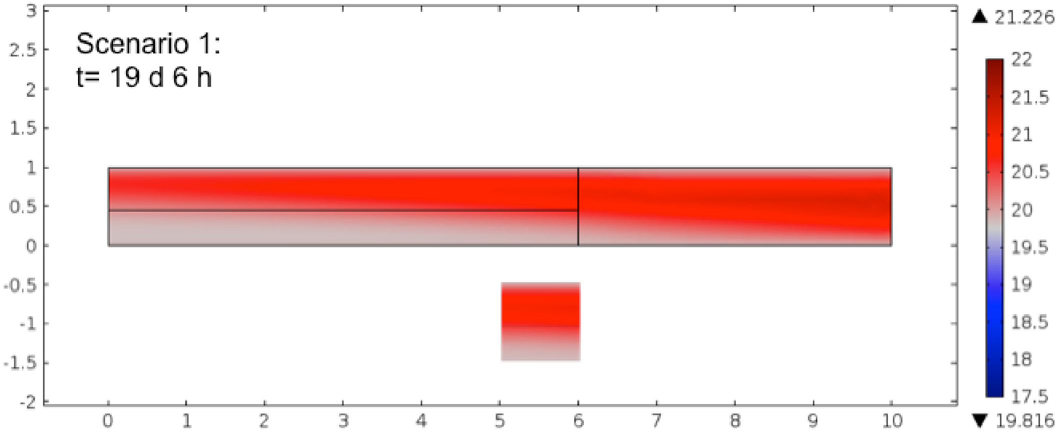

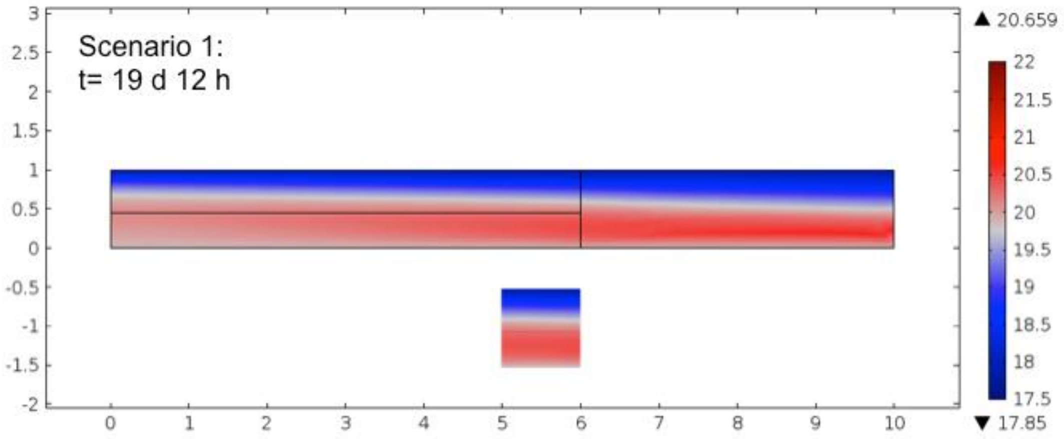
Scenario 1:
t= 19 d 12 h
3
2.5
2
1.5
1
0.5
0
-0.5
-1
-1.5
-2
0
1
2
3
4
5
6
7
8
9
10
▲ 20.659
22
21.5
21
20.5
20
19.5
19
18.5
18
17.5
▼ 17.85

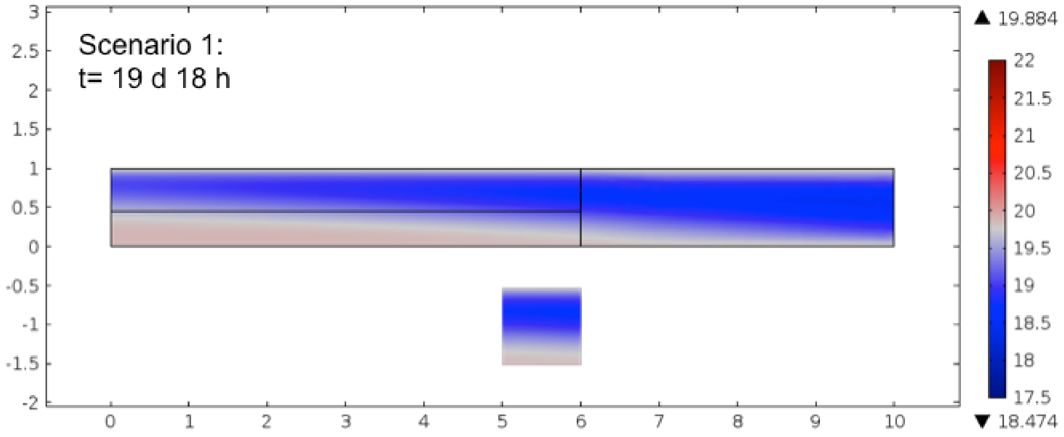
Scenario 1:
t= 19 d 18 h
3
2.5
2
1.5
1
0.5
0
-0.5
-1
-1.5
-2
0
1
2
3
4
5
6
7
8
9
10
▲ 19.884
22
21.5
21
20.5
20
19.5
19
18.5
18
17.5
▼ 18.474

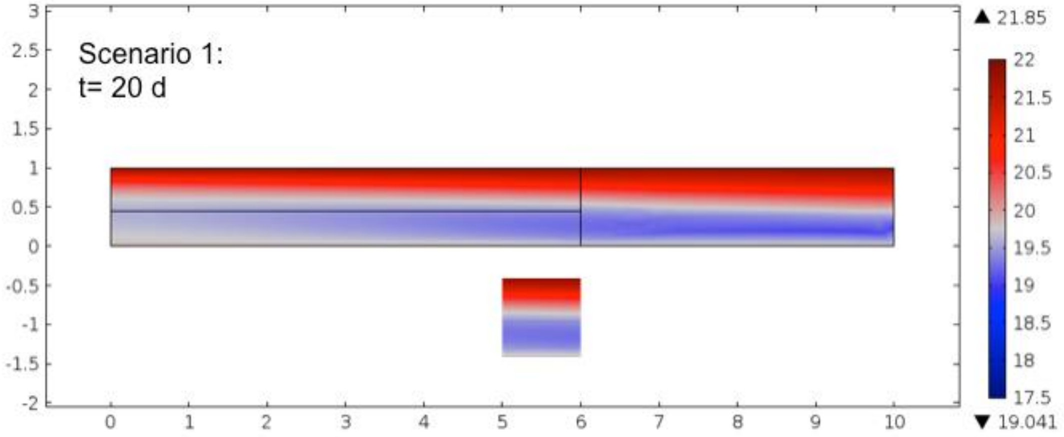
Scenario 1:
t= 20 d
3
2.5
2
1.5
1
0.5
0
-0.5
-1
-1.5
-2
0
1
2
3
4
5
6
7
8
9
10
▲ 21.85
22
21.5
21
20.5
20
19.5
19
18.5
18
17.5
▼ 19.041

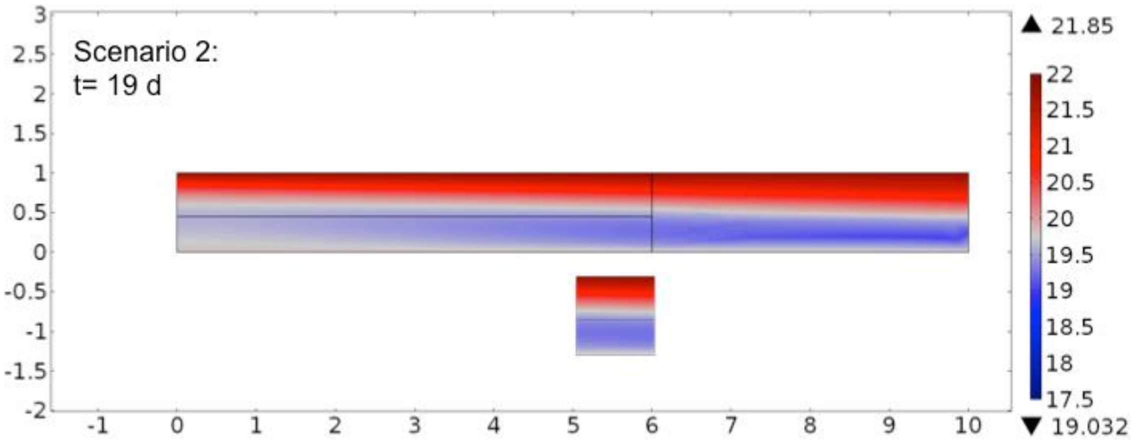
Scenario 2:
t= 19 d
▲ 21.85
22
21.5
21
20.5
20
19.5
19
18.5
18
17.5
▼ 19.032
3
2.5
2
1.5
1
0.5
0
-0.5
-1
-1.5
-2
-1
0
1
2
3
4
5
6
7
8
9
10

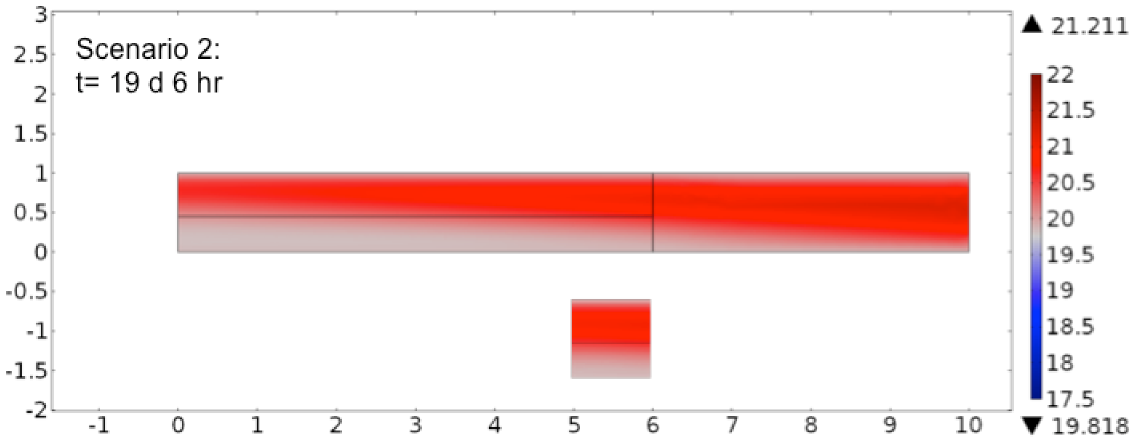
Scenario 2:
t= 19 d 6 hr
▲ 21.211
22
21.5
21
20.5
20
19.5
19
18.5
18
17.5
▼ 19.818
3
2.5
2
1.5
1
0.5
0
-0.5
-1
-1.5
-2
-1
0
1
2
3
4
5
6
7
8
9
10

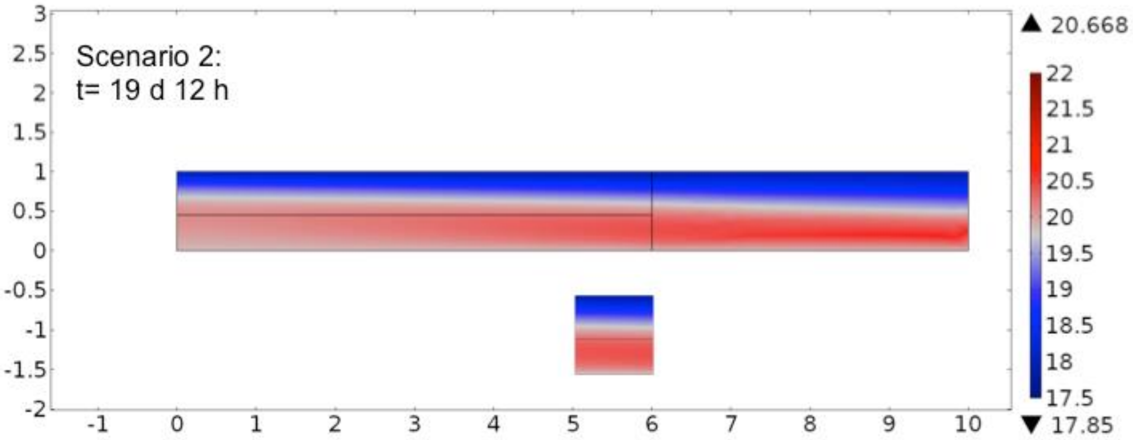
Scenario 2:
t= 19 d 12 h
▲ 20.668
22
21.5
21
20.5
20
19.5
19
18.5
18
17.5
▼ 17.85
3
2.5
2
1.5
1
0.5
0
-0.5
-1
-1.5
-2
-1
0
1
2
3
4
5
6
7
8
9
10

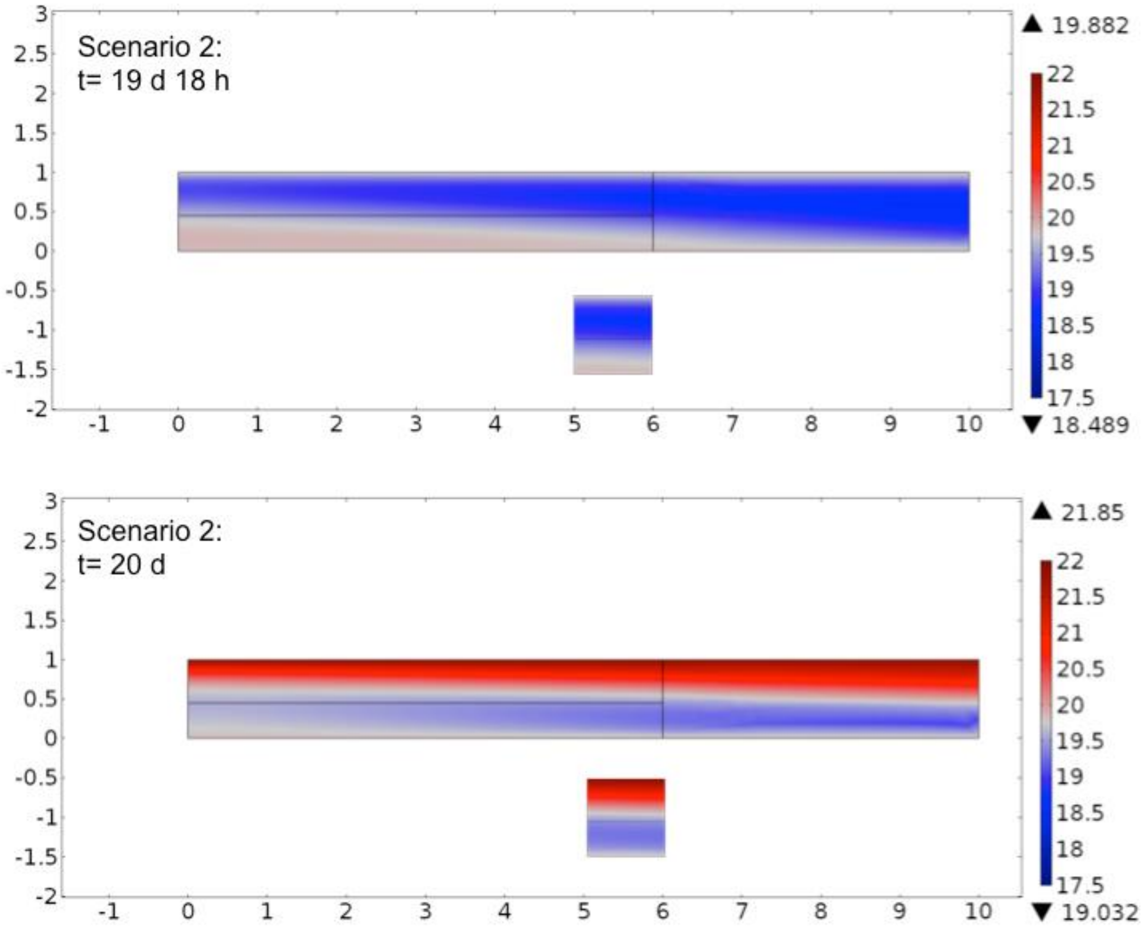

Figure J.3: Model temperature for the last day of the 20 day model run with a 6 hour time-step for Scenarios 1 and 2.

For both scenarios, the thermal isotherms have roughly the same slope, despite having different horizontal velocity magnitudes. This is due to the downward velocity playing a larger role in controlling the location of the isotherms. Increasing vertical velocities transport heat downwards. As vertical velocity changes across the model, the depth of each isotherm also changes. This creates the slope of the isotherm, rather than the magnitude of the horizontal velocity.

Within the overlapping sections of the model, temperature time series were compared at 5 locations. Temperature time series were extracted at depths of 0, 10 and 50 cm on the left boundary of the 1 m model (5 m across the 10 m model) and depths of 10 cm and 50 cm in the center of the 1 m model (5.5 m across the 10 m model) for both Scenarios. Temperature time series from the 1 m model were subtracted from the corresponding locations in the 10 m model. For Scenario 1 with 0.4 m/d horizontal velocity, the maximum difference in temperature at the 5 extracted temperature time series was 0.03°C once the model equilibrated to quasi-steady state. For Scenario 2 with 0.8 m/d horizontal velocity, the maximum difference in temperature at the 5 extracted temperature time series was 0.035°C once the model equilibrated to quasi-steady state. Differences in temperature were largest at the left boundary of the 1 m model (5 m across the 10 m model) at a depth of 50 cm. We suspect this is due to slight changes in mesh discretization. In the 1 m model, this location occurs on an edge of the model, whereas this point occurs in the center of the 10 m model. However, for the purpose of the thesis, temperature time series were extracted from the center of the 3D model, and the errors presented here represent a maximum potential error as a result of the boundary conditions.

Scenario 1:

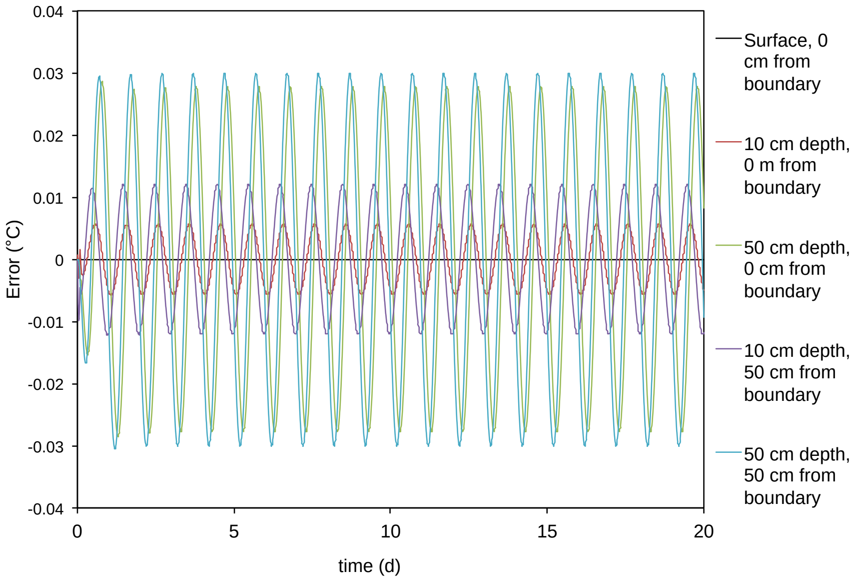

Scenario 2:

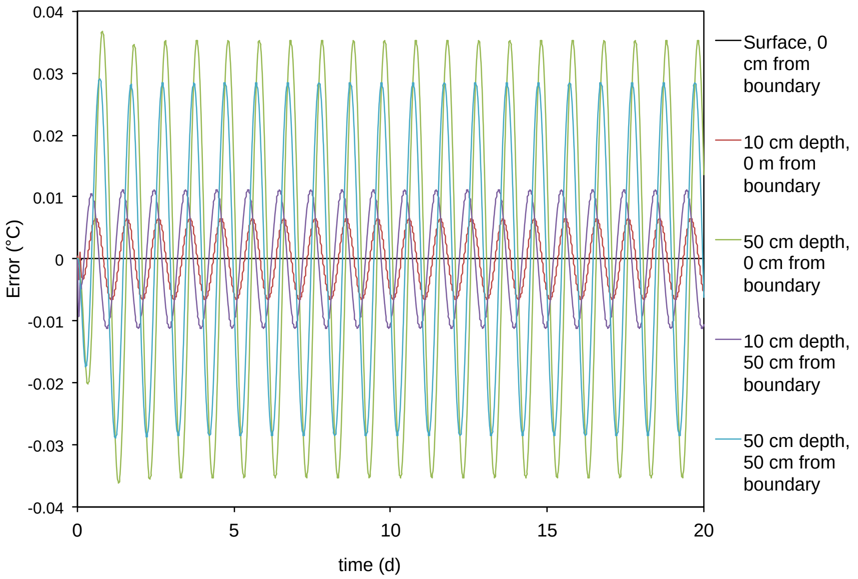

Figure J.4: Temperature time series recorded at all temperature observation nodes used for validation of model boundary conditions for Scenarios 1 and 2.

Temperature time series were then analyzed in VFLUX using the same methods used for the 3D model. Predicted fluxes between the 10 m and 1 m model differed by less than 0.03 m/d. This difference is low enough such that it is within the resolution of the 2D model. Additionally, VFLUX could have introduced additional error in the filtering process.

Table J.1: Calculations and error analysis used for validation of model boundary conditions.

Model Size (m)	10	1	10	1	10	1	10	1
q_h (m/d)	0.4	0.4	0.4	0.4	0.8	0.8	0.8	0.8
Distance across model (m)	5.0	0.0	5.5	0.5	5.0	0.0	5.5	0.5
Actual q_z (m/d)	0.75	0.75	0.85	0.85	0.75	0.75	0.85	0.85
Average q_{Ar} for last day of flux calculations (m/d)	0.69	0.71	0.73	0.74	0.68	0.71	0.72	0.73
Error (m/d)	0.06	0.04	0.12	0.11	0.07	0.04	0.13	0.12
Percent Error	8.0	5.3	14.6	12.9	9.0	5.6	15.6	13.8
Difference in error between 10 m model, and 1 m model (m/d)	0.020		0.015		0.025		0.015	

Since the temperature distributions are nearly identical for the 10 m and 1 m model, we can conclude that the thermal boundary conditions are not driving the results of this study.

APPENDIX K

RESULTS FIGURES USING ONLY ADJACENT TEMPERATURE OBSERVATION NODES

This appendix contains Figures 5, 6, 7, 8 and 9 using thermal calculations from exclusively adjacent temperature observation nodes. The figures are separated by center depth between the two observation nodes to show how hydraulic and thermal conditions are changing with depth in the model.

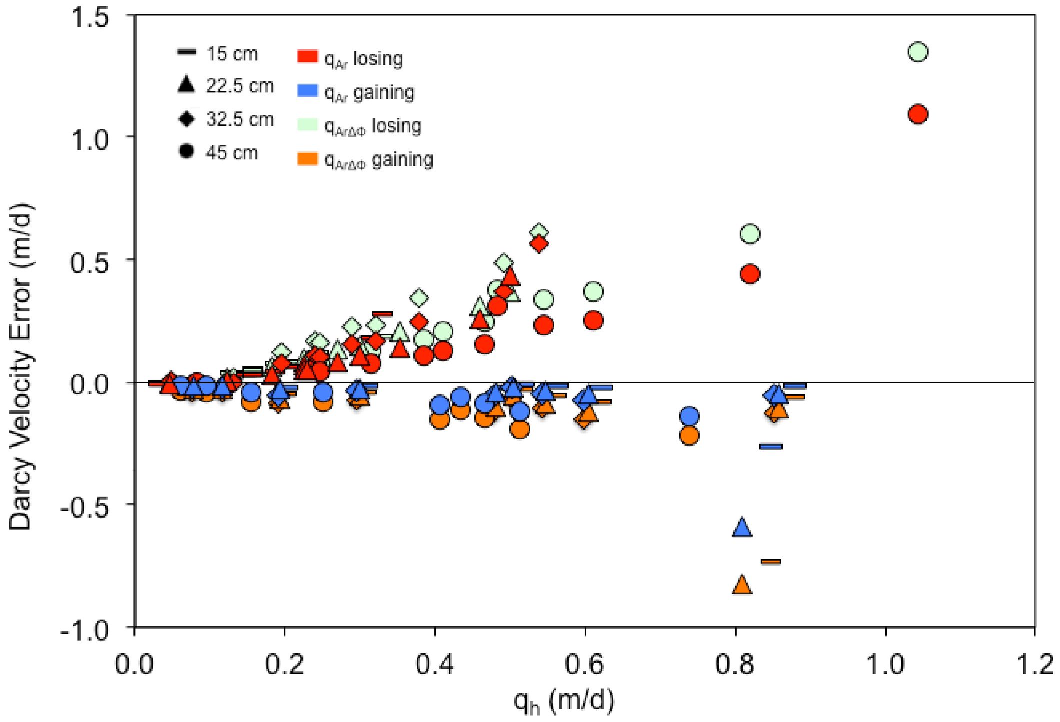

Figure K.1: Performance of amplitude ratio, q_{AR} and combined amplitude ratio/phase shift, $q_{Ar\Delta\Phi}$, heat-as-a-tracer methods compared to horizontal Darcy velocity magnitude, q_h, for both gaining and losing flow geometries.

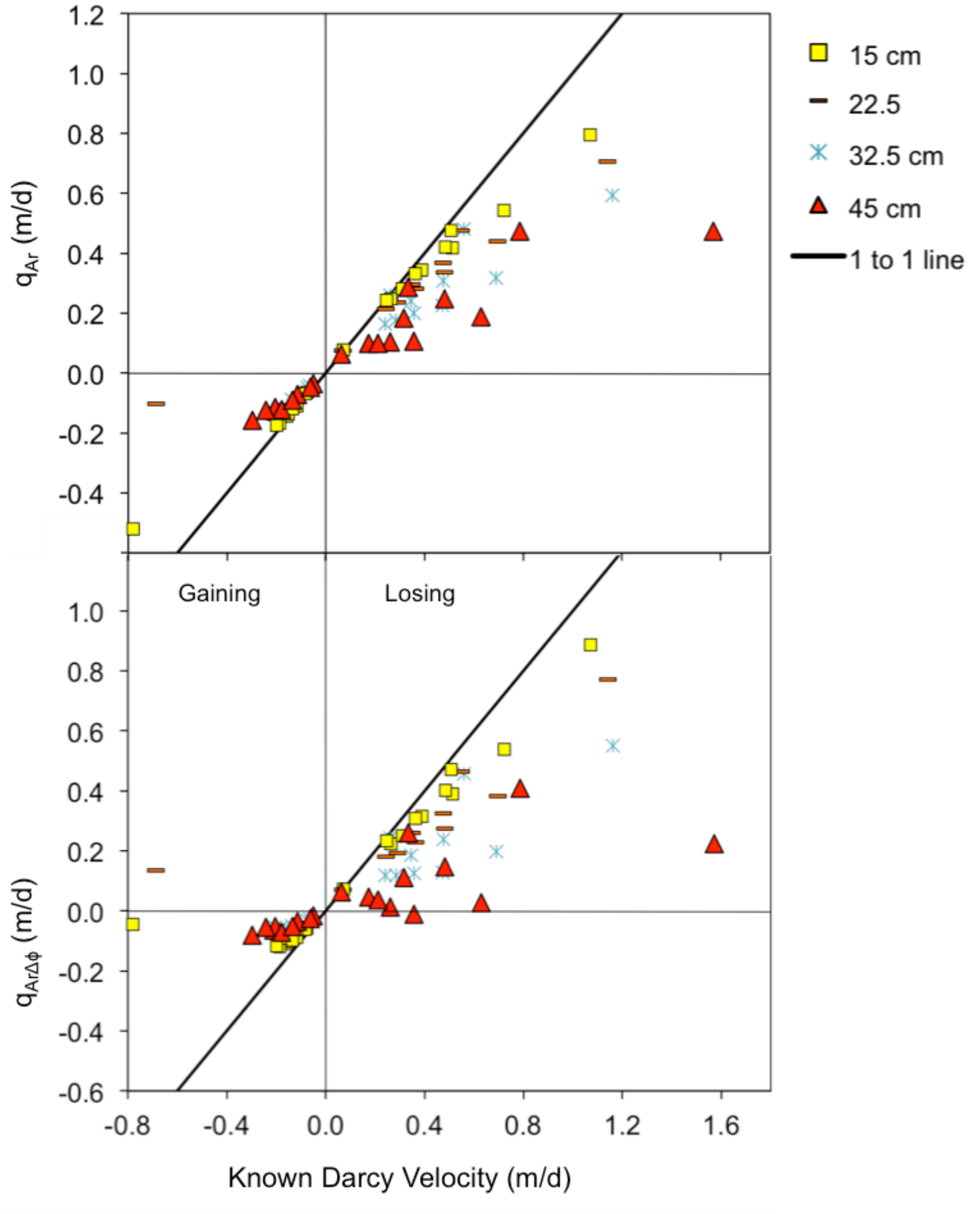

Figure K.2: Known Darcy velocity compared to amplitude ratio derived flux ($q_{Ar)}$ (top) and combined amplitude ratio and phase shift derived flux ($q_{Ar\Delta\phi})_{\phi}$ (bottom) separated by center depth between temperature observation nodes. Black diagonal lines are the 1 to 1 lines. Temperature derived fluxes are calculated from temperature time series extracted at depths of 10, 20, 25, 40 and 50 cm.

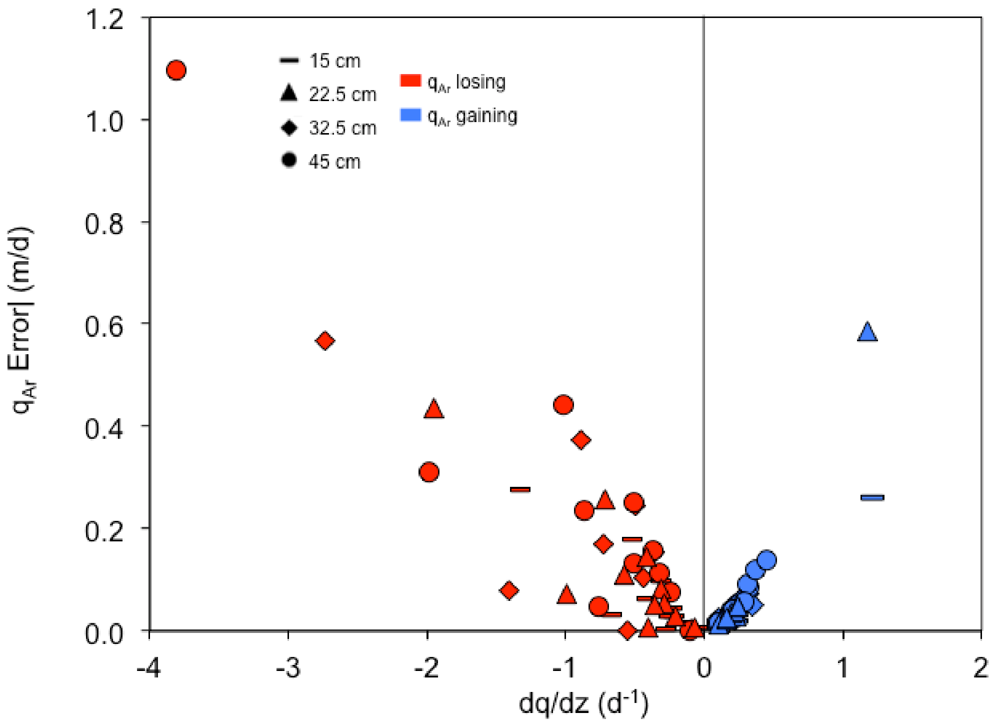

Figure K.3: Error response for amplitude ratio derived fluxes as a function of degree of flow non-uniformity dq/dz for losing (red triangles) and gaining (blue diamonds) groundwater flows.

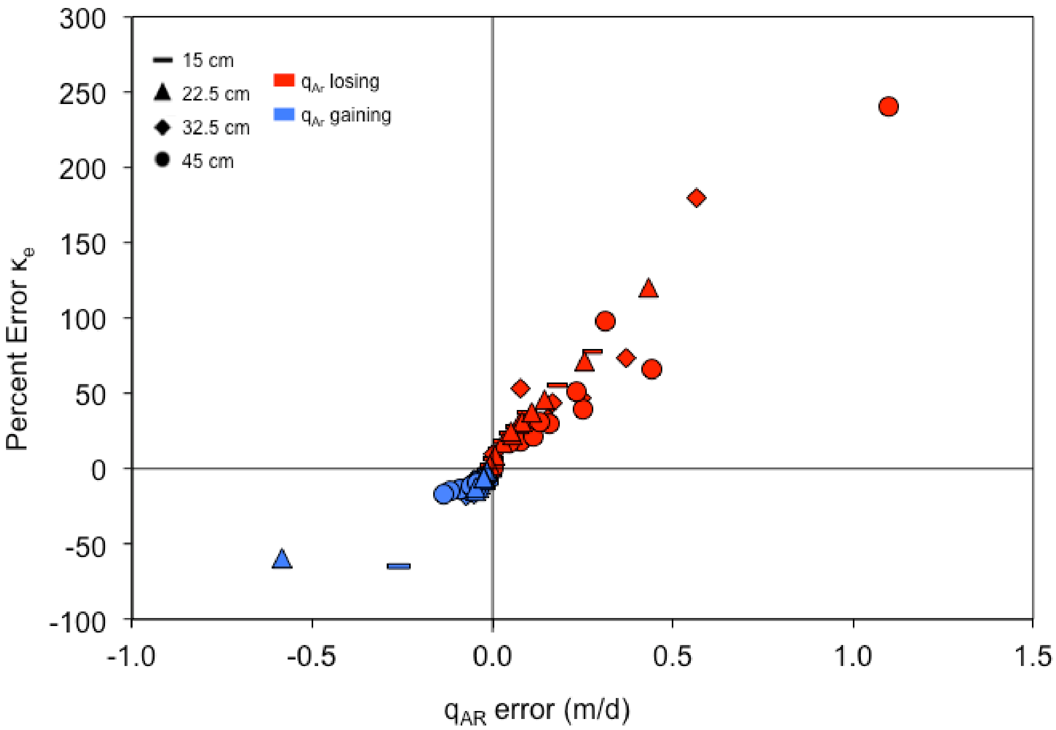

Figure K.4: Percent error in temperature derived effective thermal diffusivity, κ_e, compared to amplitude ratio derived Darcy velocity error for gaining (blue diamond) and losing (red triangle) groundwater flow paths. Percent error κ_e is positive when temperature derived κ_e under predicts actual modeled . Negative values of Percent error κ_e indicate over predicted temperature derived κ_e.

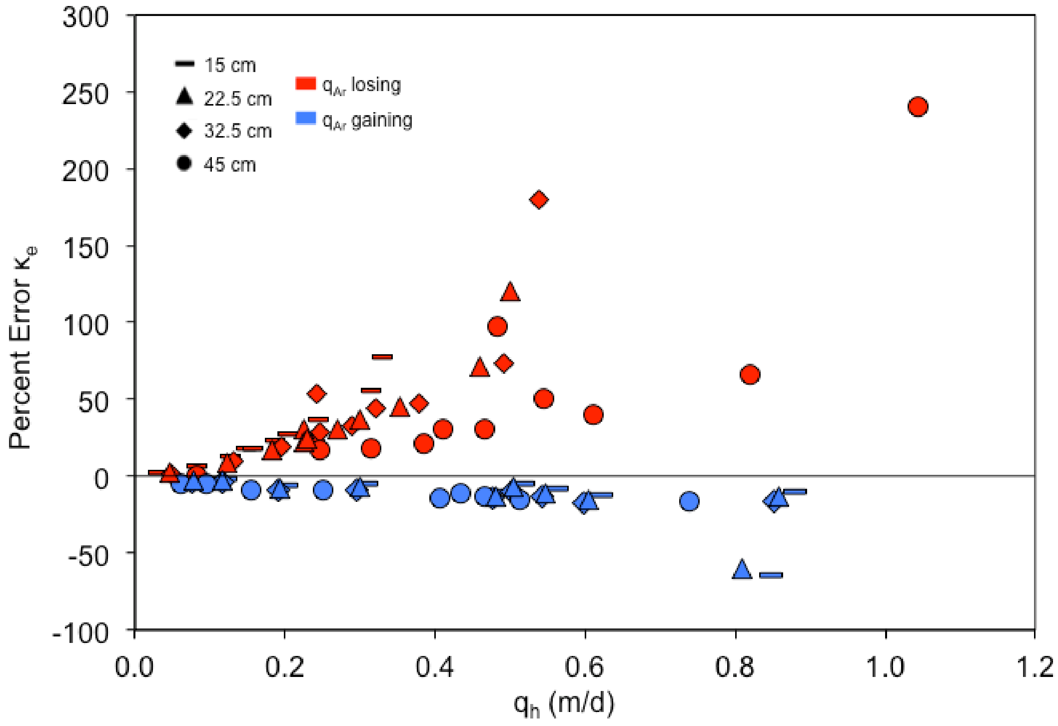

Figure K.5: Percent error in temperature derived effective thermal diffusivity, κ_e, compared to horizontal Darcy flux magnitude for gaining (blue diamond) and losing (red triangle) groundwater flow paths.

BIBLIOGRAPHY

Anderson, M.P., 2005, Heat as a groundwater tracer: Ground water, v. 43, p. 951–68, doi: 10.1111/j.1745-6584.2005.00052.x.

Baxter, C. V, and Hauer, F.R., 2000, Geomorphology, hyporheic exchange, and selection of spawning habitat by bull trout (Salvelinus confluentus): Canadian Journal of Fisheries and Aquatic Sciences, v. 57, p. 1470–1481.

Bhaskar, A.S., Harvey, J.W., and Henry, E.J., 2012, Resolving hyporheic and groundwater components of streambed water flux using heat-as-a-tracer: Water Resources Research, v. 48, p. n/a–n/a, doi: 10.1029/2011WR011784.

Boano, F., Demaria, A., Revelli, R., and Ridolfi, L., 2010, Biogeochemical zonation due to intrameander hyporheic flow: Water Resources Research, v. 46, p. 1–13, doi: 10.1029/2008WR007583.

Bredehoeft, J.D., and Papaopulos, I.S., 1965, Rates of vertical groundwater movement estimated from the Earth's thermal profile: Water Resources Research, v. 1, p. 325, doi: 10.1029/WR001i002p00325.

Briggs, M. A., Lautz, L.K., Buckley, S.F., and Lane, J.W., 2014, Practical limitations on the use of diurnal temperature signals to quantify groundwater upwelling: Journal of Hydrology, v. 519, p. 1739–1751, doi: 10.1016/j.jhydrol.2014.09.030.

Briggs, M. A., Lautz, L.K., and McKenzie, J.M., 2012, A comparison of fiber-optic distributed temperature sensing to traditional methods of evaluating groundwater inflow to streams: Hydrological Processes, v. 26, p. 1277–1290, doi: 10.1002/hyp.8200.

Briggs, M. A., Lautz, L.K., McKenzie, J.M., Gordon, R.P., and Hare, D.K., 2012, Using high-resolution distributed temperature sensing to quantify spatial and temporal variability in vertical hyporheic flux: Water Resources Research, v. 48, p. n/a–n/a, doi: 10.1029/2011WR011227.

Brunke, M., and Gonser, T., 1997, The ecological significance of exchange processes between rivers and groundwater: Freshwater Biology, v. 37, p. 1–33, doi: 10.1046/j.1365-2427.1997.00143.x.

Carslaw, H.S., and Jaeger, J.C., 1959, Conduction of Heat in Solids: Oxford, U.K., Clarendon, 510 p.

Constantz, J., 2008, Heat-as-a-tracer to determine streambed water exchanges: Water Resources Research, v. 44, p. n/a–n/a, doi: 10.1029/2008WR006996.

Constantz, J., 1994, Influence of diurnal variations in stream temperature on streamflow loss and groundwater recharge: Water Resources Research, v. 30, p. 3253–3264.

Cuthbert, M.O., and Mackay, R., 2013, Impacts of nonuniform flow on estimates of vertical streambed flux: Water Resources Research, v. 49, p. 19–28, doi: 10.1029/2011WR011587.

Derx, J., Blaschke, a. P., and Blöschl, G., 2010, Three-dimensional flow patterns at the river-aquifer interface - a case study at the Danube: Advances in Water Resources, v. 33, p. 1375–1387, doi: 10.1016/j.advwatres.2010.04.013.

Elliott, A., and Brooks, N., 1997, Transfer of nonsorbing solutes to a streambed with bed forms: Laboratory experiments: Water Resources Research, v. 33, p. 137–151.

Findlay, S., 1995, Importance of surface-subsurface The hyporheic zone exchange in stream ecosystems : Limnology and Oceanography, v. 40, p. 159–164.

Gordon, R.P., Lautz, L.K., Briggs, M. a., and McKenzie, J.M., 2012, Automated calculation of vertical pore-water flux from field temperature time series using the VFLUX method and computer program: Journal of Hydrology, v. 420-421, p. 142–158, doi: 10.1016/j.jhydrol.2011.11.053.

Gordon, R.P., Lautz, L.K., and Daniluk, T.L., 2013, Spatial patterns of hyporheic exchange and biogeochemical cycling around cross-vane restoration structures: Implications for stream restoration design: Water Resources Research, v. 49, p. 2040–2055, doi: 10.1002/wrcr.20185.

Goto, S., 2005, Thermal response of sediment with vertical fluid flow to periodic temperature variation at the surface: Journal of Geophysical Research, v. 110, p. B01106, doi: 10.1029/2004JB003419.

Hatch, C.E., Fisher, A.T., Revenaugh, J.S., Constantz, J., and Ruehl, C., 2006, Quantifying surface water-groundwater interactions using time series analysis of streambed thermal records: Method development: Water Resources Research, v. 42, p. 276–288, doi: 10.1029/2005WR004787.

Hatch, C.E., Fisher, A.T., Ruehl, C.R., and Stemler, G., 2010, Spatial and temporal variations in streambed hydraulic conductivity quantified with time-series thermal methods: Journal of Hydrology, v. 389, p. 276–288, doi: 10.1016/j.jhydrol.2010.05.046.

Huysmans, M., and Dassargues, A., 2005, Review of the use of Peclet numbers to determine the relative importance of advection and diffusion in low permeability environments: Hydrogeology Journal, v. 13, p. 895–904, doi: 10.1007/s10040-004-0387-4.

Ingebritsen, S.E., and Sanford, W.E., 1998, Groundwater in Geologic Processes: Cambridge, U.K., Cambridge University Press, 341 pp., p.

Irvine, Dylan J., Cranswick, Roger H., Simmons, Craig T., Shanafield, M.A., 2015, The effect of streambed heterogeneity on groundwater-surface water exchange fluxes inferred from temperature time series: Water Resources Research, p. 2108–2123, doi: 10.1002/2012WR013085.Received.

Janssen, F., Cardenas, M.B., Sawyer, A.H., Dammrich, T., Krietsch, J., and Beer, D. De, 2012, A comparative experimental and multiphysics computational fluid dynamics study of coupled surface – subsurface flow in bed forms: v. 48, p. 1–16, doi: 10.1029/2012WR011982.

Johnson, A., and Boer, B., 2005, Evaluation of an Inexpensive Small ‐ Diameter Temperature Logger for Documenting Ground Water–River Interactions: Groundwater Monitoring & Remediation, v. 25, p. 68–74.

Keery, J., Binley, A., Crook, N., and Smith, J.W.N., 2007, Temporal and spatial variability of groundwater–surface water fluxes: Development and application of an analytical method using temperature time series: Journal of Hydrology, v. 336, p. 1–16, doi: 10.1016/j.jhydrol.2006.12.003.

Lautz, L.K., 2010, Impacts of nonideal field conditions on vertical water velocity estimates from streambed temperature time series: Water Resources Research, v. 46, p. n/a–n/a, doi: 10.1029/2009WR007917.

Lautz, L.K., 2012, Observing temporal patterns of vertical flux through streambed sediments using time-series analysis of temperature records: Journal of Hydrology, v. 464-465, p. 199–215, doi: 10.1016/j.jhydrol.2012.07.006.

Luce, C.H., Tonina, D., Gariglio, F., and Applebee, R., 2013, Solutions for the diurnally forced advection-diffusion equation to estimate bulk fluid velocity and diffusivity in streambeds from temperature time series: Water Resources Research, v. 49, p. 488–506, doi: 10.1029/2012WR012380.

Marzadri, A., Tonina, D., and Bellin, A., 2011, A semianalytical three-dimensional process-based model for hyporheic nitrogen dynamics in gravel bed rivers: Water Resources Research, v. 47, p. 1–14, doi: 10.1029/2011WR010583.

McCallum, a. M., Andersen, M.S., Rau, G.C., and Acworth, R.I., 2012, A 1-D analytical method for estimating surface water-groundwater interactions and effective thermal diffusivity using temperature time series: Water Resources Research, v. 48, p. n/a–n/a, doi: 10.1029/2012WR012007.

Pulido-Velázquez, M., Andreu, J., and Sahuquillo, A., 2006, Economic Optimization of Conjunctive Use of Surface Water and Groundwater at the Basin Scale: Journal of Water Resources Planning and Management, v. 132, p. 454–467, doi: 10.1061/(ASCE)0733-9496(2006)132:6(454).

Rau, G.C., Acworth, R.I., and Andersen, M.S., 2012, Experimental investigation of the thermal dispersivity term and its significance in the heat transport equation for flow in sediments: Water Resources Research, v. 48, p. n/a–n/a, doi: 10.1029/2011WR011038.

Rau, G.C., Andersen, M.S., McCallum, A.M., and Acworth, R.I., 2010, Analytical methods that use natural heat-as-a-tracer to quantify surface water–groundwater exchange, evaluated using field temperature records: Hydrogeology Journal, v. 18, p. 1093–1110, doi: 10.1007/s10040-010-0586-0.

Rau, G.C., Andersen, M.S., McCallum, A.M., Roshan, H., and Acworth, R.I., 2014, Heat-as-a-tracer to quantify water flow in near-surface sediments: Earth Science Reviews, v. 129, p. 40–58, doi: 10.1016/j.earscirev.2013.10.015.

Rau, G.C., Cuthbert, M.O., McCallum, A.M., Halloran, L., and Andersen, M.S. 2015, Assessing the accuracy of 1-D analytical heat tracing for estimating near-surface sediment scour/deposition and water flux under transient conditions: Journal of Geophysical Research Earth Surface, 120, doi: 10.1002/2015JF003466.

Rosenbury, D.O., and Morin, R.H., 2004, Use of an Electromagnetic Seepage Meter to Investigate Temporal Variability in Lake Seepage: Ground water,.

Roshan, H., Rau, G.C., Acworth, I.R., and Andersen, M.S., 2012, Use of heat as tracer to quantify vertical streambed flow in a two-dimensional flow field: Water Resources Research, v. 48, p. n/a–n/a, doi: 10.1029/2012WR011918.

Sawyer, A.H., Bayani Cardenas, M., and Buttles, J., 2012, Hyporheic temperature dynamics and heat exchange near channel-spanning logs: Water Resources Research, v. 48, p. W01529, doi: 10.1029/2011WR011200.

Schmidt, C., Martienssen, M., and Kalbus, E., 2011, Influence of water flux and redox conditions on chlorobenzene concentrations in a contaminated streambed: Hydrological Processes, v. 25, p. 234–245, doi: 10.1002/hyp.7839.

Scibek, J., Allen, D.M., Cannon, A.J., and Whitfield, P.H., 2007, Groundwater-surface water interaction under scenarios of climate change using a high-resolution transient groundwater model: Journal of Hydrology, v. 333, p. 165–181, doi: 10.1016/j.jhydrol.2006.08.005.

Shanafield, M., Hatch, C., and Pohll, G., 2011, Uncertainty in thermal time series analysis estimates of streambed water flux: Water Resources Research, v. 47, p. 1–7, doi: 10.1029/2010WR009574.

Stallman, R., 1965, Steady one‐dimensional fluid flow in a semi‐infinite porous medium with sinusoidal surface temperature: Journal of Geophysical Research, v. 70, p. 2821.

Stanford, J. A., and Ward, J. V., 1993, An Ecosystem Perspective of Alluvial Rivers: Connectivity and the Hyporheic Corridor: Journal of the North American Benthological Society, v. 12, p. 48–60, doi: 10.2307/1467685.

Stanford, J. A., and Ward, J. V., 1988, The hyporheic habitat of river ecosystems: Nature, v. 335, p. 64–66, doi: 10.1038/335064a0.

Swanson, T.E., and Cardenas, M.B., 2010, Diel heat transport within the hyporheic zone of a pool-riffle-pool sequence of a losing stream and evaluation of models for fluid flux estimation using heat: Limnology and Oceanography, v. 55, p. 1741–1754, doi: 10.4319/lo.2010.55.4.1741.

Tarnawski, V.R., Momose, T., and Leong, W.H., 2011, Thermal conductivity of standard sands II. Saturated conditions: International Journal of Thermophysics, v. 32, p. 984–1005, doi: 10.1007/s10765-011-0975-1.

Taylor, C.J., Pedregal, D.J., Young, P.C., and Tych, W., 2007, Environmental time series analysis and forecasting with the Captain toolbox: Environ. Model. Software, v. 22, p. 797–814.

Winter, T.C., Harvey, J.W., Franke, O.L., and Alley, W.M., 1998, Ground water and surface water: A single resource: USGS Publications, p. 79.

Zhou, S., Yuan, X., Peng, S., Yue, J., Wang, X., Liu, H., and Williams, D.D., 2014, Groundwater-surface water interactions in the hyporheic zone under climate change scenarios: Environmental Science and Pollution Research, p. 13943–13955, doi: 10.1007/s11356-014-3255-3.